

***In silico* Modeling of Itk Activation Kinetics in Thymocytes Suggests Competing Positive and Negative IP₄ Mediated Feedbacks Increase Robustness**

Sayak Mukherjee¹, Stephanie Rigaud⁷, Sang-Cheol Seok¹, Guo Fu⁷, Agnieszka Prochenka^{1,8}, Michael Dworkin^{1,5}, Nicholas R. J. Gascoigne⁷, Veronica J. Vieland^{1,2,4}, Karsten Sauer^{7*} and Jayajit Das^{1,2,3,6*}

¹Battelle Center for Mathematical Medicine, The Research Institute at the Nationwide Children's Hospital and Departments of ²Pediatrics, ³Physics, ⁴Statistics, ⁵Mathematics and ⁶Biophysics Graduate Program, The Ohio State University, 700 Children's Drive, Columbus, OH 43205. ⁷ Department of Immunology and Microbial Science, The Scripps Research Institute, La Jolla, CA 92037. ⁸Institute of Computer Science, Polish Academy of Sciences, Warsaw, Poland.

One-sentence summary:

Competing positive and negative IP₄ feedbacks increase robustness of PI3K signaling via Itk in thymocytes against variations at the single cell level.

* Corresponding authors

Abstract

The inositol-phosphate messenger inositol(1,3,4,5)tetrakisphosphate (IP₄) is essential for thymocyte positive selection by regulating plasma-membrane association of the protein tyrosine kinase Itk downstream of the T cell receptor (TCR). IP₄ can act as a soluble analog of the phosphoinositide 3-kinase (PI3K) membrane lipid product phosphatidylinositol(3,4,5)trisphosphate (PIP₃). PIP₃ recruits signaling proteins such as Itk to cellular membranes by binding to PH and other domains. In thymocytes, low-dose IP₄ binding to the Itk PH domain surprisingly promoted and high-dose IP₄ inhibited PIP₃ binding of Itk PH domains. However, the mechanisms that underlie the regulation of membrane recruitment of Itk by IP₄ and PIP₃ remain unclear. The distinct Itk PH domain ability to oligomerize is consistent with a cooperative-allosteric mode of IP₄ action. However, other possibilities cannot be ruled out due to difficulties in quantitatively measuring the interactions between Itk, IP₄ and PIP₃, and in generating non-oligomerizing Itk PH domain mutants. This has hindered a full mechanistic understanding of how IP₄ controls Itk function. By combining experimentally measured kinetics of PLC γ 1 phosphorylation by Itk with *in silico* modeling of multiple Itk signaling circuits and a maximum entropy (MaxEnt) based computational approach, we show that those *in silico* models which are most robust against variations of protein and lipid expression levels and kinetic rates at the single cell level share a cooperative-allosteric mode of Itk regulation by IP₄ involving oligomeric Itk PH domains at the plasma membrane. This identifies MaxEnt as an excellent tool for quantifying robustness for complex TCR signaling circuits and provides testable predictions to further elucidate a controversial mechanism of PIP₃ signaling.

Author Summary:

Inositol phosphate second messengers can regulate interactions between receptor signaling and lipid metabolic networks, critically affecting cell decision processes. However, the molecular mechanisms underlying such cross-regulation are poorly understood. Pairing mathematical modeling and experiments, we elucidate these mechanisms in the activation of T cells developing in the thymus (thymocytes), which is carefully controlled by TCR induced production of the membrane lipid PIP₃, soluble IP₄, and activation of the kinase Itk. T cells are major orchestrators of our adaptive immune system. Their development in the thymus is critically monitored to produce functional but self-tolerant T cells in the periphery. We combine experimentally measured kinetics of Itk mediated PLC γ 1 phosphorylation with Maximum Entropy (MaxEnt) based computational simulations into a novel approach to analyze the robustness of Itk activation kinetics. Our results provide testable predictions to further elucidate a controversial mechanism of PIP₃ signaling.

Introduction

Hydrolysis of plasma membrane phospholipids generates various cellular messengers [1]. Among these, multiple isomeric inositol phosphates (IP) [1-4] form an “IP code”[5] whose members can regulate critical decision processes downstream of many receptors in diverse cell types. However, the specific mechanisms and precise molecular circuitries that underlie the regulation of cell functions by soluble IPs are poorly understood. We and others previously reported an essential role for inositol(1,3,4,5) tetrakisphosphate (IP₄) in regulating T cell development [2,3,6,7].

T cells are key mediators of adaptive immune responses. Through a plasma-membrane anchored TCR, they recognize pathogen-derived peptides bound to Major Histocompatibility Complex proteins (pMHC) on the surface of antigen-presenting cells. TCR engagement triggers activation, proliferation and effector functions in peripheral T cells that then kill pathogen-infected cells and control immune responses. During T cell development in the thymus, somatic mutation of the antigen-binding TCR α/β subunit genes creates a thymocyte repertoire with random TCR specificities. However, many of these TCRs are non-functional or interact with the body's self-antigens with high affinity, causing autoimmune disorders if the respective T cells were allowed to mature. To prevent this, thymic selection processes eliminate thymocytes carrying TCRs that fail to interact with, or interact with too strong affinity with self-peptide-MHC (pMHC) complexes. The latter process is known as negative selection, a key mechanism of central tolerance. Only those thymocytes whose TCR generates mild signals are positively selected to mature into T cells, which then populate peripheral organs. Balanced positive and negative selection are critical for generating a diverse but self-tolerant T cell repertoire [8-10]. Recent experiments provided a more complex picture of thymic selection, where certain high affinity peptides can 'agonist select' distinct regulatory T cell types [11,12].

TCR-pMHC binding triggers a series of signaling reactions, resulting in the formation of a plasma membrane-proximal signalosome containing Src (Lck, Fyn) and Syk family protein tyrosine kinases (Zap70), cytosolic (such as SLP-76, Gads, Grb-2), and transmembrane adapter proteins (such as LAT). TCR-activation of phosphoinositide 3-kinase (PI3K) converts the abundant membrane phospholipid phosphatidylinositol(4,5) bisphosphate (PIP₂) into phosphatidylinositol(3,4,5) trisphosphate (PIP₃). By binding to pleckstrin homology (PH) or other protein-domains, PIP₃ recruits key effectors such as the Tec family protein tyrosine kinase Itk (IL-2 inducing T cell activation kinase). Itk also contains SH2 and SH3 domains that bind to signalosome components. The Src kinase Lck phosphorylates Y₅₁₁ in the A-loop of the murine (Y₅₁₂ in the human) Itk kinase domain [13]. Subsequently, Itk propagates TCR signals by phosphorylating and activating signalosome-recruited phospholipase C γ 1 (PLC γ 1). PLC γ 1 then hydrolyzes PIP₂ into the second messenger molecules diacylglycerol (DAG) and inositol(1,4,5) trisphosphate (IP₃). The membrane lipid DAG further recruits and activates Rasgrp1 and PKCs that in turn activate the GTPase Ras and the Bcl-10/CARMA1/MALT complex, ultimately triggering thymocyte positive and negative selection, or peripheral T cell

responses [14,15]. Soluble IP₃ mobilizes Ca²⁺ from the endoplasmic reticulum (ER). Moreover, IP₃ 3-kinases such as ItpkB can phosphorylate IP₃ at its 3-position into IP₄ [2,6,7,14,16]. IP₄ chemically resembles the PH domain binding PIP₃ tetraphosphoinositol headgroup [14,17].

We and others identified ItpkB as essential for thymocyte positive selection [2,6,7]. *ItpkB*^{-/-} DP thymocytes show intact proximal TCR signaling but defective IP₄ production, Itk PIP₃-binding, signalosome recruitment and activation with ensuing reduced PLCγ1 activation, DAG production, and, Ras/Erk activation [2]. The ability of soluble IP₄ to bind to the Itk PH domain and in low μM doses promote PIP₃ binding, and the ability of the Itk PH domain to oligomerize suggested that IP₄ might promote Itk recruitment to membrane-PIP₃ through a cooperative-allosteric mechanism. In this model, IP₄-binding to one PH domain in an oligomer allosterically increases the ligand affinities of the other PH domains in the same oligomer [2]. IP₄ promoted Itk activation appears to be required for sufficient Itk activation to ensure positive selection, because an exogenous DAG-analog restored positive selection of *ItpkB*^{-/-} thymocytes [2]. However, high-dose IP₄ inhibited Itk PH domain binding to PIP₃ *in vitro* [2]. Whether it does so *in vivo* is unknown [14]. In neutrophils, NK cells and myeloid progenitors, IP₄ competitively limits Akt PH domain binding to membrane PIP₃[18-20]. Which PH domains are positively versus negatively controlled by IP₄, and what determines whether IP₄ promotes or inhibits PH domain binding to PIP₃ or leaves it unaffected are important open questions [14,21]. In particular, the Itk PH domain might be bi-modally regulated by IP₄. However, the detailed molecular interactions between Itk, PIP₃ and IP₄ *in vivo* are not well characterized. This leaves room for multiple alternate hypotheses/mechanisms. For example, one could also propose that the binding affinity of PIP₃ and IP₄ for Itk changes from a low to a fixed high value above a threshold IP₄ concentration. Such a mechanism implies that the interaction of Itk with IP₄ and PIP₃ after the threshold IP₄ concentration is reached does not involve a positive feedback. The situation is further confounded by elusive results from experiments probing Itk oligomerization [2,22-28].

The current lack of a mechanistic understanding of how IP₄ controls Itk PIP₃-interactions and whether Itk PH domain oligomerization is physiologically relevant arises from difficulties in quantitatively measuring the interactions between Itk, IP₄ and PIP₃, and in generating soluble Itk PH domain preparations for biophysical studies and non-oligomerizing Itk PH domain mutants for genetic analyses. Additional limitations arise from difficulties in measuring membrane recruitment of Itk in cell population based assays. It is also difficult to measure PIP₃ bound Itk or phosphorylation of PLC-γ1, a substrate of PIP₃ bound Itk, in large numbers of individual cells using flow cytometry techniques due to limited antibody quality. *In vitro* and cell-based studies based on ectopic Itk expression suggest the existence of several different monomeric and oligomeric Itk species, including head-to-head and head-to-tail dimers [2,22-28]. Andreotti and colleagues[22] showed that Itk molecules can self associate via their SH2-SH3 domains into auto-inhibitory oligomers. This is hindered by SLP-76 interactions with the Itk SH2-SH3 domains. It was suggested that Itk molecules might exist as auto-inhibited multimers in the cytosol, but after plasma membrane recruitment, Itk monomers might mediate downstream activation [22,26]. Other experiments [27,28] employing fluorescence complementation showed that formation of Itk head-to-head and head-to-tail

dimers requires the PH domain and may primarily occur at the plasma membrane, although low-abundance cytoplasmic dimers have not been excluded. Here, monomeric Itk was proposed to be primarily cytoplasmic and autoinhibited [27]. At least head-to-head dimerization is unaffected by mutations in the other (SH2/SH3) domains [28]. We found that the Itk PH domain can oligomerize with other Itk PH domains or full length Itk [2]. Thus, the PH domain is well suited to contribute to at least certain modes of Itk oligomerization, some of which could have positive or a combination of positive and negative functions regulated by IP₄/PIP₃. This could account for the limited activity-enhancing effect of disrupting SH3/SH2-domain mediated Itk dimerization [26].

Altogether, whether Itk PH domain dimerization has a physiological function, whether it promotes or inhibits Itk activation, whether IP₄ controls Itk function through positive or negative feedback, or both, and whether IP₄ has additional unrelated functions in thymocytes, are all contentious questions in the field. Resolving them is very important, because PI3K is a paramount regulator of signaling from many receptors in most cells. PIP₃ hyperactivity is a major contributor to immune, metabolic and other diseases including cancers [29,30]. IP₃ 3-kinases are broadly expressed and IP₄ has been found in many cell types. Thus, IP₄ regulation of PIP₃ function could be broadly important and elucidating the precise molecular mechanisms through which IP₄ controls PIP₃ signaling improves our understanding of a very fundamental and important signaling pathway with great therapeutic relevance [14].

To further explore how the presence or absence of Itk PH domain oligomerization, of positive or negative IP₄ feedback or both, or of specific molecular modes of association of Itk, PIP₃ and IP₄ impact TCR signaling, we constructed seven different molecular models (Table I and Fig. S1B). We used a Maximum Entropy (MaxEnt) [31-33] based approach to quantify the robustness of each model against variations in rate constants and protein expression levels at the single cell level. Each model was constrained to reproduce the Itk activation kinetics of an entire cell population measured in biochemical experiments. We found that those models involving dimeric Itk molecules with IP₄ mediated competing positive and negative feedbacks are most robust. As in many other cell signaling systems [34], the actual signaling kinetics in thymocytes are likely to be robust against such variations, while retaining their sensitivity to small variations in antigen affinity or dose. On this basis, our simulations best support biphasic Itk regulation by IP₄ in thymocytes. Future testing of this exciting hypothesis will require the so far unsuccessful generation of non-oligomerizing Itk PH domain mutants and their expression in *Itk*^{-/-} mice, along with currently impossible single-cell measurements of IP₄ levels in large cell populations.

RESULTS

Multiple molecular models can be constructed to probe Itk, IP₄, and PIP₃ interactions *in silico*

We constructed seven different molecular models (Table I, Fig. S1B) based on available details about interactions between Itk, PIP₃ and IP₄ from the biochemical studies described above. Including Itk kinase domain activation by Lck only caused qualitative changes in the relative robustness of the models (Fig. S17, Tables S9-S15). Therefore, for

simplicity, we considered models that do not contain Itk activation by Lck explicitly. We also did not consider Itk autophosphorylation explicitly in the models as it does not affect Itk catalytic activity. In addition, the role of Itk autophosphorylation in PLC γ 1 activation remains unclear [22]. Since we aimed to elucidate general characteristics of the kinetics of PIP $_3$ binding to Itk, we used a simplified modeling scheme (Fig. 1) and did not consider the detailed molecular composition of the TCR and the LAT associated signalsome. The models also do not investigate different mechanisms for formation of Itk oligomers. Rather, they probe the functional consequences of having Itk PH domain dimers versus monomers and how these can affect interactions between Itk, PIP $_3$ and IP $_4$ in the presence or absence of IP $_4$ mediated positive feedback. The kinetics of PIP $_3$ production due to signal-dependent recruitment of PI3K are not considered explicitly as PIP $_3$ is produced at a much faster time scale (in seconds, [35][36][37]) than the time scales of PLC γ 1 activation (up to 60 min, Figs. 3, S18) analyzed in this study. The concentrations of LAT bound Itk and of PIP $_3$ were considered approximate markers for the strength of the stimulation generated by antigen-TCR interactions. Therefore, we considered fixed initial concentrations of Itk and PIP $_3$ in the models. We approximated the production of IP $_4$ from PIP $_2$ by a single one-step reaction to simplify the models further .

The models can be broadly classified into two types: (i) Models M1-M4 and M7 containing IP $_4$ mediated positive feedbacks. (ii) Models M5 and M6 lacking IP $_4$ positive feedback. In each type, we further considered models that contained Itk dimers (models M1-M3, M5, M7), or monomers (models M4, M6). In models M1-M3, each of the two PH domains in the Itk dimer can independently bind to either IP $_4$ or PIP $_3$ with a weak affinity when the other PH domain is unoccupied. However, once a PH domain is bound to an IP $_4$ molecule, it allosterically increases the affinity of the other PH domain for PIP $_3$ and IP $_4$. Models M1-M3 differ from each other in the relative increase in the affinities of one PH domain in the Itk dimer toward IP $_4$ vs. PIP $_3$ caused by IP $_4$ or PIP $_3$ binding to the other PH domain in the dimer. In contrast, in M7, binding of PIP $_3$ to one PH domain in a dimer increases the affinity of the other PH domain for PIP $_3$ but not for IP $_4$. These models probed potential secondary interactions between Itk dimers and the membrane lipids. In the monomeric model, M4, IP $_4$ binds the single Itk PH domain with a weak affinity and induces a conformational change that increases the affinity of this PH domain for both PIP $_3$ and IP $_4$. Models M5 and M6 lack positive IP $_4$ feedback. Instead, the Itk PH domain binds to IP $_4$ and PIP $_3$ with equal affinity. These models probed a mechanism where the Itk PH domain interacts with IP $_4$ and PIP $_3$ once a small threshold IP $_4$ concentration is generated. We assumed that the small threshold level of IP $_4$ is generated at a time scale much smaller than the timescale (min) of robust Itk activation and did not consider the kinetics generating the threshold level of IP $_4$ explicitly in M5 and M6. The models are summarized in Table I, Fig. S1B, and tables S1-S8.

The shape of transient Itk activation kinetics depends on specific molecular wirings and feedbacks in the different models

We studied the kinetics of Itk binding to PIP $_3$ using deterministic mass-action kinetic rate equations described by ordinary differential equations (ODE) for all the models, ignoring stochastic fluctuations in the copy numbers of signaling proteins occurring due to the

intrinsic random nature of biochemical reactions [38]. Including such fluctuations did not change the kinetics qualitatively (Figs. S2-S3). In all seven models, the kinetics of PIP₃ bound Itk showed a transient behavior (Fig. 2A); PIP₃ bound Itk started with a low concentration, reached a peak value at an intermediate time, and then fell back to a small concentration at later times. We found that initially few Itk molecules were bound to PIP₃. With increasing time, more Itk molecules became associated with PIP₃ molecules due to the binding reactions between Itk and PIP₃. This produced the rise in the Itk-PIP₃ concentration. However, as the concentrations of PIP₃ bound Itk molecules increased, they also induced increased production of IP₄ molecules. IP₄ competed with PIP₃ for binding to the Itk PH domain, and when the number of IP₄ molecules exceeded that of PIP₃ molecules, most of the Itk molecules were sequestered to the cytosol by forming stable complexes only with IP₄. This reduced the rate of PIP₃ association of Itk and eventually resulted in the decrease of the PIP₃ bound Itk molecules. IP₄ outnumbered PIP₃ at later times because the number of PIP₂ molecules, the source of IP₃ and IP₄ in a cell, is considered not limiting in contrast to PIP₃ [37,39]. We emphasize that the results of our models do not depend on the cytosolic nature of Itk-IP₄ complexes, but on the model assumption that Itk (or Itk oligomers) bound to IP₄ at every PH domain does not induce any PLC γ 1 activation.

We characterized the ‘shape’ of the temporal profile of PIP₃ bound Itk in terms of (i) the largest concentration of PIP₃ bound Itk in the entire temporal profile (peak amplitude value A); (ii) the time taken for PIP₃ bound Itk to reach the peak value (peak time τ_p); and (iii) the time interval during which the PIP₃ bound Itk concentration is greater than or equal to half of the peak value (peak duration τ_w , Fig. 2B). A dimensionless variable quantifying the asymmetry in the shape of the kinetics, denoted as the asymmetry ratio $R = \tau_w/\tau_p$ (Fig. 2B), turned out to be a useful indicator for differentiating temporal profiles of concentrations of PIP₃ bound Itk in simulations and experiments. R also quantifies if the time scale for the decay of the concentration of PIP₃ bound Itk after the peak value is reached is larger than or comparable to τ_p (the timescale for producing the peak value A). E.g., when $R \approx 1$, it implies that the τ_p is comparable to decay time. $R \gg 1$ indicates a more persistent signal with long decay times. Differences (transient vs. persistent) in the shapes of kinetic profiles of signals downstream of Itk activation have been observed to influence thymocyte decision outcomes [2,40]. Therefore, R , which characterizes the persistent or transient nature of Itk activation, also contains details directly relevant for thymic selection outcomes. We found that the shape of the transient kinetics of PIP₃ binding to Itk varied substantially depending on the feedbacks and the molecular wiring of the networks. Since the reaction rates used in the models are difficult to measure *in vivo* for thymocytes, we estimated the rates based on interaction strengths measured *in vitro* between PH domains and inositol phosphates in other cells, and from temporal profiles of PLC γ 1 activation measured in experiments with T cells (tables S1-S7). Previous work demonstrated the essential role of phosphorylated PLC γ 1 and its kinetics in regulating thymocyte positive, negative and agonist selection [41,42]. Phospho-PLC γ 1 is also known to mirror other indicators of T cell activation such as TCR ζ - or LAT-phosphorylation, or Erk-activation [2,40]. Therefore phospho-PLC γ 1 is a relevant marker for functional T cell responses.

We studied variations in the kinetics of PIP₃ bound Itk for different initial concentrations of Itk and PIP₃. This probed how different ligand doses or affinities affected the PIP₃ binding of Itk. We found that the peak concentration of PIP₃ bound Itk increased in a graded manner with increasing initial Itk and PIP₃ concentrations in all models (Fig. S4). However, the peak time τ_p (Fig. S5), and the asymmetry ratio R (Fig. 2C), were affected differently in different models. Among the feedback models, M1-M3 and M7 containing Itk dimers generated smaller values (varied between 2 to 6) of R compared to monomeric model M4 which produced a much larger range of R (~20 -120) (Fig. 2C). The models lacking positive feedbacks (M5 and M6) generated large values (~100-700) of R compared to feedback models with Itk dimers (Fig. 2C). In the feedback models, the initial low affinity binding-unbinding interactions between Itk and PIP₃/IP₄ are converted into high affinity interactions due to the positive feedback. Therefore, a large part of τ_p is spent in building up the positive feedback interactions controlled primarily by the weak affinity binding-unbinding rates (or K_D). The small values of R in models M1-M3 and M7 occurred because stronger negative feedbacks resulted in much smaller timescales for substantially reducing the concentration of PIP₃ bound Itk after it reached its peak value compared to the other models. In the models lacking positive feedback (M5, M6), concentrations of PIP₃ bound Itk decreased at a much slower rate than the peak time leading to large values of R . In the monomeric model, the relatively weaker strength of positive and negative feedbacks resulted in larger decay time scales for the PIP₃ bound Itk, producing large values of R . These results are analyzed in detail in the web supplement and Figs. S6-S11. We will show below how the ability of feedback models with Itk dimers to produce R values within a small range leads to higher robustness of these models against parameter variations at the single cell level.

Models containing dimeric Itk and IP₄ mediated dueling positive and negative feedbacks are the most robust models

Quantification of robustness in in silico models: The reaction rates describing non-covalent primary and secondary interactions between Itk, PIP₃ and IP₄ can depend on specific properties of the local cellular environment, such as local membrane curvature [43], molecular crowding [44,45], and the presence of different lipid molecules in the proximity [46]. Since these factors can vary from cell to cell, the reaction rates can vary at the single cell level. In addition, protein expression levels can vary between cells. Such variations are also known as extrinsic noise fluctuations [47,48]. The IP₄ production rate depends on the concentrations of ItpkB, Calmodulin (CaM), and released calcium [3]. Hence, the IP₄ production rates in our models which approximate all such dependencies with a one-step reaction will vary between individual cells as well. The above variations are capable of producing differences in the shapes of temporal profiles of activation of signaling proteins in individual cells [49]. In the coarse-grained or approximate models we have constructed, many molecular details have been approximated. For example, multiple phosphorylation sites or SH2/SH3 binding sites of Itk, LAT, SLP-76 and their regulation via TCR induced signaling are not considered explicitly [3,22,50,51]. These detailed molecular signaling events can depend on the concentrations of proteins, enzymes, and lipids, and can thus be regulated differently in different cells due to extrinsic noise fluctuations. Consequently, the rates in our *in silico* models that effectively describe those detailed signaling events can vary from cell to cell. Consistent

with this view, our simulations with the ODE models showed that the shape of the kinetics of PIP₃ bound Itk, characterized by A , τ_p , and R , changed significantly as the rate constants and initial concentrations in a model were varied (Figs. S12-S14). Thus, activation kinetics of a marker molecule (e.g. PLC γ 1) measured in experiments (e.g., immunoblots) assaying a large cell population represent averages over a range of temporal profiles with different shapes occurring at the single cell level.

We found that for some ranges of the reaction rates, multiple different *in silico* models can produce the same values of A , τ_p , and R (Fig. S12-S14). This implied that more than one *in silico* model *could* reproduce the mean temporal profile measured in cell population assays. However, it is possible that each model could show a different degree of robustness to variations in reaction rates and initial concentrations at the single cell level. Robustness of time dependent responses in a cell population against variations at the single cell levels has been observed in several systems, e.g., oscillations in adenosine 3',5' cyclic monophosphate (cAMP) concentrations in a population of *Dyctostelium* [52,53], or damped oscillations of protein 53 (p53) in a population of human breast cancer epithelial cells [54]. Robustness of cellular functions against variations in external conditions and cell-to-cell variability has been proposed as a required design principle for a wide range of biochemical networks [55-58]. We therefore decided to ask: Which model(s) can accommodate the largest variation in reaction rates and initial concentrations, while reproducing the mean temporal profile of PIP₃ bound Itk measured as generation of phosphorylated PLC γ 1 in cell population experiments? We postulate that the answer to this question will point us to the molecular circuitry most likely to be the relevant model, in the sense that it robustly produces a specific temporal response at the cell population level despite variations in the kinetics in individual cells.

To identify the most robust model(s), we quantified robustness using a method based on the principle of Maximum Entropy (MaxEnt) [31-33]. MaxEnt provides a mechanism for estimating the probability distribution of the rate constants and initial Itk and PIP₃ concentrations under constraints derived from experimental data (Fig. 3A-B, 4A-B). Here, we used the experimentally obtained values τ_p^{expt} and R^{expt} as the constraints. It is difficult to directly relate the amplitude (in units of number of molecules in the simulation box) in the *in silico* models to experiments, where amplitudes are calculated from the fold change of the immunoblot intensities upon stimulation. Therefore, the experimental values of A can be related to the number of activated molecules, at best, through a proportionality constant dependent on specific protocols used in an assay. Because of these issues we chose a value of A^{expt} , representing A in experiments, where every *in silico* model produced amplitudes at A^{expt} for a set of parameters within the range of variations considered here. We then varied A^{expt} to investigate the change in robustness of the models and address the arbitrariness in the choice of A^{expt} . We constructed a relative entropy measure (Kullback-Leibler distance, D_{KL} , calculated on the \log_{10} scale) [59] that measures the deviation of the constrained MaxEnt distribution from the unconstrained MaxEnt distribution, in which all values of the rate constants and initial concentrations are equally likely (uniform distribution). Thus D_{KL} is being used as a measure of how “close” each model can get to one which is completely indifferent to the values of the rate constants, given the experimental constraints. We then compared D_{KL} across our models in order to find the most robust model compatible with experimental results. Note that the minimum value of D_{KL} is 0,

with smaller values indicating greater robustness. We have also analyzed D_{KL} for different models when τ_p^{expt} and R^{expt} were constrained but the amplitude A^{expt} was not constrained (Fig. S23). The results are qualitatively similar to that of the case when τ_p^{expt} , R^{expt} , and A^{expt} were constrained. This indicates that the robustness of the temporal shape of Itk membrane recruitment kinetics rather than the amplitude contributes substantially toward the increased robustness of the feedback models with Itk dimers.

Experimental analysis of Itk activation kinetics in mouse thymocytes: To determine which Itk activation profile predicted by models M1-M7 produces maximum robustness while reproducing experimental data, we analyzed Itk activation kinetics in mouse $CD4^+CD8^+$ double-positive (DP) thymocytes, the developmental stage where positive selection occurs [9,60]. To generate a homogeneous cell population in which every cell expresses the same TCR and in which the TCR has not been stimulated by endogenous ligands prior to *in vitro* stimulation, we used *OT1 TCR-transgenic*, *RAG2^{-/-}*, *MHCI($\beta 2m$)^{-/-}* mice. Their DP cells express exclusively the transgenic OT1 TCR, which recognizes the ovalbumin-derived peptide ligand OVA and recently identified endogenous peptide ligands presented by MHC I molecules [40,61]. In *MHCI^{-/-}* mice, no endogenous ligands are presented to OT1 TCR-transgenic T cells and their development is blocked at the DP stage due to impaired positive selection. *In vitro*, OT1 TCR transgenic DP cells can be stimulated with MHC I tetramers loaded with OVA peptide [40,61]. Due to its high affinity for the OT1 TCR, OVA stimulation generates strong TCR signals and induces DP cell deletion. A number of OVA-derived altered peptide ligands (APL) have been generated which carry single or multiple amino acid substitutions compared to OVA. In the peptide series OVA>Q4R7>Q4H7>G4, such substitutions progressively reduce OT1 TCR affinity and signaling capacity [40]. Consequently, OVA and Q4R7 cause *OT1 TCR-transgenic* DP cell negative selection, whereas Q4H7 and G4 trigger positive selection.

We used MHC I tetramers presenting either one of these four peptides to stimulate *RAG2^{-/-}MHC^{-/-} OT1 TCR-transgenic* DP cells for various time points. We analyzed PLC γ 1 phosphorylation at Y₇₈₃, normalized to total PLC γ 1 protein levels, as a measure for Itk activation [2] (Fig. 3A). Stimulation by all peptides induced fast PLC γ 1 phosphorylation already at 1 min which peaked at 2 min and then decreased over the next 60 min to very low levels which, however, were still above background levels in unstimulated cells. The decrease was fastest between 2 and 5 min and then progressively slowed down. As expected, overall levels of PLC γ 1 phosphorylation progressively decreased with decreasing peptide affinity/signaling capacity in the order OVA>Q4R7>Q4H7>G4. An asymmetric peak shape with an extended right flank was preserved across all signal intensities. We calculated the peak durations (τ_w), peak times (τ_p) and asymmetry ratios $R = \tau_w/\tau_p$ in Table II for stimulation with OVA, Q4R7, Q4H7 and G4, respectively. Consistent with preserved peak asymmetry, all ratios R were >1.

Comparison between experiments and conclusions: The phospho-PLC γ 1 levels (representing active Itk) for different affinity peptides peaked at $\tau_p=2$ mins with R values from 1.9-4.3 (Table II). Therefore, we fixed $\tau_p^{expt}=\bar{\tau}=2$ mins (the bar indicates average over the cell population) for quantifying robustness in the *in silico* modeling. The low, medium and large initial Itk and PIP₃ concentrations represent stimulation by weak (G4),

moderate (Q4R7, Q4H7) and high affinity (OVA) ligands, respectively. Analyzing D_{KL} (Fig. 3C) showed that for large initial PIP_3 and Itk concentrations (representing OVA stimulation) the feedback models incorporating Itk PH domain dimers (M1-M3, M7) were substantially more robust (Smaller D_{KL} values) than the models lacking feedbacks (M5, M6) for small values of R (<3). Monomeric feedback model M4 produced large D_{KL} values (1.5-5). M5, M6 and M4 produced much larger ranges of R (Fig. S14) as the parameters were varied compared to the feedback models with Itk dimers where the values of R were clustered around $R^{expt} \sim 2$. This behavior contributed substantially to the increased robustness of the feedback models with dimers as these models could accommodate for larger ranges of parameter variations while being able to maintain the constraint imposed by R^{expt} . The relative robustness of the feedback versus feedback-free models showed similar qualitative trends for the other ligands, Q4R7, Q4H7, and G4 (Fig. S15-S16). This suggests that the models containing feedbacks and Itk dimers are substantially more robust than models with Itk monomers or lacking feedbacks.

Evaluation of robustness in polyclonal thymocytes: The molecular wiring of Itk, PIP_3 and IP_4 interactions is unlikely to depend on the clonal nature of the T cells. Thus, the feedback models with Itk dimers should also be more robust than the other models when used to describe the kinetics of $PLC\gamma 1$ activation in polyclonal DP thymocytes expressing many different TCRs with different ligand specificities, stimulated by antibodies against the common TCR subunit CD3 alone or with co-ligation of the common coreceptor CD4. Stimulation of non TCR-transgenic $MHC^{-/-}$ DP cells with $1\mu g/ml$ or $5\mu g/ml$ of $\alpha CD3$ or combined $\alpha CD3/\alpha CD4$ antibodies produced different R^{expt} and τ_p^{expt} values than the OT1 system above (Fig. 4A-4B, Fig S18, table. S16). Calculation of the robustness constrained by R^{expt} , τ_p^{expt} and A showed that feedback models M1, M2, M3 and M7 are again substantially more robust than the other models (Fig. 4C-4F, Fig. S19, S20). Large variations of R in M4, M5 and M6 as parameters were varied again made these models substantially less robust than the feedback models with Itk dimers.

DISCUSSION

Here, we used *in silico* simulations combined with a novel Maximum Entropy (MaxEnt) based method and cell population averaged measurements of $PLC\gamma 1$ activation kinetics to distinguish between multiple models constructed to elucidate different mechanisms of Itk activation in TCR signaling. Our analysis quantified the robustness of seven different models employing monomeric or dimeric Itk PH domains with or without positive and negative IP_4 feedback against variations of parameters (rates and concentrations) at the single cell level. MaxEnt has been widely used in diverse disciplines ranging from physics [62] via information theory [63] to biology [64-67] to estimate probability distributions of variables subject to constraints imposed by experimental data [33,65]. However, to our knowledge these methods have not been used for evaluating the robustness of dynamic models in cell signaling or gene regulatory systems. Using thymocyte positive selection as a physiologically important model process, our results show the usefulness of MaxEnt methods for such studies. We are currently working on extending the methods to include additional information from experiments (such as

variances), and also evaluating their performance in comparison with closely related approaches such as Bayesian analysis [68].

Our simulations predict that the models containing IP_4 feedbacks and Itk dimers are most robust. This is consistent with our previously proposed model of cooperative-allosteric regulation of Itk- PIP_3 interactions via IP_4 -binding to oligomeric Itk PH domains [2]. Thymocyte selection critically depends on TCR induced signals. Small differences in antigen peptide concentration or affinities for the same TCR can produce opposite (negative vs. positive) selection outcomes [40]. Thus, we consider it plausible that for a fixed antigen dose and affinity (or average initial concentrations of Itk and PIP_3 in our models), TCR signaling in thymocytes should be robust against cell-to-cell variations of protein/lipid concentrations, rate constants and local environment. But TCR signaling should retain sensitivity to small variations in antigen affinity or dose. A direct experimental validation of this assumption will require to test the probability distributions of τ_p , R , and A in cell populations where $PLC\gamma_1$ activation kinetics are measured in individual cells. However, we were unable to perform such single cell comparisons due to the insensitivity of FACS-based $PLC\gamma_1$ signaling assays. This indicates the importance of studying the effects of network architecture, rate constants, protein and lipid concentrations on system robustness in DP thymocyte selection in detail in the future. Thymocytes are an excellent *in vivo* model to probe the exquisite dependency of cell fate decisions on the affinity of TCR ligands with important physiological and pathological implications. This provides a valuable addition to the experimental and theoretical investigations of robustness in synthetic systems or transformed tissue culture cells *in vitro*.

On the basis of robustness, our simulations support bimodal positive and negative Itk regulation by IP_4 in thymocytes. They make a supportive argument that Itk PH domain oligomerization and IP_4 feedback are physiologically important, consistent with the severely defective TCR signaling, IP_4 production, Itk/ $PLC\gamma_1$ activation, positive selection and resulting immunodeficiency in *ItpkB^{-/-}* mice, the ability of IP_4 to bimodally control Itk PH domain binding to PIP_3 *in vitro*, and the reported Itk PH domain oligomerization [2,6,7,28]. They do, however, not exclude the possibility that IP_4 also has additional, unknown functions in DP cells [14].

Testing this exciting hypothesis will require currently impossible single-cell measurements of IP_4 levels in large cell populations. Moreover, the physiological roles and modes of Itk oligomerization, the specific PH domain contributions to Itk oligomerization, whether Itk oligomerization occurs in the cytoplasm or at the plasma membrane or both, whether it exclusively inhibits or can also promote Itk activation, and whether IP_4 promotes or inhibits Itk PH domain binding to PIP_3 or does both depending on its local concentration are all matters of active debate [2,22-28]. Their conclusive elucidation requires quantitative biophysical studies of full length Itk with or without mutational perturbation of individual and combined interactions among the different Itk domains implicated in its monomeric and oligomeric self-association, and the reconstitution of *Itk^{-/-}* mice with these mutants at endogenous expression levels. Unfortunately, difficulties to produce sufficient quantities of soluble full-length Itk or Itk PH domain protein, and a tendency of Itk and its PH domain to aggregate *in vitro* have precluded more quantitative analyses of Itk PH domain oligomerization and IP_4/PIP_3

interactions, as well as the generation of non-oligomerizing Itk PH domain mutants. Despite progress regarding SH2/SH3/proline-rich domain interactions [22-26] and some evidence for PH domain involvement [2,27,28], formation of several different homotypic Itk dimers with differing subcellular localization and functions further complicates such analyses and their interpretation. Our *in silico* results suggest that by enabling competing positive and negative IP₄ induced feedback, Itk PH domain oligomerization could render Itk signaling in DP thymocytes much more robust to parameter fluctuation between individual cells than could be achieved without Itk dimers, or without IP₄ feedback. Models M1-M3 and M7 involving Itk dimers and IP₄ feedbacks showed substantially larger robustness than models lacking feedbacks (M5-M6) or containing only monomeric Itk (M4). M1-M3 and M7 can describe the experimentally observed PLCγ1 kinetics with similar robustness. They differ only at the level of secondary Itk/IP₄/PIP₃ interactions. Similar robustness and the inherent variability of experimental data preclude the identification of one of these dimeric Itk feedback models as the only one operative *in vivo* thus far.

METHOD AND MATERIALS

Signaling kinetics in the *in silico* models

We constructed ODE based models. The ODEs described kinetics of concentrations of proteins and lipids in two well-mixed compartments representing plasma membrane and cytosol (Fig. S1A). The biochemical signaling reactions for each model are shown in tables S1-S7. The details regarding the construction of the ODEs and the parameters are given in the web supplement and Fig. S1. We use the rule based modeling software package BioNetGen [69] to generate time courses for the species kinetics for the signaling networks described by models M1-M7. This program produces a set of ODEs corresponding to the mass-action kinetics describing biochemical reactions in the networks and solves them numerically using the CVODE solver [70]. The ODEs for each model are listed in the supplementary material.

Quantification of robustness based on the maximum entropy principle

When a variable x can assume multiple values and is distributed according to a probability distribution $p(x)$, then the uncertainty associated with the distribution can be quantified by the entropy (S) defined as,

$$S = -\sum_x p(x) \ln p(x). \quad (1)$$

S is non-negative and is maximized when x is distributed according to a uniform distribution (i.e., x can take any value within a range with equal probability). Suppose $p(x)$ is unknown, but we do know the average value of a variable, f , that is a function of x , i.e., $f \equiv f(x)$. We can then maximize S under the constraint

$$\sum_x f(x) p(x) = \bar{f}. \quad (2)$$

The constrained MaxEnt distribution is given by $p(x) \propto \exp(-\lambda f(x))$, where the constant λ , also known as the Lagrange multiplier, is determined by solving Eq. (2) for λ when the above MaxEnt distribution for $p(x)$ is used in Eq. (2). The method can be easily

generalized to accommodate multiple variables and constraints. We used the constraints imposed by τ_p^{expt} , R^{expt} , and A^{expt} , or, τ_p^{expt} and R^{expt} that are measured over a cell population. Therefore, the MaxEnt distribution of the parameters in our calculation is given by, $p(\{k_i\}) \propto \exp(-\lambda_1 \tau_p(\{k_i\}) - \lambda_2 R(\{k_i\}) - \lambda_3 A(\{k_i\}))$, where λ_1, λ_2 , and, λ_3 denote the Lagrange's multipliers, and $\{k_i\}$ denote the values of rate constants and initial concentrations in individual cells. The Lagrange multipliers can be calculated from the constraint equations,

$$\begin{aligned} \sum_{\{k_i\}} \tau_p(\{k_i\}) p(\{k_i\}) &= \tau_p^{\text{expt}} \\ \sum_{\{k_i\}} R(\{k_i\}) p(\{k_i\}) &= R^{\text{expt}} \\ \sum_{\{k_i\}} A(\{k_i\}) p(\{k_i\}) &= A^{\text{expt}} \end{aligned} \quad (3)$$

The MaxEnt distribution thus describes how τ_p , R , and A , in individual cells are distributed over a cell population. The distribution also produces an estimation of the probability distributions for the rate constants and initial concentrations that regulate τ_p , R , and A , through the functions $\tau_p(\{k_i\})$, $R(\{k_i\})$, and, $A(\{k_i\})$, respectively. The specific relationship between the parameters, $\{k_i\}$, and the observables (τ_p , R , and A) is dependent on the molecular details of the models, M1-M7. In all the models prior to the MaxEnt calculation, the rate constants were chosen from a uniform distribution with lower and upper bounds equal to 1/10 and 10 times, respectively, of the base values shown in tables S1-S7. Similarly, the initial concentrations of proteins (e.g., Itk) and lipids (such as PIP3) were varied within a 35% [71] range from uniform distributions centered at the base values shown in Table S8. The joint uniform distribution in the parameters is given by $q(\{k_i\})$. We then used these MaxEnt distributions to quantify relative robustness of the models by calculating the Kullback-Leibler distance[59]

$$D_{KL} = \sum_{\{k_i\}} p(\{k_i\}) \ln(p(\{k_i\}) / q(\{k_i\})) \quad (4)$$

That is, for each model, we first find the probability distribution for the rate constants and initial concentrations that maximizes the entropy (robustness) for that model under the experimental constraints, giving the model a kind of "maximum benefit of the doubt." We then compare the resulting MaxEnt models with one another to evaluate their relative robustness to variation in the rate constants, in order to select the model(s) most likely to correctly represent the actual kinetics. When $p(\{k_i\})$ is equal to $q(\{k_i\})$, D_{KL} assumes the minimum value 0; as the distribution $p(\{k_i\})$ starts deviating from the uniform distribution, say by becoming sharply peaked around a particular value, D_{KL} increases. Thus maximizing the entropy S , is equivalent to minimizing D_{KL} in Eq. (4). The calculations of D_{KL} were done at a specific antigen dose which fixed the average values of initial concentrations of Itk and PIP3. Therefore, the robustness calculations did not exclude the sensitivity of PLC γ 1 activation to changes in PIP3 concentrations resulting from antigen dose variations. We calculated $p(\{k_i\})$ by minimizing the D_{KL} subject to the constraints imposed by Eq. (3). We used D_{KL} to rank order the models for a particular measured value of τ_p^{expt} , R^{expt} , and, A_{avg} . All the calculations were carried out using MATLAB. Additional details can be found in the supplementary material (Figs. S12-S15). Note that D_{KL} is unaffected by inclusion of additional parameters that do not

influence the experimentally measured variables (Fig. S21, Table S17). Thus having extra variables in a model does not in and of itself affect the relative robustness of models with variable numbers of parameters. We have used 100,000 sample points, which we have shown to be statistically sufficient in Fig. S22 for the faithful calculation of D_{KL} .

Thymocyte stimulation and immunoblot analysis

All mice were housed in the TSRI specific pathogen-free vivarium monitored by the TSRI Department of Animal Resources. All animal studies were approved by the TSRI IACUC and conform to all relevant regulatory standards.

DP cells were prepared as in [2] and rested at 37°C for 3 hours. Then, 10^7 DP cells per sample were incubated on ice for 15 min with 2.4 μ M MHCI tetramers pre-loaded with either one of the altered peptide ligands OVA, Q4R7, Q4H7 or G4 [40], stimulated by rapidly adding 37°C warm PBS for the indicated times and quickly lysed in 100 mM Tris, pH 7.5, 600 mM NaCl, 240 mM n-octyl- β -D-glucoside, 4% Triton, 4 mM EDTA and a protease/phosphatase inhibitor cocktail (Roche). Lysates were cleared by centrifugation at 14000 rpm for 10 minutes at 4°C, resolved by SDS-PAGE and analyzed via immunoblot as previously described [2]. Band intensities were quantified via densitometry using NIH *ImageJ* software, and phosphoY₇₈₃-PLC γ 1 intensities normalized to total PLC γ 1 amounts.

ACKNOWLEDGEMENTS

We thank our lab members for valuable discussions, Luise Sternberg and Lyn'Al Nosaka for mouse genotyping, and the TSRI vivarium for expert mouse husbandry. S.M thanks Susmita Basak for help with MATLAB.

Figure Captions:

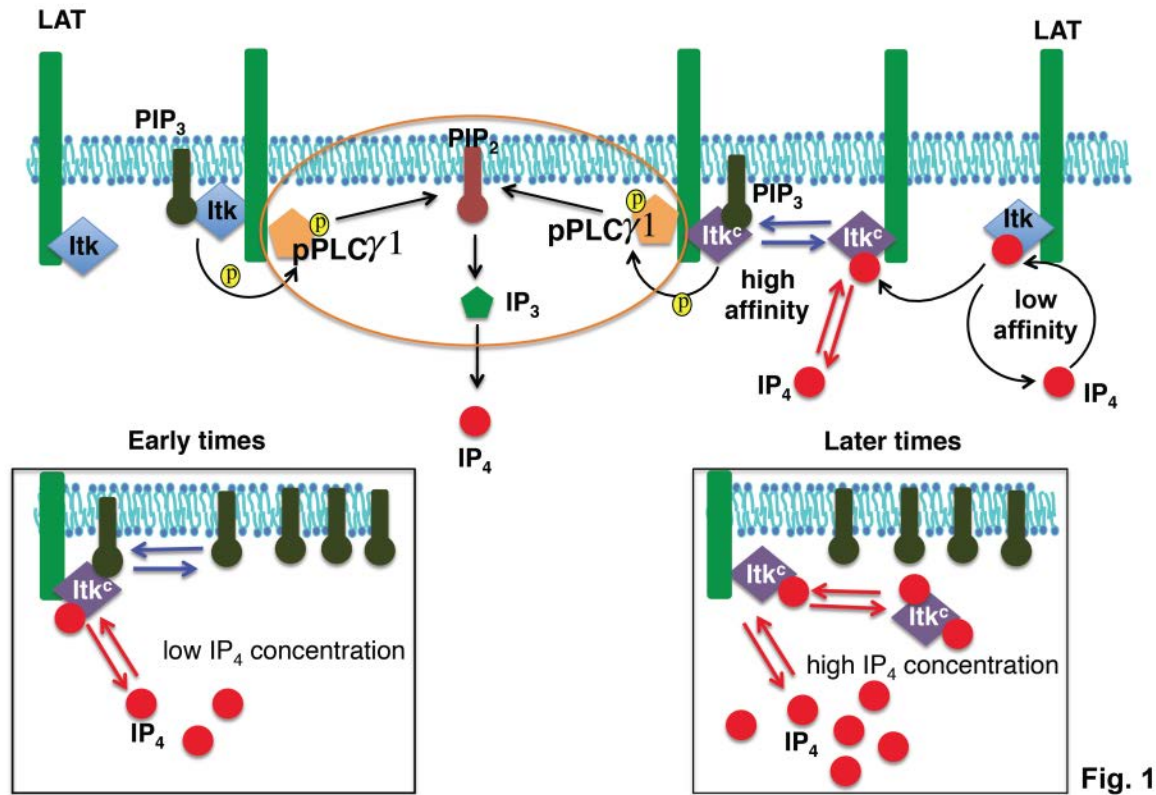


Fig. 1

Fig. 1. Relevant basic interactions between Itk, PIP₃ and IP₄. Following TCR-pMHC binding, Itk molecules are bound by the LAT signalsome via SLP-76 (not shown). Itk molecules (monomers or dimers, blue diamonds), bind the membrane lipid PIP₃ with low affinity through their PH domains. PIP₃ bound Itk phosphorylates and thereby activates LAT-bound PLCγ1. Activated PLCγ1 then hydrolyzes the membrane lipid PIP₂ into the soluble second messenger IP₃, a key mediator of Ca²⁺ mobilization. IP₃ 3-kinase B (ItpkB) converts IP₃ into IP₄ (red filled circle). For our *in silico* models, we simplified this series of reactions, encircled by the orange oval, into a single second order reaction where PIP₃ bound Itk converts PIP₂ into IP₄. In models M1-M4 and M7, IP₄ modifies the Itk PH domain (denoted as Itk^C, purple diamonds) to promote PIP₃ and IP₄ binding to the Itk PH domain. At the onset of the signaling, when the concentration of IP₄ is smaller than that of PIP₃, IP₄ helps Itk^C to bind to PIP₃ (left lower panel). However, as the concentration of IP₄ is increased at later times, IP₄ outcompetes PIP₃ for binding to Itk^C and sequesters Itk^C to the cytosol (right lower panel). In models M5/M6, IP₄ and PIP₃ do not augment each other's binding to Itk. However, IP₄ still outcompetes PIP₃ for Itk PH domain binding when the number of IP₄ molecules becomes much larger than that of PIP₃ molecules at later times.

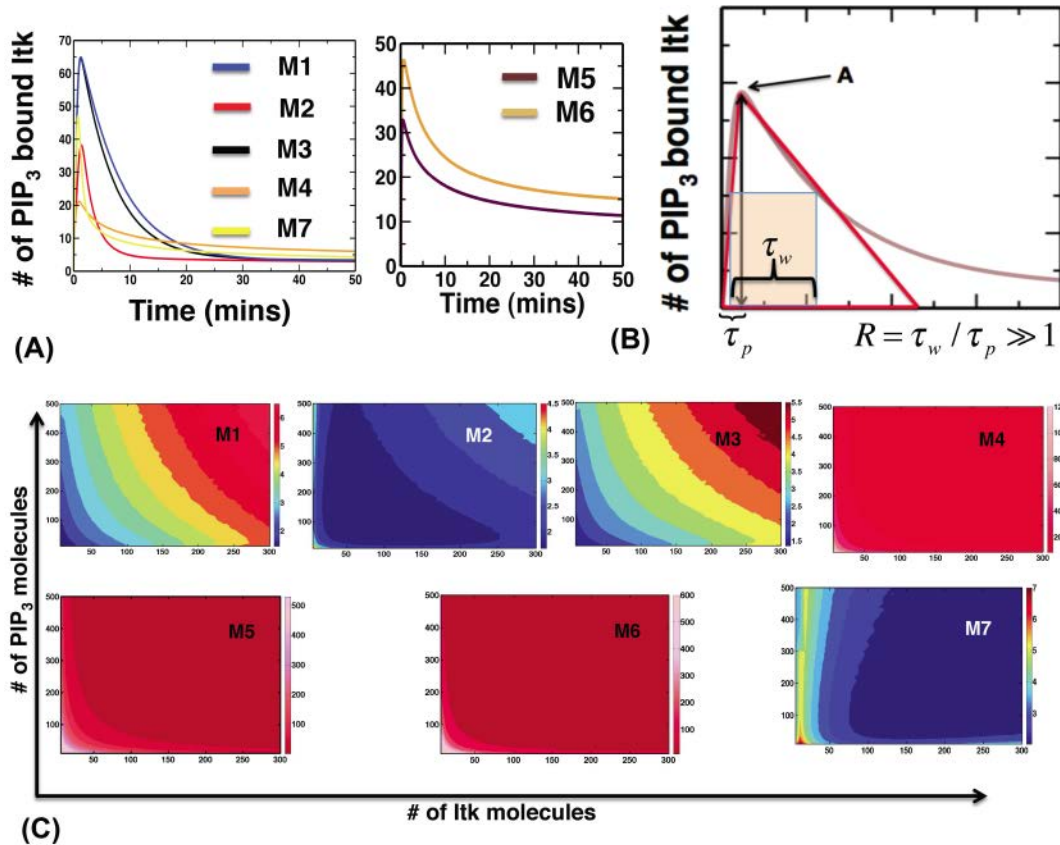
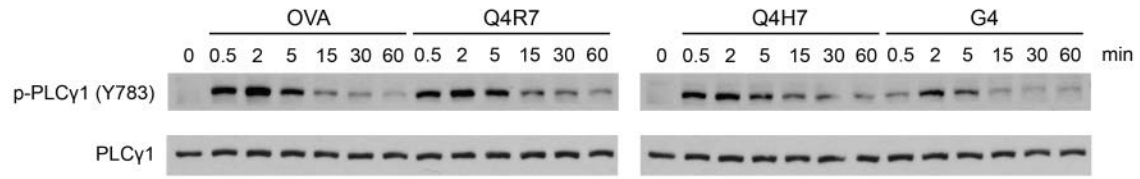


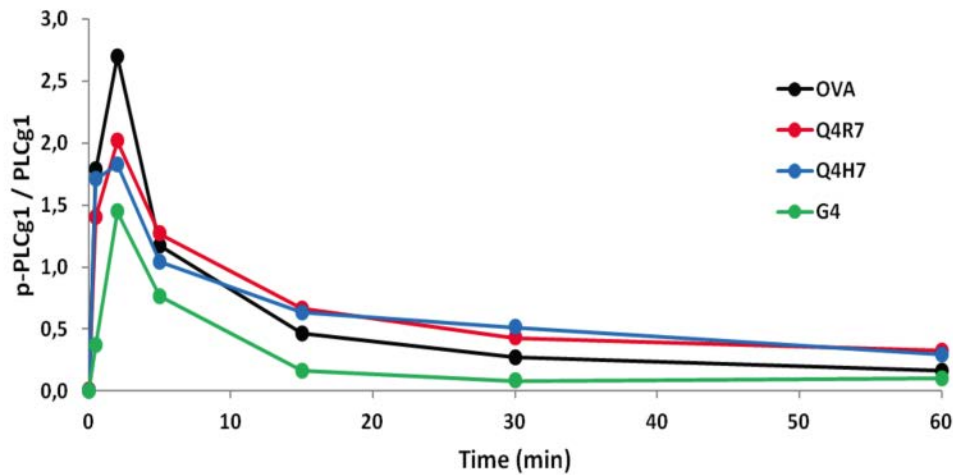
Fig. 2

Fig. 2. Different molecular interactions in models M1-M7 produce different temporal profiles of PIP₃ binding to Itk. (A) Kinetics of PIP₃ association of Itk for fixed initial PIP₃ and Itk concentrations (100 and 370 molecules, respectively) in models with feedbacks (M1-M4, and M7, left panel) and no feedbacks (M5-M6, right panel). (B) The shapes of the temporal profiles can be characterized by the parameters peak time (τ_p), peak width (τ_w), and peak value or amplitude (A). The dimensionless asymmetry ratio $R = \tau_w / \tau_p$ quantifies how symmetric the shape of the time profile is. A larger R value indicates larger asymmetry. (C) Variations in R in models M1-M7 for different initial concentrations of Itk and PIP₃. Color scales for R values are shown on the right of each panel.

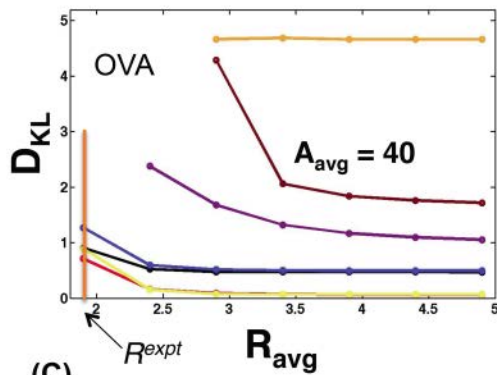


(A)

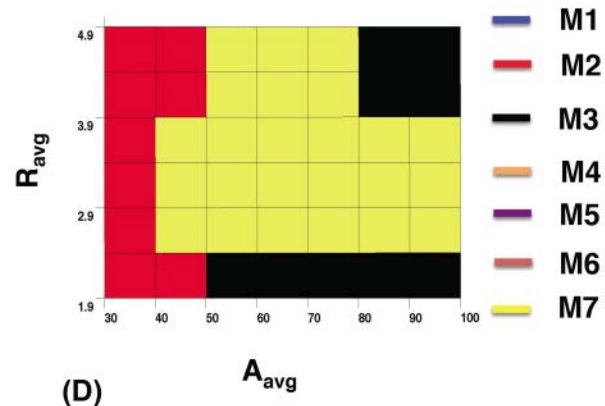
PLCγ1 Phosphorylation



(B)



(C)



(D)

Fig. 3. Experimentally measured PLCγ1 activation kinetics in DP thymocytes stimulated with TCR ligands of different affinities and robustness of *in silico* models. (A) Immunoblots showing Y₇₈₃-phosphorylated (upper panels) and total (lower panels) PLCγ1 protein amounts in *RAG2*^{-/-}*MHC*^{-/-}*OT1* *TCR-transgenic* DP thymocytes stimulated for the indicated times with MHC I tetramers presenting the indicated altered peptide ligands (APL). (B) Phospho-PLCγ1 levels normalized to total PLCγ1 protein amounts plotted over time for the indicated APLs. Their TCR affinity decreases in the order OVA (black) > Q4R7 (red) > Q4H7 (blue) > G4 (green). Band intensities were quantified via scanning and analysis with *ImageJ* software. Representative of several independent experiments. (C) Variation of the Kulback-Leibler distance D_{KL} with R for models M1-M3 (blue, red and black, respectively), M7 (yellow), and M4-M6 (orange, purple, and maroon, respectively) at high initial Itk ($Itk^0=140$ molecules) and PIP₃ concentrations ($PIP_3^0=530$ molecules), representing high-affinity OVA stimulation for

$\tau_p=2$ min and A (shown as A_{avg})=40 molecules. Note we use A to represent the amplitude A^{expt} in experiments measuring fold change in Itk phosphorylation (see the main text for further details). The vertical orange bar indicates R^{expt} for OVA. Color legend in (D). (D) The color map shows which model is most robust (has the lowest D_{KL}) as R^{expt} and A (shown as A_{avg}) are varied for the same parameters as in (C). The color legend is depicted on the right.

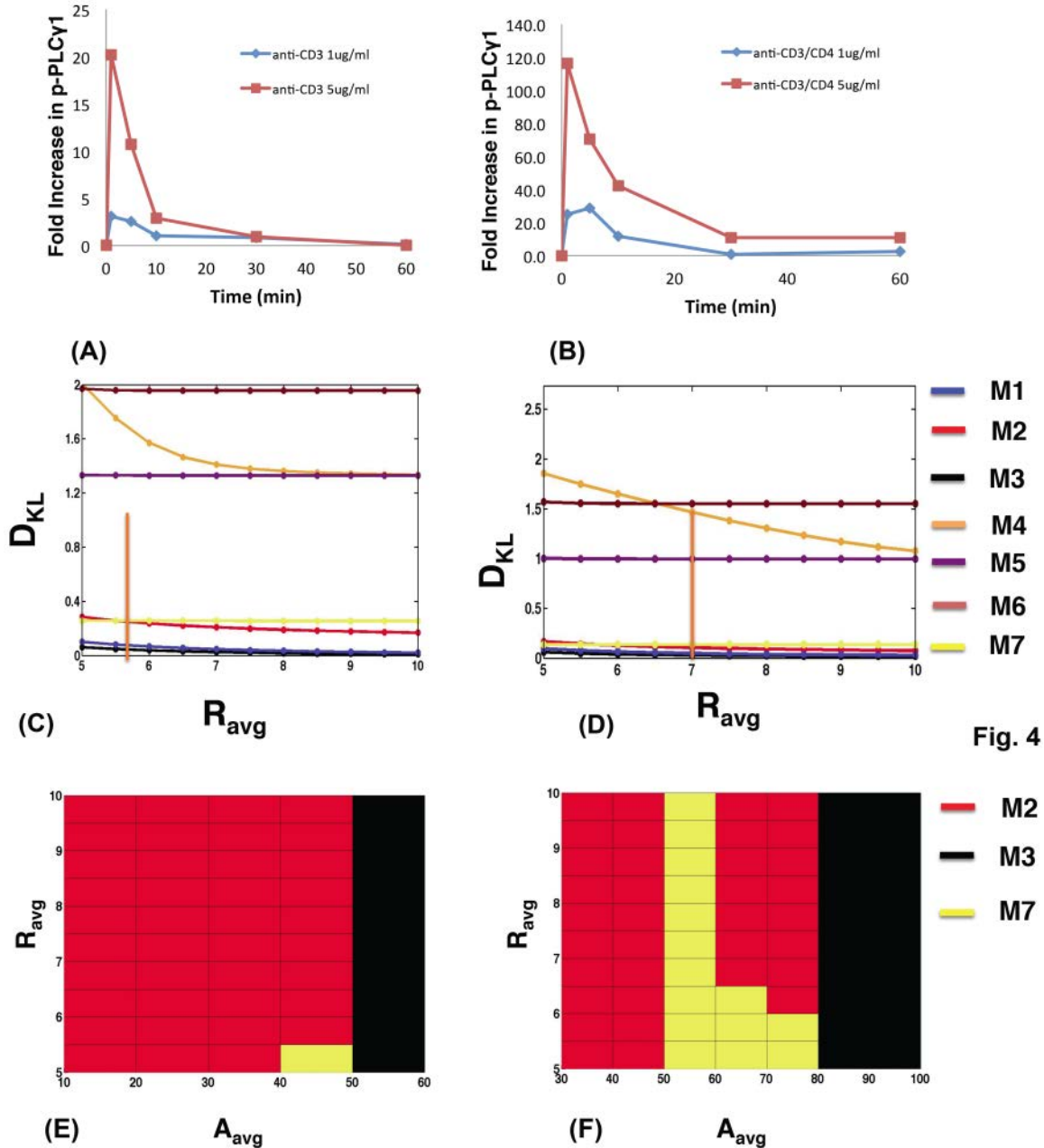


Fig. 4. Models containing Itk dimers and dueling feedbacks also show higher robustness for polyclonal T cells stimulated by anti-CD3 antibodies. PLC γ 1 phosphorylation kinetics in $MHC^{-/-}$ T cells stimulated by antibodies against (A) CD3 or (B) CD3 and CD4 at 1 μ g/ml versus 5 μ g/ml. (C) Variation of D_{KL} with R for the *in silico*

models M1-M3 (blue, red and black, respectively), M7 (yellow), and M5-M6 (purple and maroon, respectively) at initial Itk ($\text{Itk}^0 = 100$ molecules) and PIP_3 concentrations ($\text{PIP}_3^0 = 370$ molecules) at $\tau_p = 1$ min and $A = 60$ molecules, representing anti-CD3 stimulation at $5 \mu\text{g/ml}$. The orange bar indicates R^{expt} . Note we use A to represent the amplitude A^{expt} in experiments measuring fold change in Itk phosphorylation (see the main text for further details). (D) Variation of D_{KL} with R for anti-CD3/CD4 stimulation at $5 \mu\text{g/ml}$ at $\tau_p = 1$ min and $A = 80$ molecules. The initial Itk ($\text{Itk}^0 = 140$ molecules) and PIP_3 concentrations ($\text{PIP}_3^0 = 530$ molecules) were used. The orange bar indicates R^{expt} . (E) and (F) show maps of the most robust models (with the lowest D_{KL}) as R^{expt} and A (shown as A_{avg}) are varied for the same parameters as in (C) and (D), respectively.

References

1. Irvine RF, Schell MJ (2001) Back in the water: the return of the inositol phosphates. *Nature reviews Molecular cell biology* 2: 327-338.
2. Huang YH, Grasis JA, Miller AT, Xu R, Soonthornvacharin S, et al. (2007) Positive regulation of Itk PH domain function by soluble IP4. *Science* 316: 886-889.
3. Sauer K, Cooke MP (2010) Regulation of immune cell development through soluble inositol-1,3,4,5-tetrakisphosphate. *Nature reviews Immunology* 10: 257-271.
4. Schell MJ (2010) Inositol trisphosphate 3-kinases: focus on immune and neuronal signaling. *Cell Mol Life Sci* 67: 1755-1778.
5. York JD (2006) Regulation of nuclear processes by inositol polyphosphates. *Biochim Biophys Acta* 1761: 552-559.
6. Pouillon V, Hascakova-Bartova R, Pajak B, Adam E, Bex F, et al. (2003) Inositol 1,3,4,5-tetrakisphosphate is essential for T lymphocyte development. *Nat Immunol* 4: 1136-1143.
7. Wen BG, Pletcher MT, Warashina M, Choe SH, Ziaee N, et al. (2004) Inositol (1,4,5) trisphosphate 3 kinase B controls positive selection of T cells and modulates Erk activity. *Proc Natl Acad Sci U S A* 101: 5604-5609.
8. Gascoigne NR, Palmer E (2011) Signaling in thymic selection. *Curr Opin Immunol* 23: 207-212.
9. Starr TK, Jameson SC, Hogquist KA (2003) Positive and negative selection of T cells. *Annu Rev Immunol* 21: 139-176.
10. Stritesky GL, Jameson SC, Hogquist KA (2011) Selection of Self-Reactive T Cells in the Thymus. *Annu Rev Immunol*.
11. Jordan MS, Boesteanu A, Reed AJ, Petrone AL, Holenbeck AE, et al. (2001) Thymic selection of CD4+CD25+ regulatory T cells induced by an agonist self-peptide. *Nat Immunol* 2: 301-306.
12. Moon JJ, Dash P, Oguin TH, McClaren JL, Chu HH, et al. (2011) Quantitative impact of thymic selection on Foxp3(+) and Foxp3(-) subsets of self-peptide/MHC class II-specific CD4(+) T cells. *Proceedings of the National Academy of Sciences of the United States of America* 108: 14602-14607.

13. Heyeck SD, Wilcox HM, Bunnell SC, Berg LJ (1997) Lck phosphorylates the activation loop tyrosine of the Itk kinase domain and activates Itk kinase activity. *J Biol Chem* 272: 25401-25408.
14. Sauer K, Cooke MP (2010) Regulation of immune cell development through soluble inositol-1,3,4,5-tetrakisphosphate. *Nat Rev Immunol* 10: 257-271.
15. Thome M, Charton JE, Pelzer C, Hailfinger S (2010) Antigen receptor signaling to NF-kappaB via CARMA1, BCL10, and MALT1. *Cold Spring Harb Perspect Biol* 2: a003004.
16. Huang YH, Sauer K (2010) Lipid signaling in T-cell development and function. *Cold Spring Harb Perspect Biol* 2: a002428.
17. Okoh MP, Vihinen M (1999) Pleckstrin homology domains of tec family protein kinases. *Biochem Biophys Res Commun* 265: 151-157.
18. Jia Y, Loison F, Hattori H, Li Y, Erneux C, et al. (2008) Inositol trisphosphate 3-kinase B (InsP3KB) as a physiological modulator of myelopoiesis. *Proc Natl Acad Sci U S A* 105: 4739-4744.
19. Jia Y, Subramanian KK, Erneux C, Pouillon V, Hattori H, et al. (2007) Inositol 1,3,4,5-tetrakisphosphate negatively regulates phosphatidylinositol-3,4,5-trisphosphate signaling in neutrophils. *Immunity* 27: 453-467.
20. Sauer K, Park E, Siegemund S, French AR, Wahle JA, et al. (2013) Inositol tetrakisphosphate limits NK cell effector functions by controlling PI3K signaling. *Blood* 121: 286-297.
21. Irvine R (2007) Cell signaling. The art of the soluble. *Science* 316: 845-846.
22. Andreotti AH, Schwartzberg PL, Joseph RE, Berg LJ (2010) T-cell signaling regulated by the Tec family kinase, Itk. *Cold Spring Harb Perspect Biol* 2: a002287.
23. Severin A, Joseph RE, Boyken S, Fulton DB, Andreotti AH (2009) Proline isomerization preorganizes the Itk SH2 domain for binding to the Itk SH3 domain. *J Mol Biol* 387: 726-743.
24. Colgan J, Asmal M, Neagu M, Yu B, Schneidkraut J, et al. (2004) Cyclophilin A regulates TCR signal strength in CD4+ T cells via a proline-directed conformational switch in Itk. *Immunity* 21: 189-201.
25. Laederach A, Cradic KW, Fulton DB, Andreotti AH (2003) Determinants of intra versus intermolecular self-association within the regulatory domains of Rlk and Itk. *J Mol Biol* 329: 1011-1020.
26. Min L, Wu W, Joseph RE, Fulton DB, Berg L, et al. (2010) Disrupting the intermolecular self-association of Itk enhances T cell signaling. *J Immunol* 184: 4228-4235.
27. Qi Q, August A (2009) The Tec family kinase Itk exists as a folded monomer in vivo. *J Biol Chem* 284: 29882-29892.
28. Qi Q, Sahu N, August A (2006) Tec kinase Itk forms membrane clusters specifically in the vicinity of recruiting receptors. *J Biol Chem* 281: 38529-38534.
29. Engelman JA, Luo J, Cantley LC (2006) The evolution of phosphatidylinositol 3-kinases as regulators of growth and metabolism. *Nat Rev Genet* 7: 606-619.

30. Wong KK, Engelman JA, Cantley LC (2010) Targeting the PI3K signaling pathway in cancer. *Curr Opin Genet Dev* 20: 87-90.
31. Jaynes ET (1957) Information Theory and Statistical Mechanics .2. *Physical Review* 108: 171-190.
32. Jaynes ET (1957) Information Theory and Statistical Mechanics. *Physical Review* 106: 620-630.
33. Jaynes ET, Bretthorst GL (2003) Probability theory : the logic of science. Cambridge, UK ; New York: Cambridge University Press. xxix, 727 p. p.
34. Kitano H (2004) Biological robustness. *Nat Rev Genet* 5: 826-837.
35. Costello PS, Gallagher M, Cantrell DA (2002) Sustained and dynamic inositol lipid metabolism inside and outside the immunological synapse. *Nature immunology* 3: 1082-1089.
36. Insall RH, Weiner OD (2001) PIP3, PIP2, and cell movement--similar messages, different meanings? *Developmental cell* 1: 743-747.
37. Stephens LR, Jackson TR, Hawkins PT (1993) Agonist-stimulated synthesis of phosphatidylinositol(3,4,5)-trisphosphate: a new intracellular signalling system? *Biochimica et biophysica acta* 1179: 27-75.
38. Kampen NGv (1992) Stochastic processes in physics and chemistry. Amsterdam ; New York: North-Holland. xiv, 465 p. p.
39. Rebecchi MJ, Scarlata S (1998) Pleckstrin homology domains: a common fold with diverse functions. *Annual review of biophysics and biomolecular structure* 27: 503-528.
40. Daniels MA, Teixeira E, Gill J, Hausmann B, Roubaty D, et al. (2006) Thymic selection threshold defined by compartmentalization of Ras/MAPK signalling. *Nature* 444: 724-729.
41. Sommers CL, Lee J, Steiner KL, Gurson JM, Depersis CL, et al. (2005) Mutation of the phospholipase C-gamma1-binding site of LAT affects both positive and negative thymocyte selection. *J Exp Med* 201: 1125-1134.
42. Fu G, Chen Y, Yu M, Podd A, Schuman J, et al. (2010) Phospholipase C{gamma}1 is essential for T cell development, activation, and tolerance. *J Exp Med* 207: 309-318.
43. Liu YW, Neumann S, Ramachandran R, Ferguson SM, Pucadyil TJ, et al. (2011) Differential curvature sensing and generating activities of dynamin isoforms provide opportunities for tissue-specific regulation. *Proceedings of the National Academy of Sciences of the United States of America* 108: E234-242.
44. Eungdamrong NJ, Iyengar R (2004) Modeling cell signaling networks. *Biol Cell* 96: 355-362.
45. Phillips R, Kondev J, Theriot J (2009) Physical biology of the cell. New York: Garland Science. xxiv, 807 p. p.
46. Lemmon MA (2008) Membrane recognition by phospholipid-binding domains. *Nature reviews Molecular cell biology* 9: 99-111.
47. Elowitz MB, Levine AJ, Siggia ED, Swain PS (2002) Stochastic gene expression in a single cell. *Science* 297: 1183-1186.

48. Feinerman O, Veiga J, Dorfman JR, Germain RN, Altan-Bonnet G (2008) Variability and robustness in T cell activation from regulated heterogeneity in protein levels. *Science* 321: 1081-1084.
49. Cohen-Saidon C, Cohen AA, Sigal A, Liron Y, Alon U (2009) Dynamics and variability of ERK2 response to EGF in individual living cells. *Mol Cell* 36: 885-893.
50. Houtman JC, Higashimoto Y, Dimasi N, Cho S, Yamaguchi H, et al. (2004) Binding specificity of multiprotein signaling complexes is determined by both cooperative interactions and affinity preferences. *Biochemistry* 43: 4170-4178.
51. Lin J, Weiss A (2001) Identification of the minimal tyrosine residues required for linker for activation of T cell function. *J Biol Chem* 276: 29588-29595.
52. Kim J, Heslop-Harrison P, Postlethwaite I, Bates DG (2007) Stochastic noise and synchronisation during dictyostelium aggregation make cAMP oscillations robust. *PLoS computational biology* 3: e218.
53. Laub MT, Loomis WF (1998) A molecular network that produces spontaneous oscillations in excitable cells of Dictyostelium. *Molecular biology of the cell* 9: 3521-3532.
54. Geva-Zatorsky N, Rosenfeld N, Itzkovitz S, Milo R, Sigal A, et al. (2006) Oscillations and variability in the p53 system. *Molecular systems biology* 2: 2006 0033.
55. Kitano H (2007) Towards a theory of biological robustness. *Molecular systems biology* 3: 137.
56. Nurse P, Hayles J (2011) The cell in an era of systems biology. *Cell* 144: 850-854.
57. Stelling J, Sauer U, Szallasi Z, Doyle FJ, 3rd, Doyle J (2004) Robustness of cellular functions. *Cell* 118: 675-685.
58. Chau AH, Walter JM, Gerardin J, Tang C, Lim WA (2012) Designing synthetic regulatory networks capable of self-organizing cell polarization. *Cell* 151: 320-332.
59. Kullback S (1959) *Information theory and statistics*. New York,: Wiley. 395 p. p.
60. Moran AE, Hogquist KA (2012) T-cell receptor affinity in thymic development. *Immunology* 135: 261-267.
61. Juang J, Ebert PJR, Feng D, Garcia KC, Krogsgaard M, et al. (2010) Peptide-MHC heterodimers show that thymic positive selection requires a more restricted set of self-peptides than negative selection. *The Journal of Experimental Medicine* 207: 1223-1234.
62. Landau LD, Lifshits EM (1958) *Statistical physics*. London, Reading, Mass.,: Pergamon Press; Addison-Wesley Pub. Co. 484 p. p.
63. Cover TM, Thomas JA (2006) *Elements of information theory*. Hoboken, N.J.: Wiley-Interscience. xxiii, 748 p. p.
64. Hamann JR, Bianchi LM (1970) Stochastic Population Mechanics in Relational Systems Formalism - Volterra-Lotka Ecological Dynamics. *Journal of Theoretical Biology* 28: 175-&.

65. Phillips SJ, Anderson RP, Schapire RE (2006) Maximum entropy modeling of species geographic distributions. *Ecological Modelling* 190: 231-259.
66. Bialek W, Cavagna A, Giardina I, Mora T, Silvestri E, et al. (2012) Statistical mechanics for natural flocks of birds. *Proceedings of the National Academy of Sciences of the United States of America* 109: 4786-4791.
67. Schneidman E, Berry MJ, Segev R, Bialek W (2006) Weak pairwise correlations imply strongly correlated network states in a neural population. *Nature* 440: 1007-1012.
68. Xu TR, Vyshemirsky V, Gormand A, von Kriegsheim A, Girolami M, et al. (2010) Inferring Signaling Pathway Topologies from Multiple Perturbation Measurements of Specific Biochemical Species (vol 3, pg 134, 2010). *Science Signaling* 3.
69. Blinov ML, Faeder JR, Goldstein B, Hlavacek WS (2004) BioNetGen: software for rule-based modeling of signal transduction based on the interactions of molecular domains. *Bioinformatics* 20: 3289-3291.
70. Cohen SD, Hindmarsh, A. C. (1996) CVODE, a stiff/nonstiff ODE solver in C. *Computers in Physics* 10: 138-143.
71. Volfson D, Marciniak J, Blake WJ, Ostroff N, Tsimring LS, et al. (2006) Origins of extrinsic variability in eukaryotic gene expression. *Nature* 439: 861-864.

Table I: Molecular models describing interactions between Itk, IP₄ and PIP₃.

	M1	M2	M3	M7	M4	M5	M6
	Contain IP ₄ induced +ve feedback					No +ve feedback	
	Contain Itk dimers				Contains Itk monomers	Contains Itk dimers	Contains Itk monomers
Effect of IP₄ binding to one PH domain of an Itk dimer	Increase the affinity of the other PH domain toward IP ₄ and PIP ₃ .	Same as in M1.	Same as in M1.	Increase the affinity of the other PH domain toward PIP ₃ and IP ₄ .	IP ₄ and PIP ₃ bind to the Itk PH domain with weak affinities. However, IP ₄ bound to Itk gets replaced by PIP ₃ with high affinity, and then the PIP ₃ bound to Itk can get replaced by IP ₄ with high affinity.	No change in affinity	The monomeric PH domain binds IP ₄ and PIP ₃ with equal but always low affinity.
Effect of PIP₃ binding to one PH domain of an Itk dimer	Increase the affinity of the other PH domain for IP ₄ and PIP ₃ .	<i>Does not increase the affinity of the other PH domain for IP₄ or PIP₃.</i>	Increase the affinity of the other PH domain only for IP ₄ but <i>not</i> for PIP ₃ .	Increase the affinity of the other PH domain for PIP ₃ but <i>not</i> for IP ₄ .		No change in affinity	
Number of parameters (Rate constants + initial concentrations)	5 + 3	5 + 3	5 + 3	5 + 3	4 + 3	3 + 3	3 + 3

Table II: Values of peak time, peak width, and asymmetry ratio R calculated from the PLC γ 1 activation kinetics in Fig. 3 for different ligands.

Ligand	Peak time (τ_p) (min)	Peak width (τ_w) (min)	R
OVA	2.0	3.9	1.9
Q4R7	2.0	8.6	4.3
Q4H7	2.0	7.5	3.8
G4	2.0	4.3	2.1

Supplementary Information for “*In silico* Modeling of Itk Activation Kinetics in Thymocytes Suggests Competing Positive and Negative IP₄ Mediated Feedbacks Increase Robustness ”

Details of the models and simulations:

We used a set of ODEs to describe the signaling kinetics of concentrations of proteins and lipids in the system. The descriptions of the kinetics using ODEs neglect stochastic fluctuations arising from intrinsic noise fluctuations and assume a spatially well-mixed system. This is a good approximation when diffusion time scales are fast compared to the reaction time scales. Since the time scales for diffusion depend on the spatial extent of the system, the system can be assumed to be spatially homogeneous in a region of volume V (Fig. S1A), which is small compared to the total volume of a T cell. In addition, the signaling reactions in our system can take place between a pair of molecules, where both species reside in the plasma membrane. For these reactions, we convert the values of binding rates given in three dimensions to approximate two dimensional rates. We provide details regarding the above approximations below. The reactions are shown in Tables S1-S7, and the corresponding ODEs are shown below the tables. The model reactions are also shown graphically in Fig. S1B. The software package, BIONETGEN, was used to construct and solve the ODEs. The BIONETGEN codes are available at <http://planetx.nationwidechildrens.org/~jayajit/>.

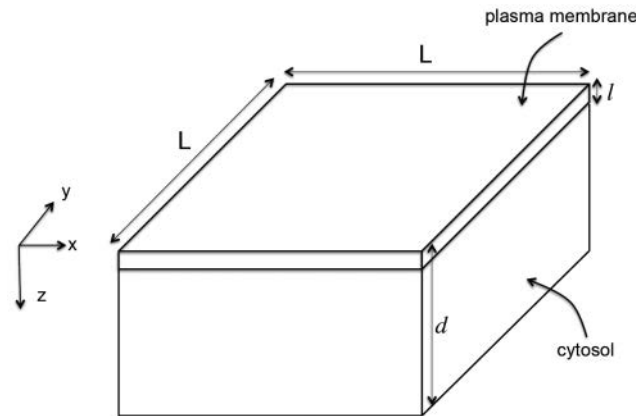


Fig. S1A. Details of the simulation box. We used $L=2 \mu\text{m}$, $l=2 \text{nm}$ and $d=0.02 \mu\text{m}$ for our simulations.

The simulation box (Fig. S1A) is divided into two compartments, plasma membrane and cytosol. The molecules in the cytosol can react with the plasma membrane bound molecules only when they are in a close proximity ($\sim l=2 \text{nm}$, Fig. S1). This length scale is used to convert three dimensional reaction rates to two dimensional reaction rates describing reactions in the plasma membrane. The area of the plasma membrane is taken to be $4 \mu\text{m}^2$ ($L \times L$ in Fig. S1). The volume of the cytosol is $0.08 \mu\text{m}^3$ ($L \times L \times d$ in Fig. S1) and the volume of the plasma membrane compartment is $0.008 \mu\text{m}^3$ ($L \times L \times 0.002 \mu\text{m}$). All the molecular species were distributed homogeneously across the simulation box. This is a good assumption when the time scales of diffusion of the molecules are much faster compared to the fastest reaction time scale. Since the fastest reaction time scale ($\sim 10 \text{s}$, corresponding to unbinding rate of $\text{Itk} - \text{PIP}_3$, see the tables below) is comparable to the

slowest diffusion time scales ($D \sim 0.1 \mu\text{m}^2/\text{s}$ for membrane bound species (1)) on the length scale ($2 \mu\text{m}$) of the simulation box, we assumed the plasma membrane bound species to be homogeneously distributed in space. The cytosolic molecules diffuse with a much faster time scale ($D \sim 10 \mu\text{m}^2/\text{s}$ (1)) compared to the plasma membrane bound molecules, therefore, we also assumed that those molecules are also homogeneously distributed in the simulation box.

ODEs for Model 1: The reactions for Model 1 are given in the table below. The corresponding ODEs are shown below the table.

Table S1: Reactions and rate constants for model M1.

Reactions	k_{on} ($\mu\text{M}^{-1}\text{s}^{-1}$)	k_{off} (s^{-1})	K_{D} (μM)	k_{cat} ($\mu\text{M}^{-1}\text{s}^{-1}$)
$\text{Itk} - \text{Itk} + \text{PIP}_3 \leftrightarrow \text{Itk} - \text{Itk} - \text{PIP}_3$	2.5×10^{-4}	0.1	400 *	
$\text{PIP}_3 - \text{Itk} - \text{Itk} + \text{PIP}_3 \leftrightarrow \text{PIP}_3 - \text{Itk} - \text{Itk} - \text{PIP}_3$	0.01	0.003	0.3 *	
$\text{Itk} - \text{Itk} + \text{IP}_4 \leftrightarrow \text{Itk} - \text{Itk} - \text{IP}_4$	2.5×10^{-3}	0.1	40 *	
$\text{PIP}_3 - \text{Itk} - \text{Itk} + \text{IP}_4 \leftrightarrow \text{PIP}_3 - \text{Itk} - \text{Itk} - \text{IP}_4$	0.1	0.003	0.03 † (2)	
$\text{IP}_4 - \text{Itk} - \text{Itk} + \text{PIP}_3 \leftrightarrow \text{IP}_4 - \text{Itk} - \text{Itk} - \text{PIP}_3$	0.01	0.003	0.3 † (2)	
$\text{IP}_4 - \text{Itk} - \text{Itk} + \text{IP}_4 \leftrightarrow \text{IP}_4 - \text{Itk} - \text{Itk} - \text{IP}_4$	0.1	0.003	0.03 † (2)	
$\text{Itk} - \text{Itk} - \text{PIP}_3 + \text{S} \leftrightarrow \text{IP}_4 + \text{Itk} - \text{Itk} - \text{PIP}_3$				1.5×10^{-4} **
$\text{IP}_4 - \text{Itk} - \text{Itk} - \text{PIP}_3 + \text{S} \leftrightarrow \text{IP}_4 + \text{IP}_4 - \text{Itk} - \text{Itk} - \text{PIP}_3$				1.5×10^{-4} **
$\text{PIP}_3 - \text{Itk} - \text{Itk} - \text{PIP}_3 + \text{S} \rightarrow \text{IP}_4 + \text{PIP}_3 - \text{Itk} - \text{Itk} - \text{PIP}_3$				1.5×10^{-4} **

† The high affinity binding of IP_4 to the PH domain is taken to be in the nano-molar range based on the binding affinity of the isolated Btk PH domain for both IP_4 and PIP_3 (2). The binding affinity of the Itk PH domain for IP_4 or PIP_3 however is not known. The K_{D} for PIP_3 binding to the isolated Btk PH domain is reported to be 7 times higher than the IP_4 binding (2). For convenience we have taken it to be 10 times larger.

* Estimated. The low affinity binding of Itk PH domains to IP_4/PIP_3 has been assumed to be 1000 times weaker than the high affinity binding.

** Estimated. Hydrolysis of PIP_2 and subsequent production of IP_3 , release of Ca^{2+} from the endoplasmic stores, Ca^{2+} /Calmodulin dependent activation of ItpkB, and, finally the enzymatic turnover of IP_3 by ItpkB have all been subsumed into the one single step where membrane bound Itk cleaves PIP_2 to produce IP_4 . The rate constant for the above reaction is chosen to match the time scale of $\text{PLC}\gamma 1$ activation reported in the experiments (3). PIP_2 is denoted as S for convenience.

Construction of the ODEs describing the signaling kinetics.

The molecular species, Itk-Itk (we denote this species by Itk_D), representing Itk-Itk dimers bound to the TCR and LAT signalosome, resides at the interface of the plasma membrane and the cytosol. The lipid PIP₃, and the Itk-Itk-PIP₃ complexes (Itk-Itk-PIP₃, IP₄-Itk-Itk-PIP₃), and PIP₂ (denoted as S) also reside in the plasma membrane. The molecules IP₄ and IP₄-Itk-Itk-IP₄ are soluble and dwell in the cytosol. We use two well-mixed compartments representing plasma membrane and cytosol (Fig. S1A) and use ODEs to describe the kinetics for the molecules in those compartments. E.g., concentration of Itk_D or [Itk_D] at a time t is given by,

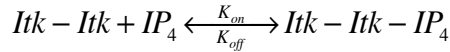
$$[Itk_D](t) = \frac{N_{Itk_D}(t)}{Al} \theta(z+l) , \text{ where, } N_{Itk_D}(t) \text{ denotes the total number of Itk dimers in the}$$

system, and $\theta(z)$ is the Heaveside step function defined as, $\theta(z) = 0$ for $z < 0$, and, $\theta(z) = 1$ for $z \geq 0$. In the simulation box, z ranges from $z=0$ to $z=-d$. The region between $0 \geq z \geq -l$ represents the plasma membrane and $-l \geq z \geq -d$ represents the cytosolic part in the simulation. All the plasma membrane bound species concentrations are defined as above. The concentration of cytosolic IP₄ is given by,

$$[IP_4](t) = \frac{N_{IP_4}(t)}{A(d-l)} \theta(z+d)\theta(z-l) \approx \frac{N_{IP_4}(t)}{Ad} \theta(z+d)\theta(z-l) . \text{ The last approximation}$$

follows as $l(= 2nm) \ll d(= 0.02\mu m)$. Concentrations of all the cytosolic species are defined in the same way. Using the scheme described above we write down the ODEs describing kinetics for the total concentrations of the species present in the model. Below we show how the ODEs are constructed from the reactions using an example.

Consider the following reaction



, where K_{on} and K_{off} are the binding and the unbinding rates respectively. Using the law of mass action the time evolution of the Itk-Itk-IP₄ complex can be written as

$$\frac{d[Itk - Itk - IP_4]}{dt} = K_{on}[Itk - Itk][IP_4] - K_{off}[Itk - Itk - IP_4] .$$

The species Itk-Itk-IP₄ and Itk-Itk reside in the plasma membrane whereas IP₄ resides in

the cytosol. Therefore, as described above, $[Itk - Itk - IP_4](t) = \frac{N_{Itk-Itk-IP_4}(t)}{Al} \theta(z+l)$,

$$[Itk - Itk](t) = \frac{N_{Itk-Itk}(t)}{Al} \theta(z+l) , \text{ and } [IP_4](t) \text{ is related to } N_{IP_4} \text{ as described previously.}$$

We denote, $V_{\text{membrane}} = Al$ and $Ad = V_{\text{cytosol}} = Ad$. Multiplying the above rate equation by V_{membrane} , we get,

$$\frac{dN_{Itk-Itk-IP_4}}{dt} = \frac{K_{on}}{V_{cytosol}} N_{Itk-Itk} N_{IP_4} - K_{off} N_{Itk-Itk-IP_4}$$

Note that the rate, K_{on} , for a binding

reaction between a plasma membrane bound molecule and a cytosolic molecule, is scaled by the volume of the cytosol whereas the K_{off} remains the same. For a reaction like $Itk - Itk + PIP_3 \xrightleftharpoons[K_{off}]{K_{on}} Itk - Itk - PIP_3$, where all the molecular species reside in the plasma membrane we find,

$$\frac{dN_{Itk-Itk-PIP_3}}{dt} = \frac{K_{on}}{V_{membrane}} N_{Itk-Itk} N_{PIP_3} - K_{off} N_{Itk-Itk-PIP_3}.$$

The on rate, K_{on} , is scaled by the volume of the membrane $V_{membrane}$ instead of the $V_{cytosol} = Ad$. Following the above procedure we write the ODEs for the model M1. For convenience we denote the Itk-Itk dimer as Itk_D . We do not show the volume scaling factors explicitly, all the rates shown in the ODEs have the unit of $[\text{time}]^{-1}$. These rates are calculated using the values given in Table S1 and then scaling those values with appropriate volume factors.

$$\begin{aligned}
\frac{dN_{Itk_D}}{dt} &= k_{-1}N_{Itk_D-PIP_3} - k_1N_{Itk_D}N_{PIP_3} + k_{-2}N_{Itk_D-IP_4} - k_2N_{Itk_D}N_{IP_4} \\
\frac{dN_{Itk_D-PIP_3}}{dt} &= k_1N_{Itk_D}N_{PIP_3} - k_{-1}N_{Itk_D-PIP_3} + 2\tilde{k}_{-1}N_{PIP_3-Itk_D-PIP_3} \\
&\quad - \tilde{k}_1N_{Itk_D-PIP_3}N_{PIP_3} + \tilde{k}_{-2}N_{IP_4-Itk_D-PIP_3} - \tilde{k}_2N_{Itk_D-PIP_3}N_{IP_4} \\
\frac{dN_{Itk_D-IP_4}}{dt} &= k_2N_{Itk_D}N_{IP_4} - k_{-2}N_{Itk_D-IP_4} + 2\tilde{k}_{-2}N_{IP_4-Itk_D-IP_4} - \tilde{k}_2N_{Itk_D-IP_4}N_{IP_4} \\
&\quad + \tilde{k}_{-1}N_{IP_4-Itk_D-PIP_3} - \tilde{k}_1N_{Itk_D-IP_4}N_{PIP_3} \\
\frac{dN_{PIP_3}}{dt} &= k_{-1}N_{Itk_D-PIP_3} - k_1N_{Itk_D}N_{PIP_3} + 2\tilde{k}_{-1}N_{PIP_3-Itk_D-PIP_3} - \tilde{k}_1N_{Itk_D-PIP_3}N_{PIP_3} \\
&\quad + \tilde{k}_{-1}N_{IP_4-Itk_D-PIP_3} - \tilde{k}_1N_{Itk_D-IP_4}N_{PIP_3} \\
\frac{dN_{PIP_3-Itk_D-PIP_3}}{dt} &= \tilde{k}_1N_{Itk_D-PIP_3}N_{PIP_3} - 2\tilde{k}_{-1}N_{PIP_3-Itk_D-PIP_3} \\
\frac{dN_{IP_4-Itk_D-PIP_3}}{dt} &= \tilde{k}_1N_{Itk_D-IP_4}N_{PIP_3} - \tilde{k}_{-1}N_{IP_4-Itk_D-PIP_3} + \tilde{k}_2N_{Itk_D-PIP_3}N_{IP_4} \\
&\quad - \tilde{k}_{-2}N_{IP_4-Itk_D-PIP_3} \\
\frac{dN_{IP_4-Itk_D-IP_4}}{dt} &= \tilde{k}_2N_{Itk_D-IP_4}N_{IP_4} - 2\tilde{k}_{-2}N_{IP_4-Itk_D-IP_4} \\
\frac{dN_{IP_4}}{dt} &= 2\tilde{k}_{-2}N_{IP_4-Itk_D-IP_4} - \tilde{k}_2N_{Itk_D-IP_4}N_{IP_4} + \tilde{k}_{-2}N_{IP_4-Itk_D-PIP_3} - \tilde{k}_2N_{Itk_D-PIP_3}N_{IP_4} \\
&\quad + k_{-2}N_{Itk_D-IP_4} - k_2N_{Itk_D}N_{IP_4} \\
&\quad + k_3 \left\{ N_{IP_4-Itk_D-PIP_3} + N_{Itk_D-PIP_3} + N_{PIP_3-Itk_D-PIP_3} \right\} N_S \\
\frac{dN_S}{dt} &= -k_3 \left\{ N_{IP_4-Itk_D-PIP_3} + N_{Itk_D-PIP_3} + N_{PIP_3-Itk_D-PIP_3} \right\} N_S
\end{aligned}$$

There are three conservation laws, namely

$$\begin{aligned}
N_{Itk_D} + N_{Itk_D-PIP_3} + N_{PIP_3-Itk_D-PIP_3} + N_{IP_4-Itk_D-PIP_3} + N_{IP_4-Itk_D-IP_4} &= N_{Itk_D}(t=0) \\
N_{PIP_3} + N_{Itk_D-PIP_3} + N_{IP_4-Itk_D-PIP_3} + 2 * N_{PIP_3-Itk_D-PIP_3} &= N_{PIP_3}(t=0) \\
N_{IP_4} + N_{Itk_D-IP_4} + N_{IP_4-Itk_D-PIP_3} + 2 * N_{IP_4-Itk_D-IP_4} + N_S &= N_S(t=0)
\end{aligned}$$

the equations above give the time evolution of all the proteins and the protein complexes.

ODEs for Model 2: The reactions for Model 2 are given in the table below. The corresponding ODEs are shown below the table.

Table S2: Reactions and rate constants for model M2.

Reactions	k_{on} ($\mu\text{M}^{-1}\text{s}^{-1}$)	k_{off} (s^{-1})	K_D (μM)	k_{cat} ($\mu\text{M}^{-1}\text{s}^{-1}$)
$I_{tk} - I_{tk} + PIP_3 \leftrightarrow I_{tk} - I_{tk} - PIP_3$	2.5×10^{-4}	0.1	400	
$I_{tk} - I_{tk} + IP_4 \leftrightarrow I_{tk} - I_{tk} - IP_4$	2.5×10^{-3}	0.1	40	
$PIP_3 - I_{tk} - I_{tk} + IP_4 \leftrightarrow PIP_3 - I_{tk} - I_{tk} - IP_4$	2.5×10^{-3}	0.1	40	
$IP_4 - I_{tk} - I_{tk} + PIP_3 \leftrightarrow IP_4 - I_{tk} - I_{tk} - PIP_3$	0.01	0.003	0.3	
$IP_4 - I_{tk} - I_{tk} + IP_4 \leftrightarrow IP_4 - I_{tk} - I_{tk} - IP_4$	0.1	0.003	0.03	
$I_{tk} - I_{tk} - PIP_3 + S \leftrightarrow IP_4 + I_{tk} - I_{tk} - PIP_3$				1.5×10^{-4}
$IP_4 - I_{tk} - I_{tk} - PIP_3 + S \leftrightarrow IP_4 + IP_4 - I_{tk} - I_{tk} - PIP_3$				1.5×10^{-4}

All the high and low affinity binding of I_{tk} PH domains with PIP₃ and IP₄, and, the IP₄ production rate are taken to be the same as that shown for model M1 (Table S1).

$$\frac{dN_{I_{tk}_D}}{dt} = k_{-1}N_{I_{tk}_D-PIP_3} - k_1N_{I_{tk}_D}N_{PIP_3} + k_{-2}N_{I_{tk}_D-IP_4} - k_2N_{I_{tk}_D}N_{IP_4}$$

$$\frac{dN_{I_{tk}_D-PIP_3}}{dt} = k_1N_{I_{tk}_D}N_{PIP_3} - k_{-1}N_{I_{tk}_D-PIP_3} + \tilde{k}_{-2}N_{IP_4-I_{tk}_D-PIP_3} - \tilde{k}_2N_{I_{tk}_D-PIP_3}N_{IP_4}$$

$$\begin{aligned} \frac{dN_{I_{tk}_D-IP_4}}{dt} &= k_2N_{I_{tk}_D}N_{IP_4} - k_{-2}N_{I_{tk}_D-IP_4} + 2\tilde{k}_{-2}N_{IP_4-I_{tk}_D-IP_4} - \tilde{k}_2N_{I_{tk}_D-IP_4}N_{IP_4} \\ &\quad + \tilde{k}_{-1}N_{IP_4-I_{tk}_D-PIP_3} - \tilde{k}_1N_{I_{tk}-IP_4}N_{PIP_3} \end{aligned}$$

$$\frac{dN_{PIP_3}}{dt} = k_{-1}N_{I_{tk}_D-PIP_3} - k_1N_{I_{tk}_D}N_{PIP_3} + \tilde{k}_{-1}N_{IP_4-I_{tk}_D-PIP_3} - \tilde{k}_1N_{I_{tk}-IP_4}N_{PIP_3}$$

$$\begin{aligned} \frac{dN_{IP_4-I_{tk}_D-PIP_3}}{dt} &= \tilde{k}_1N_{I_{tk}-IP_4}N_{PIP_3} - \tilde{k}_{-1}N_{IP_4-I_{tk}_D-PIP_3} + \tilde{k}_2N_{I_{tk}_D-PIP_3}N_{IP_4} \\ &\quad - \tilde{k}_{-2}N_{IP_4-I_{tk}_D-PIP_3} \end{aligned}$$

$$\frac{dN_{IP_4-I_{tk}_D-IP_4}}{dt} = \tilde{k}_2N_{I_{tk}_D-IP_4}N_{IP_4} - 2\tilde{k}_{-2}N_{IP_4-I_{tk}_D-IP_4}$$

$$\begin{aligned} \frac{dN_{IP_4}}{dt} &= 2\tilde{k}_{-2}N_{IP_4-I_{tk}_D-IP_4} - \tilde{k}_2N_{I_{tk}_D-IP_4}N_{IP_4} + \tilde{k}_{-2}N_{IP_4-I_{tk}_D-PIP_3} - \tilde{k}_2N_{I_{tk}_D-PIP_3}N_{IP_4} \\ &\quad + k_{-2}N_{I_{tk}_D-IP_4} - k_2N_{I_{tk}_D}N_{IP_4} \\ &\quad + k_3 \left\{ N_{IP_4-I_{tk}_D-PIP_3} + N_{I_{tk}_D-PIP_3} \right\} N_S \end{aligned}$$

$$\frac{dN_S}{dt} = -k_3 \left\{ N_{IP_4-I_{tk}_D-PIP_3} + N_{I_{tk}_D-PIP_3} \right\} N_S$$

The conservation laws are,

$$N_{Itk_D} + N_{Itk_D-PIP_3} + N_{IP_4-Itk_D-PIP_3} + N_{IP_4-Itk_D-IP_4} = N_{Itk_D} (t=0)$$

$$N_{PIP_3} + N_{Itk_D-PIP_3} + N_{IP_4-Itk_D-PIP_3} = N_{PIP_3} (t=0)$$

$$N_{IP_4} + N_{Itk_D-IP_4} + N_{IP_4-Itk_D-PIP_3} + 2 * N_{IP_4-Itk_D-IP_4} + N_S = N_S (t=0)$$

ODEs for Model 3: The reactions for Model 3 are given in the table below. The corresponding ODEs are shown below the table.

Table S3: Reactions and rate constants for model M3.

Reactions	k_{on} ($\mu M^{-1}s^{-1}$)	k_{off} (s^{-1})	K_D (μM)	k_{cat} ($\mu M^{-1}s^{-1}$)
$Itk - Itk + PIP_3 \leftrightarrow Itk - Itk - PIP_3$	2.5×10^{-4}	0.1	400	
$Itk - Itk + IP_4 \leftrightarrow Itk - Itk - IP_4$	2.5×10^{-3}	0.1	40	
$PIP_3 - Itk - Itk + IP_4 \leftrightarrow PIP_3 - Itk - Itk - IP_4$	0.1	0.003	0.03	
$IP_4 - Itk - Itk + PIP_3 \leftrightarrow IP_4 - Itk - Itk - PIP_3$	0.01	0.003	0.3	
$IP_4 - Itk - Itk + IP_4 \leftrightarrow IP_4 - Itk - Itk - IP_4$	0.1	0.003	0.03	
$Itk - Itk - PIP_3 + S \leftrightarrow IP_4 + Itk - Itk - PIP_3$				1.5×10^{-4}
$IP_4 - Itk - Itk - PIP_3 + S \leftrightarrow IP_4 + IP_4 - Itk - Itk - PIP_3$				1.5×10^{-4}

All the high and low affinity binding of Itk PH domains with PIP_3 and IP_4 , and, the IP_4 production rate are taken to be the same as that shown for model M1 (Table S1).

The ODEs and the conservation laws are same as Model 2.

ODEs for Model 4: The reactions for Model 4 are given in the table below. The corresponding ODEs are shown below the table.

Table S4: Reactions and rate constants for model M4

Reactions	k_{on} ($\mu M^{-1}s^{-1}$)	k_{off} (s^{-1})	K_D (μM)	k_{cat} ($\mu M^{-1}s^{-1}$)
$Itk + PIP_3 \leftrightarrow Itk - PIP_3$	2.5×10^{-4}	0.1	400	
$Itk + IP_4 \leftrightarrow Itk^* - IP_4$	2.5×10^{-3}	0.1	40	
$Itk^* - IP_4 + PIP_3 \leftrightarrow Itk^* - PIP_3 + IP_4$	10 (we used this value to get similar kinetics as given by Ref. (3))			
$Itk^* - PIP_3 + S \rightarrow IP_4 + Itk^* - PIP_3$				1.5×10^{-4}

$Itk - PIP_3 + S \rightarrow IP_4 + Itk - PIP_3$				1.5×10^{-4}
--	--	--	--	----------------------

All the low affinity binding of Itk PH domains with PIP_3 and IP_4 , and, the IP_4 production rate are taken to be the same as that shown for model M1 (Table S1).

$$\begin{aligned} \frac{dN_{Itk}}{dt} &= k_{-1}N_{Itk-PIP_3} - k_1N_{Itk}N_{PIP_3} + k_{-2}N_{Itk^*-IP_4} - k_2N_{Itk}N_{IP_4} \\ \frac{dN_{Itk-PIP_3}}{dt} &= k_1N_{Itk}N_{PIP_3} - k_{-1}N_{Itk-PIP_3} \\ \frac{dN_{Itk^*-IP_4}}{dt} &= k_2N_{Itk}N_{IP_4} - k_{-2}N_{Itk^*-IP_4} + k_3N_{Itk^*-PIP_3}N_{IP_4} - k_3N_{Itk^*-IP_4}N_{PIP_3} \\ \frac{dN_{Itk^*-PIP_3}}{dt} &= k_3N_{Itk^*-IP_4}N_{PIP_3} - k_3N_{Itk^*-PIP_3}N_{IP_4} \\ \frac{dN_{PIP_3}}{dt} &= k_{-1}N_{Itk-PIP_3} - k_1N_{Itk}N_{PIP_3} + k_3N_{Itk^*-PIP_3}N_{IP_4} - k_3N_{Itk^*-IP_4}N_{PIP_3} \\ \frac{dN_{IP_4}}{dt} &= k_{-2}N_{Itk^*-IP_4} - k_2N_{Itk}N_{IP_4} + k_3N_{Itk^*-IP_4}N_{PIP_3} - k_3N_{Itk^*-PIP_3}N_{IP_4} \\ &\quad + k_4 \left\{ N_{Itk-PIP_3} + N_{Itk^*-PIP_3} \right\} N_S \\ \frac{dN_S}{dt} &= -k_4 \left\{ N_{Itk-PIP_3} + N_{Itk^*-PIP_3} \right\} N_S \end{aligned}$$

Here we have used Itk not Itk_D to denote the monomeric Itk molecules. The conservation laws are,

$$\begin{aligned} N_{Itk} + N_{Itk-PIP_3} + N_{Itk^*-IP_4} + N_{Itk^*-PIP_3} &= N_{Itk}(t=0) \\ N_{PIP_3} + N_{Itk^*-PIP_3} + N_{Itk-PIP_3} &= N_{PIP_3}(t=0) \\ N_{IP_4} + N_{Itk^*-IP_4} + N_S &= N_S(t=0) \end{aligned}$$

ODEs for Model 5: The reactions for Model 5 are given in the table below. The corresponding ODEs are shown below the table.

Table S5: Reactions and rate constants for model M5.

Reactions	k_{on} ($\mu M^{-1}s^{-1}$)	k_{off} (s^{-1})	K_D (μM)	k_{cat} ($\mu M^{-1}s^{-1}$)
$Itk - Itk + PIP_3 \leftrightarrow Itk - Itk - PIP_3$	1.25×10^{-4}	0.05	400	
$PIP_3 - Itk - Itk + PIP_3 \leftrightarrow PIP_3 - Itk - Itk - PIP_3$	1.25×10^{-4}	0.05	400	
$Itk - Itk + IP_4 \leftrightarrow Itk - Itk - IP_4$	1.25×10^{-3}	0.05	40	
$PIP_3 - Itk - Itk + IP_4 \leftrightarrow PIP_3 - Itk - Itk - IP_4$	1.25×10^{-3}	0.05	40	

$IP_4 - Itk - Itk + PIP_3 \leftrightarrow IP_4 - Itk - Itk - PIP_3$	1.25×10^{-4}	0.05	400	
$IP_4 - Itk - Itk + IP_4 \leftrightarrow IP_4 - Itk - Itk - IP_4$	1.25×10^{-3}	0.05	40	
$Itk - Itk - PIP_3 + S \leftrightarrow IP_4 + Itk - Itk - PIP_3$				1.5×10^{-4}
$IP_4 - Itk - Itk - PIP_3 + S \leftrightarrow IP_4 + IP_4 - Itk - Itk - PIP_3$				1.5×10^{-4}
$PIP_3 - Itk - Itk - PIP_3 + S \leftrightarrow IP_4 + PIP_3 - Itk - Itk - PIP_3$				1.5×10^{-4}

All the low affinity binding of Itk PH domains with PIP_3 and IP_4 , and, the IP_4 production rate are taken to be the same as that shown for model M1 (Table S1).

The ODEs are same as model 1 but the rate constants are different.

ODEs for Model 6: The reactions for Model 6 are given in the table below. The corresponding ODEs are shown below the table.

Table S6: Reactions and rate constants for model M6.

Reactions	k_{on} ($\mu M^{-1} s^{-1}$)	k_{off} (s^{-1})	K_D (μM)	k_{cat} ($\mu M^{-1} s^{-1}$)
$Itk + PIP_3 \leftrightarrow Itk - PIP_3$	1.25×10^{-4}	0.05	400	
$Itk + IP_4 \longleftrightarrow Itk - IP_4$	1.25×10^{-3}	0.05	40	
$Itk - PIP_3 + S \rightarrow IP_4 + Itk - PIP_3$				1.5×10^{-4}

All the low affinity binding of Itk PH domains with PIP_3 and IP_4 , and, the IP_4 production rate are taken to be the same as that shown for model M1 (Table S1).

$$\frac{dN_{Itk}}{dt} = k_{-1}N_{Itk-PIP_3} - k_1N_{Itk}N_{PIP_3} + k_{-2}N_{Itk-IP_4} - k_2N_{Itk}N_{IP_4}$$

$$\frac{dN_{Itk-PIP_3}}{dt} = k_1N_{Itk}N_{PIP_3} - k_{-1}N_{Itk-PIP_3}$$

$$\frac{dN_{Itk-IP_4}}{dt} = k_2N_{Itk}N_{IP_4} - k_{-2}N_{Itk-IP_4}$$

$$\frac{dN_{PIP_3}}{dt} = k_{-1}N_{Itk-PIP_3} - k_1N_{Itk}N_{PIP_3}$$

$$\frac{dN_{IP_4}}{dt} = k_{-2}N_{Itk-IP_4} - k_2N_{Itk}N_{IP_4} + k_4N_{Itk-PIP_3}N_S$$

$$\frac{dN_S}{dt} = -k_4N_{Itk-PIP_3}N_S$$

The conservation laws are

$$N_{Itk} + N_{Itk-PIP_3} + N_{Itk-IP_4} = N_{Itk}(t=0)$$

$$N_{PIP_3} + N_{Itk-PIP_3} = N_{PIP_3}(t=0)$$

$$N_{IP_4} + N_{Itk-IP_4} + N_S = N_S(t=0)$$

ODEs for Model 7: The reactions for Model 7 are given in the table below. The corresponding ODEs are shown below the table.

Table S7: Reactions and rate constants for model M7.

Reactions	k_{on} ($\mu\text{M}^{-1}\text{s}^{-1}$)	k_{off} (s^{-1})	K_D (μM)	k_{cat} ($\mu\text{M}^{-1}\text{s}^{-1}$)
$Itk - Itk + PIP_3 \leftrightarrow Itk - Itk - PIP_3$	2.5×10^{-4}	0.01	40	
$PIP_3 - Itk - Itk + PIP_3 \leftrightarrow PIP_3 - Itk - Itk - PIP_3$	0.01	0.1	10	
$Itk - Itk + IP_4 \leftrightarrow Itk - Itk - IP_4$	2.5×10^{-3}	0.01	4	
$PIP_3 - Itk - Itk + IP_4 \leftrightarrow PIP_3 - Itk - Itk - IP_4$	2.5×10^{-3}	0.01	4	
$IP_4 - Itk - Itk + PIP_3 \leftrightarrow IP_4 - Itk - Itk - PIP_3$	0.01	0.1	10	
$IP_4 - Itk - Itk + IP_4 \leftrightarrow IP_4 - Itk - Itk - IP_4$	0.1	0.1	1	
$Itk - Itk - PIP_3 + S \leftrightarrow IP_4 + Itk - Itk - PIP_3$				1.5×10^{-4}
$IP_4 - Itk - Itk - PIP_3 + S \leftrightarrow IP_4 + IP_4 - Itk - Itk - PIP_3$				1.5×10^{-4}
$PIP_3 - Itk - Itk - PIP_3 + S \rightarrow IP_4 + PIP_3 - Itk - Itk - PIP_3$				1.5×10^{-4}

All the high and low affinity binding of Itk PH domains with PIP_3 and IP_4 , and, the IP_4 production rate are estimated to match the PLCg1 kinetics in Ref. (3).

The ODEs are same as model 1 but the rate constants (shown above) are different.

Description of the models:

Models M1-M4 and M7 contain IP_4 mediated feedbacks. Models M5-M6 lack those feedbacks. Models M4 and M6 contain monomeric Itk molecules. Models M1-M3, M5 and M7 contain dimeric Itk molecules. In model M1 (Fig. S1B), PIP_3 binding to one of the PH domains increases the affinity of the other PH domain for both IP_4 and PIP_3 . M2, M3 and M7 (Fig. S1B) are variants of this model where PIP_3 binding to one PH domain in a dimer does not change the affinity of the other PH domain for either IP_4 or PIP_3 (M2), or allosterically increases the affinity of the other PH domain for IP_4 but *not* PIP_3 (M3), or allosterically increases the affinity of the other PH domain for PIP_3 but *not* IP_4 (M7). These models probed potential secondary interactions between Itk dimers and the membrane lipids. In the monomeric model, M4 (Fig. S1B), IP_4 binds the single Itk PH domain with a weak affinity and induces a conformational change (denoted by Itk* in table S4) that increases the affinity of this PH domain for both PIP_3 and IP_4 . In the models lacking IP_4 mediated positive feedbacks, the PH domains of dimeric (model M5) or monomeric (model M6) Itk molecules bind both PIP_3 and IP_4 without an allosteric

modification of the binding affinities. The models are summarized in Table I in the main text. We describe the reactions used for each of the models in the tables S1-S7. In all models we make the following assumptions to make the models simpler while preserving important general features.

Assumptions (M1-M7).

1. The initial concentration of the molecular species LAT bound Itk, is referred to as Itk^0 , and, has been used as a surrogate of signal strength given by antigen dose or antigens of different affinities. The stronger the stimulation, the larger is the value of Itk^0 .
2. The details of signal dependent recruitment of PI3K and consequent production of PIP_3 by PI3K have not been considered. PIP_3 is produced within seconds after stimulation (4-6). Hence, we started our simulations with an initial concentration of PIP_3 , referred to as PIP_3^0 from now on. For a given strength of stimulation (i.e. binding of a peptide of a particular affinity), the concentration of total PIP_3 (bound plus unbound) has been held fixed to the initial PIP_3 concentration for the entirety of the simulation. The number of PIP_3^0 is decreased as the peptide affinities are decreased in order to mimic decreasing PI3K-mediated PIP_3 production with decreasing intensity of TCR engagement. For example, we have used $\text{PIP}_3^0 = 530$ molecules for OVA stimulation but only 50 molecules of PIP_3^0 for G4 stimulation.
3. As $\text{PLC}\gamma 1$ is the immediate downstream effector of PIP_3 bound Itk, we have assumed that the kinetics of the concentration of PIP_3 bound Itk directly represents $\text{PLC}\gamma 1$ activation kinetics.
4. A 5-phosphatase, responsible for the turnover of IP_4 , is absent in our models. Following TCR ligation, the experimentally determined IP_4 level in thymocytes/T cells increases until it reaches its peak at around 10 mins (7). Then owing to the 5-phosphatase activity, IP_4 levels decrease, decaying to half of its peak value at around 30 mins (7). Activation of $\text{PLC}\gamma 1$ on the other hand is much faster, peaking at around 1 to 2 mins (main text, (3)). Based on these data, we believe that the role of 5-phosphatase, if any, in the activation of $\text{PLC}\gamma 1$, is insignificant.

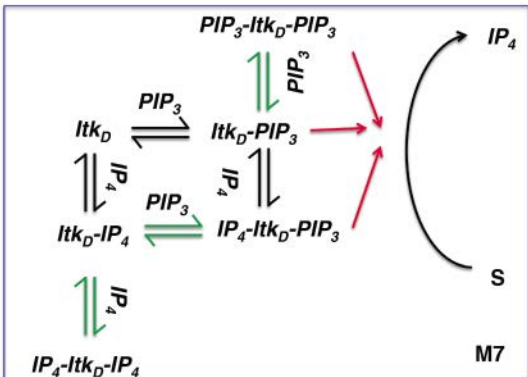
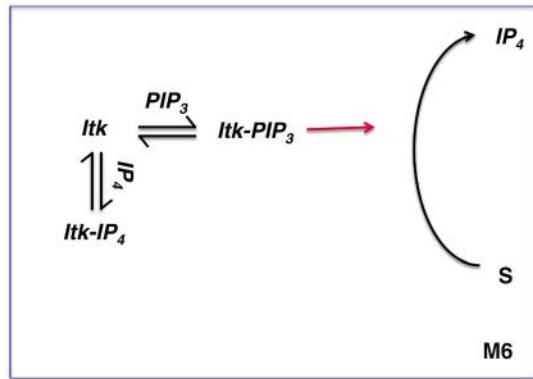
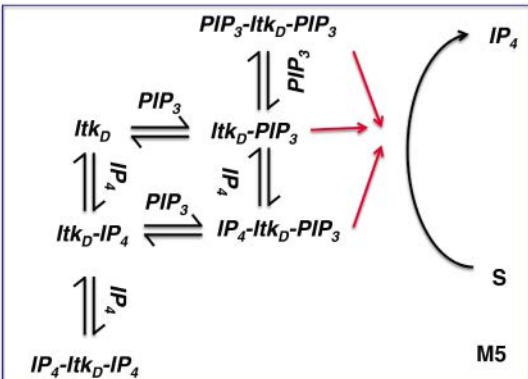
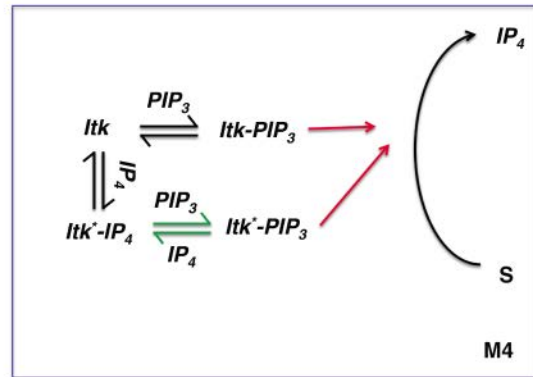
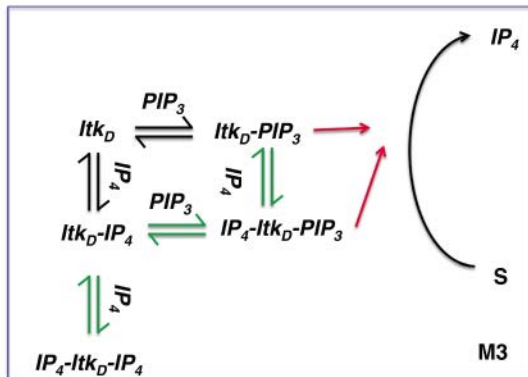
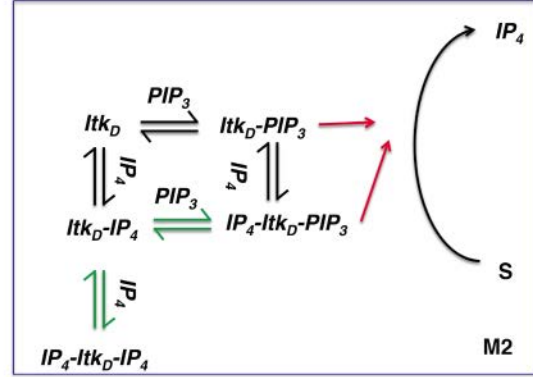
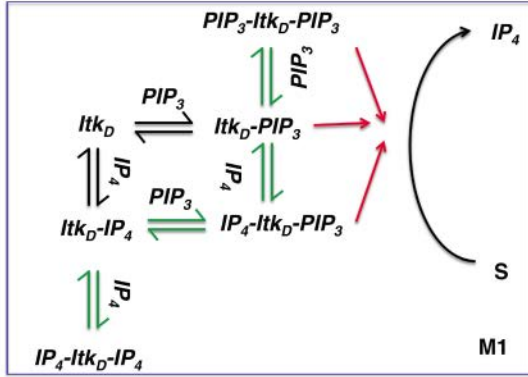


Fig. S1B: Graphical networks describing the signaling reactions in models M1-M7.

I_{tk} shown in this figure represents an I_{tk} molecule that is bound to the TCR and LAT signalosome (not shown). High affinity binding reactions are shown as green arrows. PIP₂ hydrolysis into DAG and IP₃ which ultimately produces IP₄ (S) is shown as red arrows. **(M1)** In model M1, both IP₄ and PIP₃ can equally induce allosteric modifications of the PH domains in I_{tk} dimers. **(M2)** Model M2. Similar to M1, however, modification of the PH domains by PIP₃ cannot stabilize IP₄ or PIP₃ binding to the I_{tk} PH domains. **(M3)** Model M3. Similar to M1, however, modification of the PH domains by PIP₃ can only stabilize IP₄ but not PIP₃ binding to the I_{tk} PH domains. **(M4)** Model M4. The I_{tk} PH domains are monomeric and unable to interact allosterically. IP₄ or PIP₃, upon binding with a weak affinity, instantaneously changes I_{tk} to a high affinity conformation (I_{tk}^{*}) where IP₄ (or PIP₃) can replace PH domain bound PIP₃ (or IP₄) with high affinity. **(M5)** Model M5. Both IP₄ and PIP₃ bind to the PH domains of the I_{tk} dimer with low affinity. No allosteric modification occurs. **(M6)** Model M6. Similar to model M5 but I_{tk} exists only in monomers. **(M7)** Model M7. Similar to M1, however, modification of the PH domains by PIP₃ can only stabilize PIP₃ but not IP₄ binding to the I_{tk} PH domains.

Table S8: Values of the concentrations of different molecular species used in the models.

Molecules	Number	Comments
PIP ₃ ⁰	Varied from 50-530	Roughly 5% of the available PIP ₂ pool (8) is taken to be the upper limit of PIP ₃ concentration. In a separate measurement, the PIP ₃ concentration reaches to about 150-200 μM in neutrophils, 10 seconds after stimulation (6).
I _{tk} -I _{tk} ⁰ (for dimers)/ I _{tk} ⁰ (for monomers)	Varied from 20-300	The upper limit of I _{tk} is assumed to be the upper limit of phosphorylated LAT in thymocytes (9).
S ⁰	17000	3.5 mM, 10 seconds after stimulation in neutrophils (6).
IP ₄	We do not have any basal level of IP ₄ in the models. IP ₄ is generated via the	The IP ₄ level in Jurkat T-lymphocytes increased to 1125 ± 125 pmol/10 ⁹

	cleavage of PIP ₂ (S).	cells after stimulation by anti-CD3 antibody OKT3 (7). This number, when converted to molecules/cell, is roughly two times the number we have used as an upper limit for IP ₄ (i.e. the initial PIP ₂ concentration) in our simulations.
--	-----------------------------------	--

Unit Conversion Table

$$1\mu\text{M} = 600 \text{ molecules}/(\mu\text{m})^3$$

$$k_{\text{on}}^{3\text{D}} = 1 (\mu\text{M}^{-1}\text{s}^{-1}) = 0.16 \times 10^{-2} (\mu\text{m})^3 / (\text{molecules}) \text{ s}^{-1}$$

Note that the reactions involving two plasma membrane bound complexes take place only at the plasma membrane. Hence we have to convert our $k_{\text{on}}^{3\text{D}}$ to the corresponding $k_{\text{on}}^{2\text{D}}$ in order to describe a binding reaction on a plane. This is done by dividing the $k_{\text{on}}^{3\text{D}}$ by the lengths $l = 2 \text{ nm}$ (Fig. S1A).

Effects of intrinsic noise fluctuations

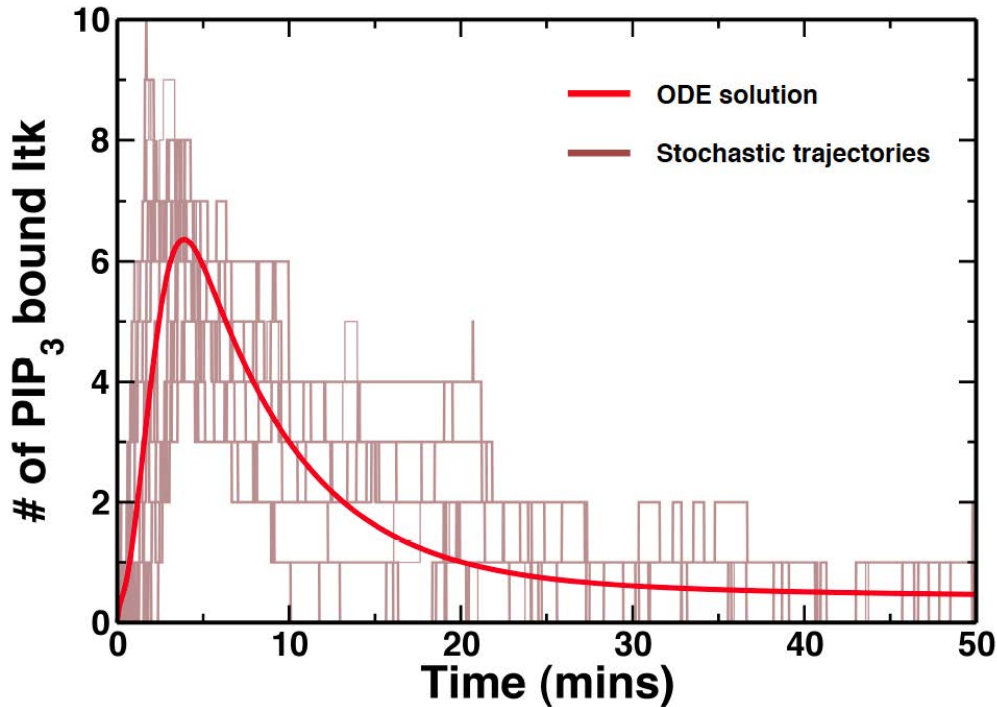


Fig. S2: Presence of Intrinsic fluctuations does not lead to qualitatively different temporal profiles as compared with the deterministic model. We show 11 different stochastic trajectories for $Itk^0 = 20$ molecules and $PIP_3^0 = 50$ molecules, the lowest concentration used in our simulations, for model M3. The stochastic trajectories for concentrations of PIP_3 bound Itk were obtained by solving the Master equation associated with the signaling reactions (Table S3) using the Gillespie algorithm (10). The curve in red is the solution of the mass action kinetics given by a set of ODEs. We use the same kinetic rates and initial concentrations for the stochastic simulations and the ODEs. The above figure shows that the stochastic trajectories spread around the solution of the ODEs (shown in red). In the next figure (Fig. S3) we show how the ODE solution compares with stochastic trajectories when averaged over a small number of *in silico* “cells”. The smaller the difference between the two, the more accurate the ODEs are in describing the kinetics for the cell population, even in the presence of intrinsic stochastic fluctuations.

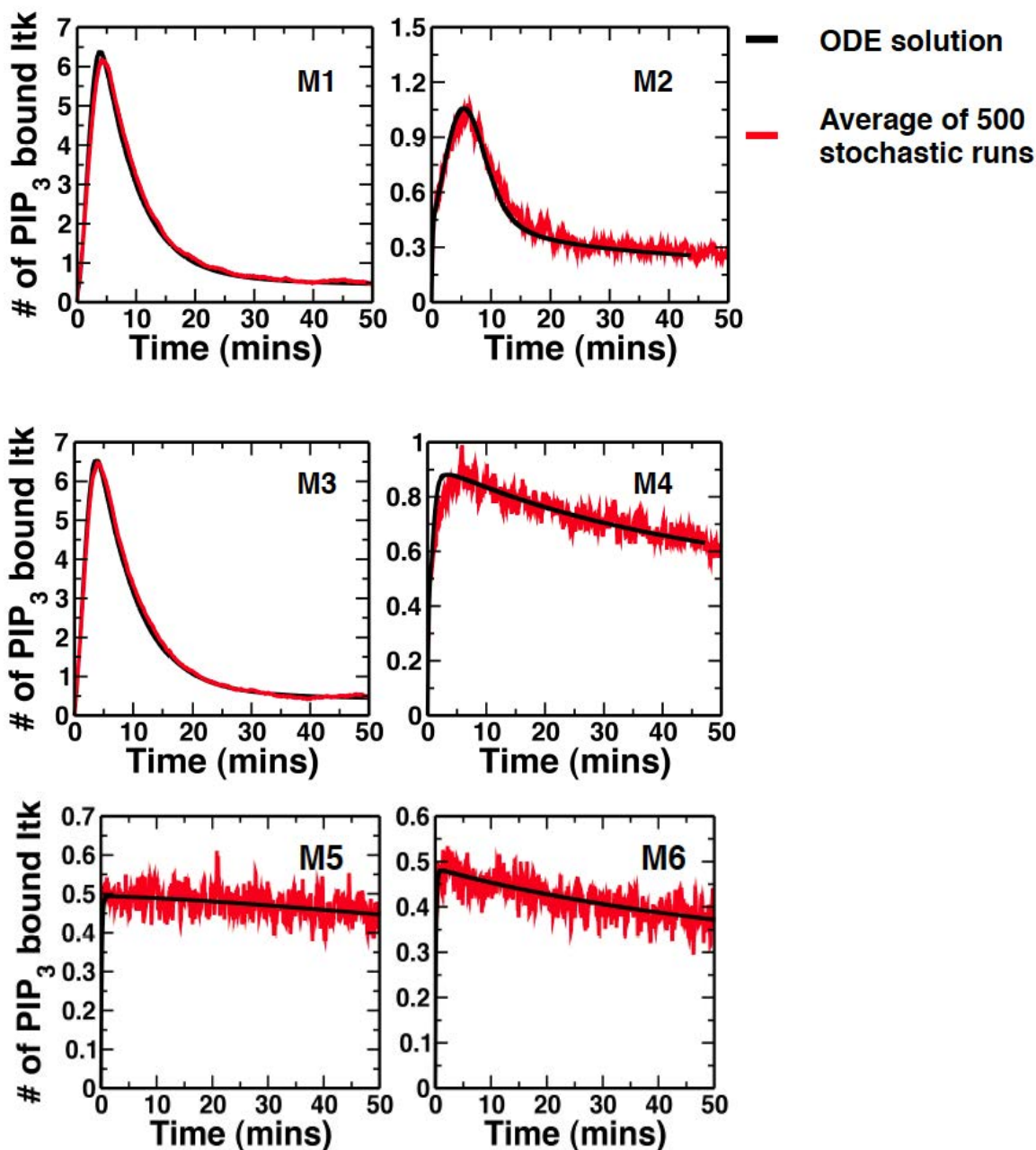


Fig. S3: Comparison between the ODE solutions and the stochastic trajectories averaged over a small number of cells. We compared the temporal profiles of concentrations of PIP₃ bound Itk obtained in simulations including stochastic copy number variations due to intrinsic noise fluctuations (red) with the solutions of the deterministic mass action reaction kinetics that ignored such fluctuations (solid black lines). The stochastic simulations were carried out by using Gillespie's method (10) which provided exact numerical solution of the Master equations associated with the models. We used the same rate constants and initial concentrations for the stochastic simulations and ODE solutions. The kinetic trajectories were averaged over 500

realizations (or *in silico* “cells”) for the stochastic simulations. We show the results for the smallest concentrations of Itk^0 (20 molecules) and PIP_3^0 (50 molecules) where the effect of the stochastic fluctuations is expected to be the largest. We observed that for all the models the ODE solutions produce qualitatively similar shapes as the average stochastic trajectories. Model M7 is not shown.

Variation of the peak value (A) as the initial concentrations of Itk and PIP_3 were increased in models M1 to M7.

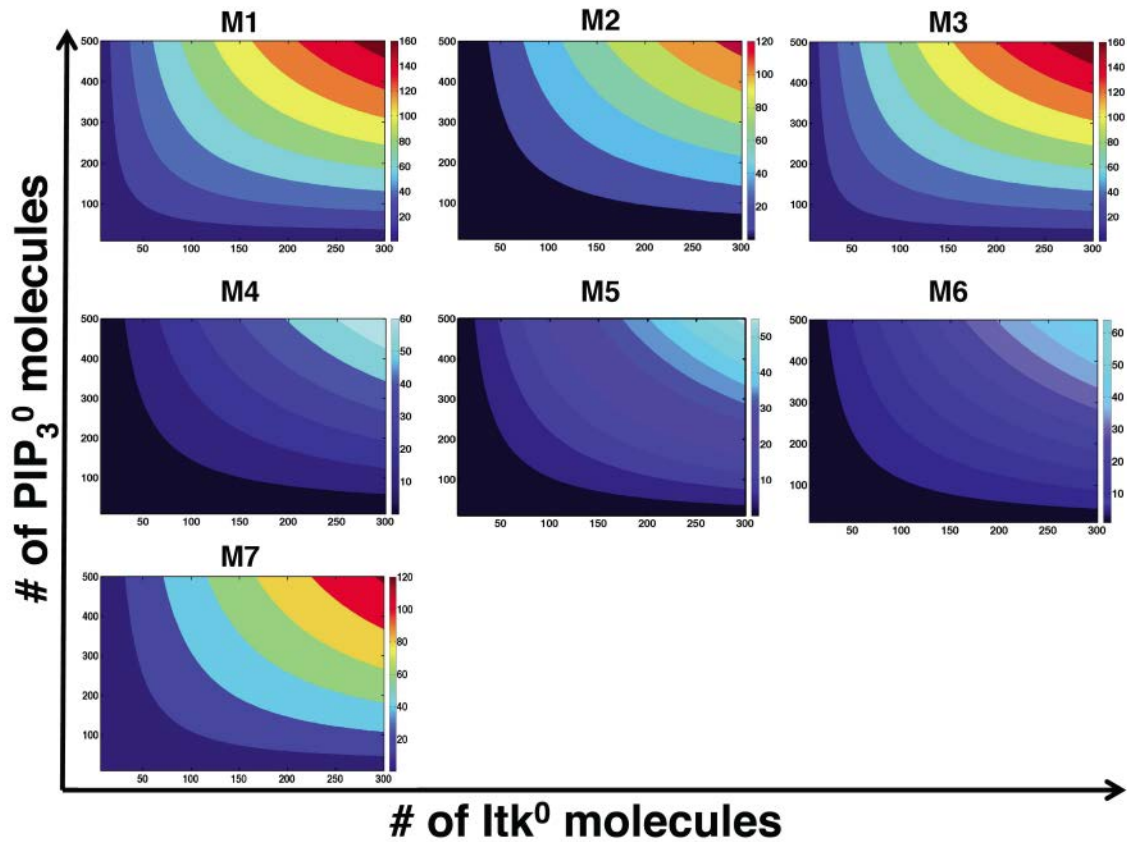


Fig. S4: Variation of the peak value (A) with Itk^0 and PIP_3^0 for all seven models. The peak value of PIP_3 bound Itk increased in a graded manner with increasing initial Itk and PIP_3 concentrations.

The variation of peak time (τ_p) as initial concentrations of Itk and PIP_3 were increased in models M1 to M7.

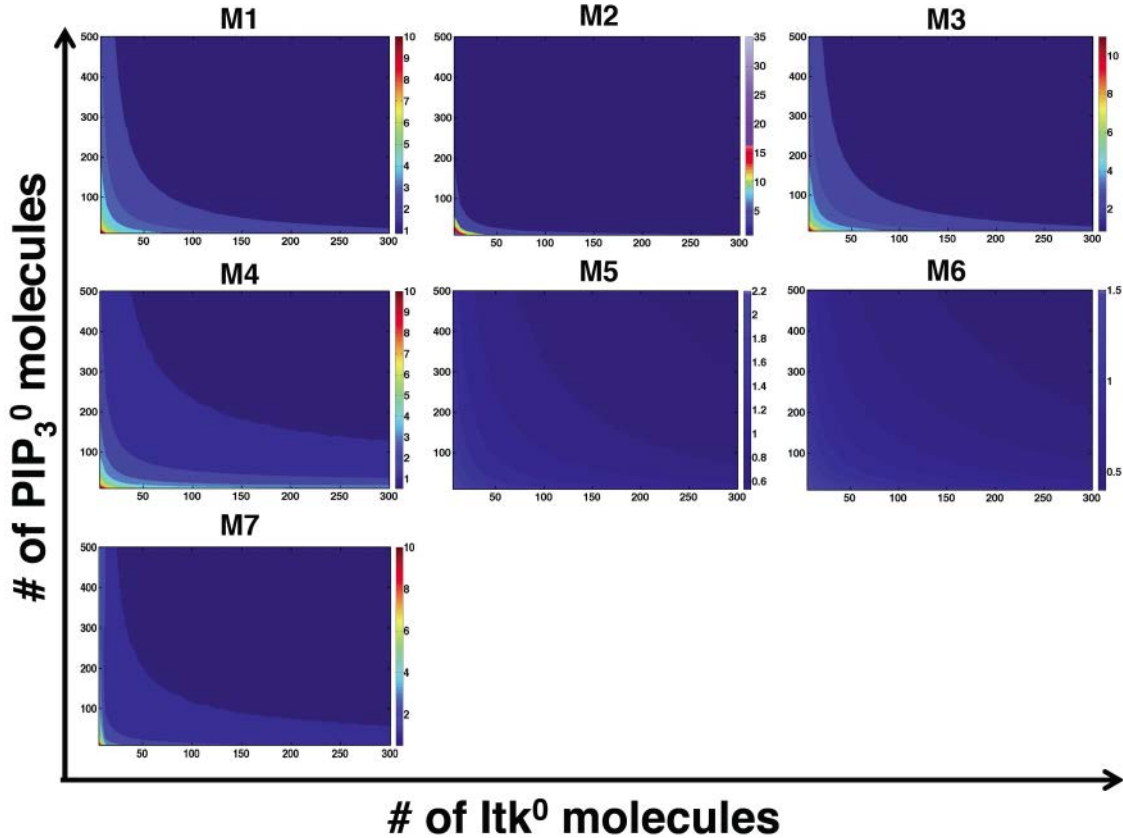


Fig. S5: Variation of τ_p with Itk^0 and PIP_3^0 for all six models. The peak time (τ_p) of the temporal profile of the concentration of PIP_3 bound Itk varied by an order of magnitude (roughly from 1 min to 10 mins) in models M1-M4 and M7, while the peak time did not change appreciably in models M5 and M6 over the entire range of variation. However, τ_p did not vary appreciably over a large range of initial Itk (>100) and PIP_3 concentrations (>150) even in the models M1-M4 and M7. Most of the large variations occurred at small concentrations of Itk and PIP_3 . We analyzed the above behavior using simple models as described in the following section.

Understanding mechanisms that regulate the shape of the temporal profiles of PIP_3 bound Itk

We constructed simpler models that effectively describe M1-M4 to analyze the effect of the feedbacks and the binding-unbinding reactions in controlling the shape of the kinetics of PIP_3 bound Itk. The simpler models could be analytically tractable under certain conditions which allowed us to characterize the dependence of kinetics on the reaction

rates and concentrations. Such calculations are usually very useful in glean- ing mechanistic understanding into the system.

Effect of the positive feedback: We aimed to understand how the positive feedback controls τ_p as the initial concentrations of Itk (Itk^0) and PIP_3 (PIP_3^0) were varied. In models M1-M4, multiple reactions occurring at different time scales work in concert to create the positive feedback which in essence increases the binding affinity of Itk PH domains for PIP_3 . Therefore, in order to analyze the initial concentration dependence of the peak time, τ_p , we constructed an effective binding unbinding reaction between Itk and PIP_3 , where, the reaction rates (k_l and k_{-l}) are initial concentration dependent.



The concentration dependence in the above reaction rates can arise because the effective reaction captures the kinetics of binding of Itk to PIP_3 in models M1-M4, where multiple second order reactions associated with different time scales induce positive feedback interactions between Itk and PIP_3 . In order to compare reaction 1 with the effect of only the positive feedback, we removed the negative feedback interactions from models M1-M4. Therefore, in all the models, the concentration of Itk bound PIP_3 reached a non-zero concentration at the steady state (Fig. S6A, black curve). Then we estimated the effective rates, k_l and k_{-l} that will produce similar kinetics (same $\tau_{1/2}$ and the same steady state) (Fig. S6B, blue curve) following the scheme below. The kinetics of $x = Itk - PIP_3$ in Reaction 1 is given by,

$$\frac{dx}{dt} = k_l(Itk^0 - x)(PIP_3^0 - x) - k_{-l}x = k_l \left[(Itk^0 - x)(PIP_3^0 - x) - K_D x \right] \quad (1)$$

where, Itk^0 and PIP_3^0 denote the initial concentrations of Itk and PIP_3 , respectively, and, $K_D = k_{-l}/k_l$. The solution of the above equation is,

$$x(t) = \frac{x_s^+ x_s^- \left(1 - e^{k_l(x_s^+ - x_s^-)t} \right)}{x_s^- - x_s^+ e^{k_l(x_s^+ - x_s^-)t}} \quad (2)$$

x_s^+ and x_s^- being the two steady state (one stable another unstable) solutions given by

$$x_s^\pm = \frac{Itk^0 + PIP_3^0 + k_D \pm \sqrt{(Itk^0 + PIP_3^0 + K_D)^2 - 4Itk^0 PIP_3^0}}{2} \quad (3)$$

The time ($\tau_{1/2}$) taken by x , to reach the half of the steady state (the stable fixed point in Eq. (3)) concentration is given by,

$$\tau_{1/2} = \frac{1}{k_1(x_s^+ - x_s^-)} \text{Log} \left(\frac{2x_s^+ - x^-}{x_s^+} \right) \quad (4)$$

For a particular set of initial concentrations, we calculated the steady state concentration of PIP₃ bound Itk, and, $\tau_{1/2}$, by numerically solving the corresponding ODEs for models M1-M4 with the negative feedbacks being turned off. Then using Eqns. (3) and (4), we estimated the rate constants, k_1 and K_D (or, equivalently, k_1 and k_{-1}) for each set of initial concentrations (Figs. S7 and S8). Both k_1 and K_D varied with initial concentrations of Itk and PIP₃. However, K_D did not change appreciably with concentrations for M1 and M3 as compared to M4 or M2 (Fig. S7). M1 and M3 showed qualitatively similar variations in K_D and k_1 with increasing initial concentrations. This demonstrates a large degree of similarity between the models. For models M1-M3, the values of K_D in the effective binding-unbinding reaction are substantially smaller (<100 times) to bare Itk and PIP₃ interaction ($K_D = 2000$) used in tables S1-S3, in the absence of any IP₄ feedback. This again demonstrates that the feedback reactions convert the low affinity interactions between Itk and PIP₃ to a high affinity binding unbinding reaction.

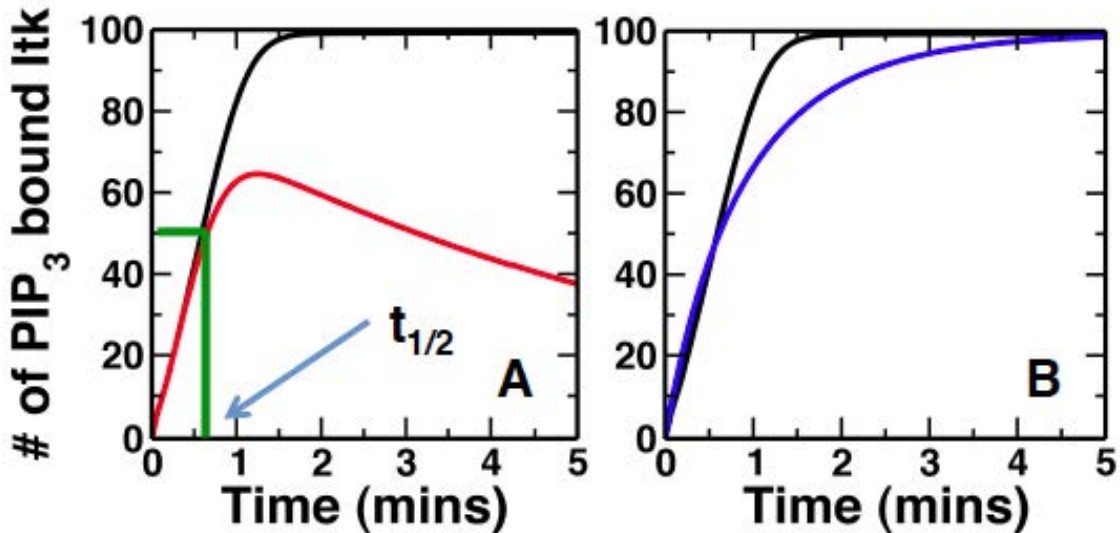


Fig. S6: Estimation of the reaction rates in the effective binding-unbinding reaction.
A) The transient kinetics of PIP₃ bound Itk in M1 (red) is compared with the case when the negative feedback is removed (black). We use $\tau_{1/2}$ and the steady state concentration of the kinetics of PIP₃ bound Itk in the absence of the negative feedback to calculate the rates in the effective binding-unbinding reaction 1. B) Kinetics of PIP₃ bound Itk in the absence of the negative feedback in model M1 (black). Blue, kinetics of PIP₃ bound Itk in the corresponding binding unbinding process (reaction 1) where the $\tau_{1/2}$ and the steady state concentration of PIP₃ bound Itk is exactly the same as the black curve.

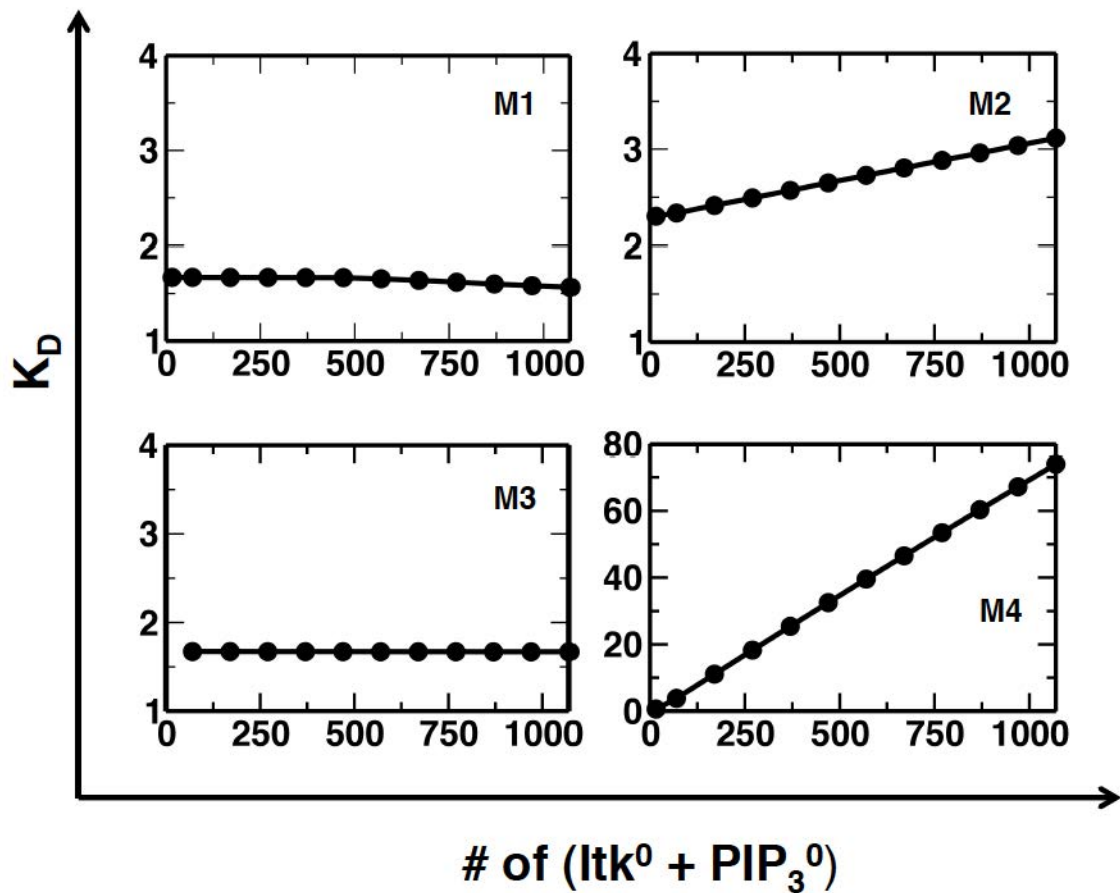


Fig. S7. Variation of K_D as a function of the sum of Itk^0 and PIP_3^0 for models M1 to M4. The K_D for the binding unbinding process has been estimated using the steady state values of the Itk kinetics in presence of the positive but not negative feedback. For models M1-M3, K_D does not change significantly with increasing concentrations of initial Itk and PIP_3 . The value of K_D is much smaller than the sum of $(Itk^0 + PIP_3^0)$ as well. For M4 however, K_D increases significantly (by an order of magnitude). The absolute value of the K_D is still a lot less than $(Itk^0 + PIP_3^0)$.

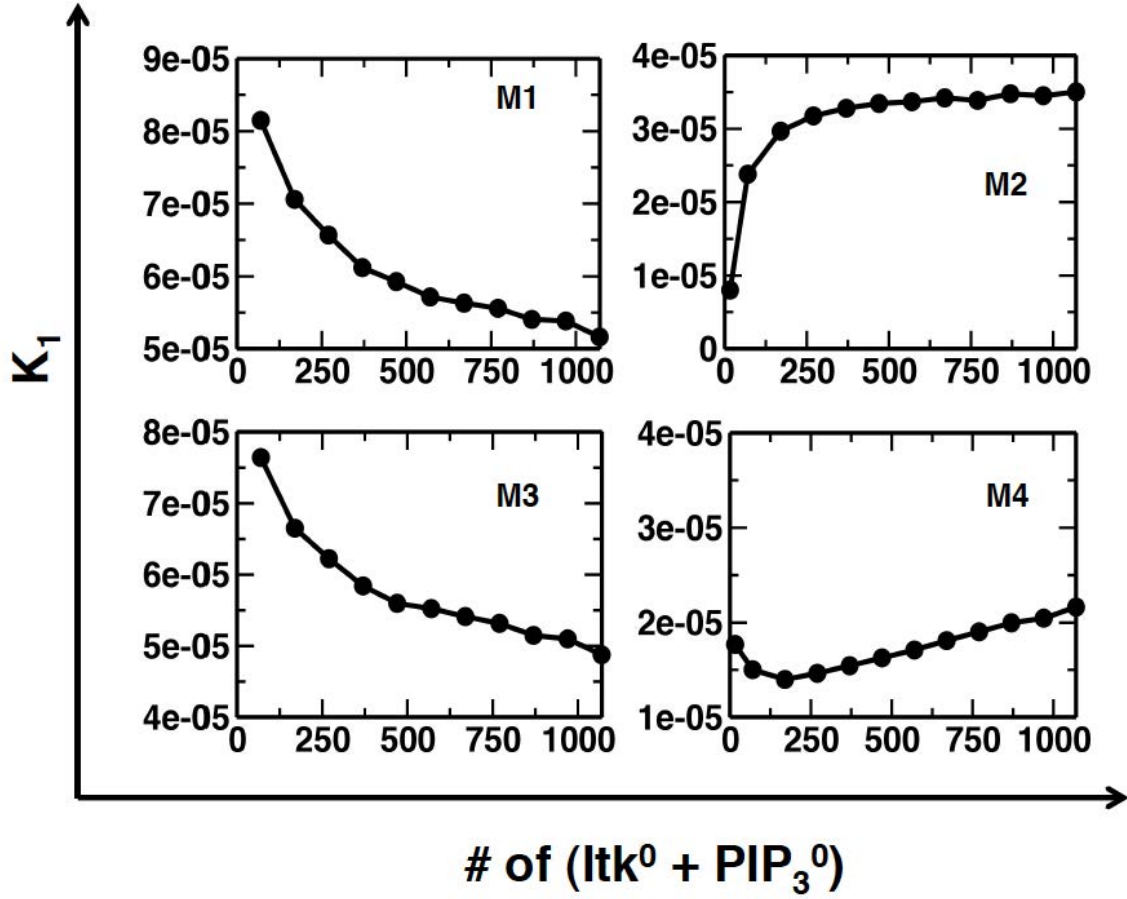


Fig. S8: Variation of k_1 as a function of the sum of Itk^0 and PIP_3^0 for models M1 to M4. k_1 decreased roughly 2 fold with the increase in Itk^0 and PIP_3^0 for M1 and M3, while, for model M2, k_1 increased 4 times. In M4, k_1 did not change appreciably.

Next we analyzed the concentration dependence of $\tau_{1/2}$ in the effective binding-unbinding reaction. This provided us with an estimate of concentration dependence of τ_p in model M1-M4, when the negative feedbacks do not contribute appreciably to τ_p . When, $K_D \ll Itk^0 + PIP_3^0$, as in Fig.S7, the Eqn (4) can be well approximated by,

$$\tau_{1/2} = \frac{1}{k_1(PIP_3^0 - Itk^0)} \log\left(\frac{2PIP_3^0 - Itk^0}{PIP_3^0}\right) \quad (5)$$

For the range of concentrations of Itk^0 and PIP_3^0 that we have considered in the simulation of our models,

$$\log\left(\frac{2PIP_3^0 - Itk^0}{PIP_3^0}\right) \sim \text{constant}, \text{ therefore,}$$

$$\tau_{1/2} \approx \frac{1}{k_1(PIP_3^0 - Itk^0)} \quad (6)$$

When k_I does not depend on concentrations, a tenfold increase in $PIP_3^0 - Itk^0$, will lead to a tenfold decrease in $\tau_{1/2}$. However, our calculations showed that the effective k_I also changes with Itk^0 and PIP_3^0 (Fig. S8). E.g., k_I decreased roughly two fold in models M1 and M3 (Fig. S8) as Itk^0 and PIP_3^0 were increased, implying that when $PIP_3^0 - Itk^0$ is increased ten times, the decrease in $\tau_{1/2}$ will be roughly 5 times instead of 10 times. For M2, however, owing to the four times increase in k_I , $\tau_{1/2}$ will decrease twenty fold for the same increase in $PIP_3^0 - Itk^0$. This is similar to what we observe in Fig S5 for the variation of τ_p with initial PIP_3 and Itk concentrations. For M1 and M3, the concentration dependence in k_I actually restricts the variation in $\tau_{1/2}$ (~5 times), while in M2 it helps in the variation in $\tau_{1/2}$ (~20 times).

For model M4, K_D showed a monotonic increase with increasing Itk^0 and PIP_3^0 (Fig. S7). However, values of K_D are much smaller than $(Itk^0 + PIP_3^0)$ for the range of concentrations we considered, therefore, we can still use Eq. (6) to estimate $\tau_{1/2}$. In contrast, for model M4, k_I did not vary appreciably with Itk^0 and PIP_3^0 , therefore, the variation in $\tau_{1/2}$ is largely determined by the change in with Itk^0 and PIP_3^0 as given by Eq. (6). This is reflected in the dependence of τ_p on initial Itk and PIP_3 concentrations.

Models (M5 and M6) lacking positive feedbacks:

For models M5 and M6, when the negative feedbacks are turned off, the effective binding unbinding reaction can represent the kinetics of $Itk - PIP_3$ with constant K_D and k_I for all concentrations. The estimated K_D values for the effective reaction were much larger ($K_D \sim 2000$) compared to the values of Itk^0 and PIP_3^0 we considered in the simulations, i.e, $K_D \gg (Itk^0 + PIP_3^0)$. Therefore, in this situation $\tau_{1/2}$ can be approximated by

$$\tau_{1/2} \approx \frac{1}{k_1 K_D} = \frac{1}{k_{-1}} \quad (7)$$

where, $\tau_{1/2}$, is solely determined by the unbinding rate and does not show any concentration dependence. This is in agreement with the results (Fig. S5) for models M5-M6.

Dependence of the decay time τ_d of PIP_3 bound Itk on the initial concentrations of Itk and PIP_3 due to the negative feedbacks

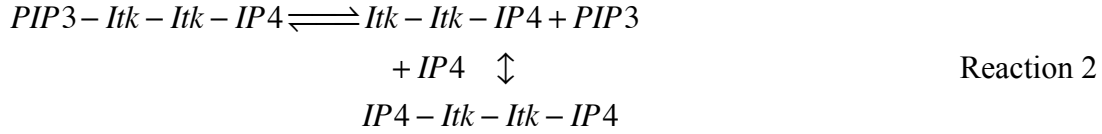
The decay time τ_d characterizes the time scale for the decay of the concentration of PIP_3 bound Itk from its peak value as IP_4 molecules outnumber PIP_3 molecules. We defined τ_d as the difference of the time (t_2) taken to decay to the half maximum value after the peak value is reached and the peak time, τ_p . The dependence of τ_d on the initial

concentrations of I_{tk} and PIP_3 manifests in the variations of the asymmetry ratio R with increasing I_{tk}^0 and PIP_3^0 as shown in Fig. 2 in the main text. We aim to characterize the concentration dependence of τ_d for the different models in this section.

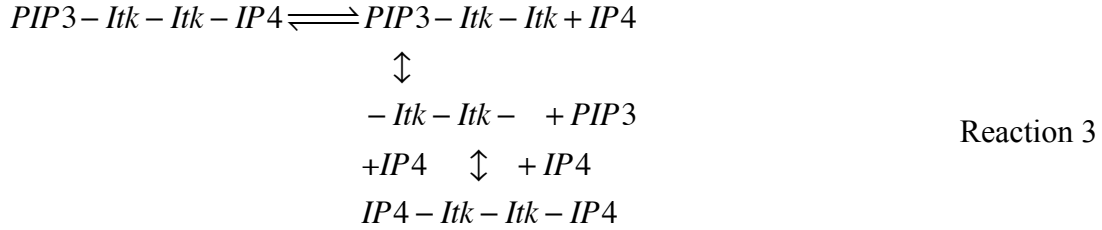
Feedback models (M1-M3) with I_{tk} dimers:

Owing to the strong positive feedback, most of the PIP_3 bound I_{tk} molecules exist in $PIP_3 - I_{tk} - I_{tk} - IP_4$ heterodimers. I_{tk} is sequestered into the cytosol via the reactions inducing negative feedbacks in the system as a result of formation of the soluble complex $IP_4 - I_{tk} - I_{tk} - IP_4$. This complex is produced by reactions occurring via two channels:

Channel I



Channel II



When the concentration of IP_4 is much larger than that of PIP_3^0 , formation of the soluble $IP_4 - I_{tk} - I_{tk} - IP_4$ is more likely to occur through channel I, because, in channel II when IP_4 unbinds from $PIP_3 - I_{tk} - I_{tk} - IP_4$, the complex, $I_{tk} - I_{tk} - PIP_3$ is quickly transformed back to $PIP_3 - I_{tk} - I_{tk} - IP_4$, due to the presence of large number of IP_4 molecules. The rate of change of $x = IP_4 - I_{tk} - I_{tk} - PIP_3$ can be described by

$$\frac{dx}{dt} = (\tilde{k}_1 \cdot [IP_4] \cdot [I_{tk} - I_{tk} - PIP_3] - \tilde{k}_{-1} x) + (\tilde{k}_1 \cdot [I_{tk} - I_{tk} - IP_4] \cdot [PIP_3] - \tilde{k}_{-1} x) \quad (8)$$

, where, \tilde{k}_1 and \tilde{k}_{-1} are high affinity binding unbinding rates of IP_4 and PIP_3 to the I_{tk} PH domains. The terms in the first and the second parentheses in the right hand side describe the binding unbinding reactions in channel I and II, respectively. We have considered the rates to be the same for IP_4 and PIP_3 , therefore, the above reaction is more appropriate for models M1 and M3. However, the general conclusions drawn in this calculation will apply for M2 as well. As argued above, when concentration of IP_4 is much larger than that of PIP_3 , the first set of binding unbinding reactions in channel II occur at faster time scales, and $\tilde{k}_1 \cdot [IP_4] \cdot [I_{tk} - I_{tk} - PIP_3] \approx \tilde{k}_{-1} x$. In addition, a large number of IP_4 molecules quickly convert the unstable $- I_{tk} - I_{tk} - IP_4$ complexes into stable complexes (reactions in channel I). Therefore, we can write down the following inequality,

$$\tilde{k}_1 \cdot [I_{tk} - I_{tk} - IP_4] [PIP_3] \ll \tilde{k}_1 \cdot [IP_4] \cdot [I_{tk} - I_{tk} - PIP_3] \approx \tilde{k}_{-1} x. \text{ Keeping in mind } \tilde{k}_1 \cdot [I_{tk} - I_{tk} - IP_4] [PIP_3] \ll \tilde{k}_1 \cdot [I_{tk} - I_{tk} - IP_4] [IP_4], \text{ } x \text{ in Eq. (8) can be approximated as,}$$

$$\frac{dx}{dt} = -\tilde{k}_{-1}x \quad (9)$$

Therefore, in this situation, the decay time does not appreciably depend on the initial concentrations of Itk and PIP₃, and is determined by the unbinding rate of PIP₃ from the PIP₃ – Itk – Itk – IP₄ complex (Fig. S9).

The above results change for M2, as IP₄ binding does not stabilize binding of PIP₃ to the Itk dimers. Therefore, the reactions in channel II play a greater role in the decay of x , and consequently, the decay time scales in M2 vary appreciably with the initial concentrations of Itk and PIP₃ (Fig. S9).

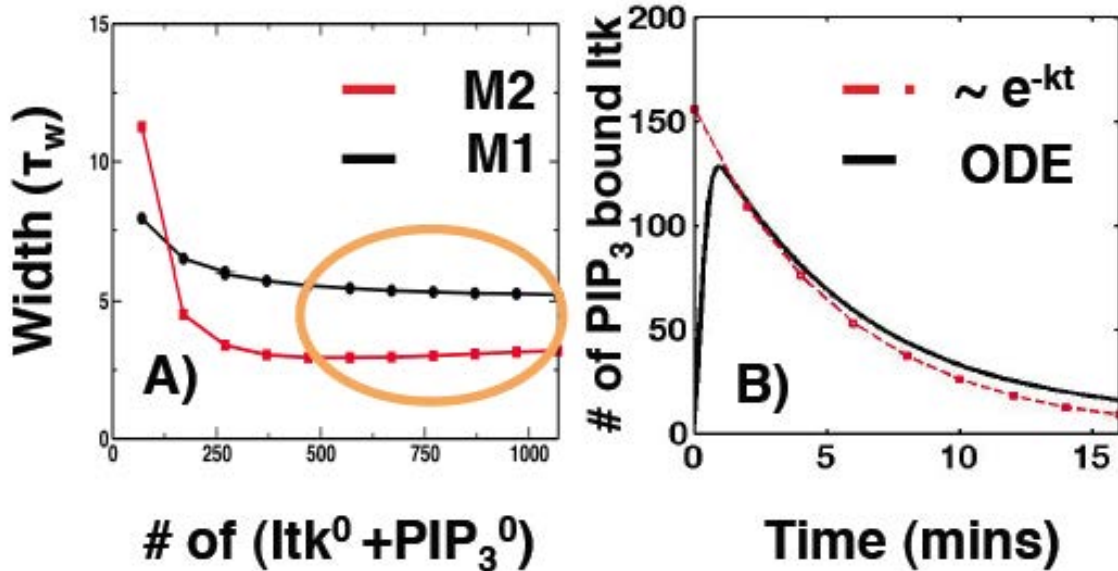


Fig. S9: The saturation of the width in the feedback models. A) We have varied both Itk⁰ and PIP₃⁰ such that $PIP_3^0 \geq Itk^0$. The plot of the width of PIP₃ bound Itk as a function of $(Itk^0 + PIP_3^0)$ is shown for M1 (black line) and M2 (red line). For large values of $(Itk^0 + PIP_3^0)$ the width saturates (the orange oval) both for M1 and M2. For M2 however the rate of decay of the width of Itk – PIP₃ kinetics is much faster than for M1 as can be seen from the fact that the red curve decays from roughly 12 mins to 3 mins where as the black curve goes down from 7 mins to 5 mins. B) The transient activation kinetics of the membrane bound Itk in M3 are shown in black. PIP₃⁰ = 500, Itk⁰ = 200. The dotted red curve is the exponential decay curve of the form e^{-kt} with the time constant equal to the inverse of the high affinity PIP₃ unbinding rate, which validates the claim of Eqn (9). The same holds true for M1. The saturation of width (τ_w) of the kinetics of PIP₃ bound Itk

concentration would be useful to understand the dependence of the ratio $R = \tau_w/\tau_p$ on initial concentrations of Itk and PIP₃.

Models lacking feedbacks (M5-M6):

Since both IP₄ and PIP₃ bind to Itk PH domains with a low affinity in M5 and M6, a large excess of IP₄ is required to sequester Itk into the cytosol. We quantify the amount of IP₄ that is required to effectively sequester Itk into the cytosol below.

Let us consider model M6. The rates of change of $x = Itk - PIP_3$ and $y = Itk - IP_4$ are given by

$$\begin{aligned}\frac{dx}{dt} &= k_1[Itk^0 - x - y].[PIP_3^0 - x] - k_{-1}x \\ \frac{dy}{dt} &= k_1[Itk^0 - x - y].[IP_4] - k_{-1}y\end{aligned}\quad (10)$$

, where, Itk^0 and PIP_3^0 denote the initial concentrations of Itk and PIP₃, respectively. Using, $IP_4 + y_s = S^0$, where, S^0 denotes the initial concentration of PIP₂, we find that at the steady state,

$$\frac{[PIP_3^0 - x_s]}{[S^0 - y_s]} = \frac{x_s}{y_s} \quad \Rightarrow \quad \frac{x_s}{y_s} = \frac{PIP_3^0}{S^0}\quad (11)$$

x_s can be calculated from the above equations,

$$x_s = \frac{Itk^0 + PIP_3^0 + k_D + S^0 - \sqrt{(Itk^0 + PIP_3^0 + k_D + S^0)^2 - 4 \cdot \left(\frac{S^0}{PIP_3^0} + 1\right) Itk^0 \cdot PIP_3^0}}{2 \cdot \left(\frac{S^0}{PIP_3^0} + 1\right)}\quad (12)$$

In order to get a finite τ_w , the kinetic of Itk-PIP₃ has to decay to half of its peak value (A) i.e., $x_s(S^0) < A/2$, for a given K_D , PIP_3^0 and Itk^0 . It is however hard to analytically write down a closed form of A. Instead, we can use $x_s(S^0=0)$ as an approximate upper bound of A (A_{max}). The reason being, for $S^0=0$ i.e., when PIP₂ concentration is zero, we recover the steady state for the binding unbinding process in absence of any competition from IP₄. This will represent the largest value A can ever attain. We used this as our approximation for the peak value (A) of PIP₃ recruited Itk in M6. The variation of x_s as a function of S^0 for two separate K_D is shown below.

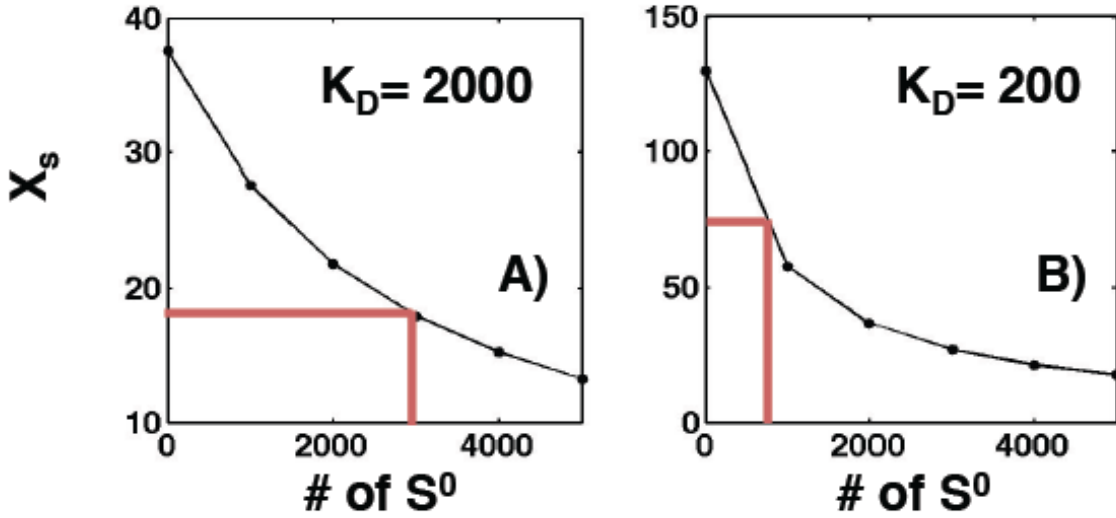


Fig. S10: A large concentration of IP₄ is required to replace PIP₃ in models M5-M6. A) Variation of the steady state x_s (Itk-PIP₃) as a function of initial substrate (PIP₂) concentration S^0 when the $K_D = 2000$. B) Variation of the steady state x_s as a function of initial substrate concentration S^0 when the $K_D = 200$.

In Fig S10, the values of x_s at $S_0=0$ denote the values for A_{\max} . Fig. S10A shows that for high K_D values the system requires a large concentration of S^0 (roughly 3000 molecules) to reach a steady state just about the half of A_{\max} . Moreover, when K_D is high, A_{\max} is small (Fig. S10A to Fig. S10B), which in turn slows down the production rate of IP₄. We can estimate the initial concentration dependence of this time scale as follows. The fastest time scale for IP₄ production is given by $(k_{cat}A_{\max})^{-1}$, where, k_{cat} is the rate at which PIP₂ is converted into IP₄ by Itk – PIP₃ by a one step reaction (tables S1-S6). Since, A_{\max} grows in a graded fashion with the increase in Itk⁰ and PIP₃⁰ (Eqn 12), the production timescales for IP₄ generation decrease slowly with increasing Itk⁰ and PIP₃⁰. Both these facts play hand in hand to give rise to a larger τ_d in M5 and M6 as compared to models M1-M3.

Model M4:

In model M4, in addition to the low affinity binding unbinding reactions, there is a bi-directional high affinity augmentation process. Following the same procedure as described above we compute the steady state concentration of PIP₃ bound Itk for M4. Denoting concentrations of Itk – PIP₃, Itk* – PIP₃ and Itk-IP₄ by x_1 , x_2 and y , respectively, the rate equations are given by,

$$\frac{dx_1}{dt} = k_1[Itk^0 - x - y][PIP_3^0 - x] - k_{-1}x_1$$

$$\frac{dx_2}{dt} = k_2[PIP_3^0 - x]y - k_2x_2[IP_4]$$

$$\frac{dy}{dt} = k_1[Itk^0 - x - y][IP_4] - k_{-1}y - \frac{dx_2}{dt} \quad (13)$$

where, k_1 and k_{-1} are the usual binding unbinding rates while k_2 is the high affinity augmentation rate. x is the sum of x_1 and x_2 . In the steady state we have,

$$\begin{aligned} [PIP_3^0 - x_s]y_s - x_{2s}[S^0 - y_s] &= 0 \\ [Itk^0 - x_s - y_s][S^0 - y_s] - K_D y_s &= 0 \\ [Itk^0 - x_s - y_s][PIP_3^0 - x_s] - K_D x_{1s} &= 0 \end{aligned} \quad (14)$$

The subscript “s” is used denote steady state concentrations. From Eqn (14) it is apparent that

$$\begin{aligned} \frac{[PIP_3^0 - x_s]}{[S^0 - y_s]} &= \frac{x_{1s}}{y_s} \\ [S^0 - y_s] &= \frac{y_s [PIP_3^0 - x_s]}{x_{2s}} \end{aligned} \quad (15)$$

which implies $x_{1s} = x_{2s}$ for nonzero values of y_s . Making use of this fact we have,

$$K_D x_s (x_s - 2PIP_3^0) - 2(PIP_3^0 - x_s) \{ (2PIP_3^0 + S^0 - x_s)x_s + Itk^0(x_s - 2PIP_3^0) \} = 0 \quad (16)$$

Eqn(16) is a cubic equation yielding three real roots for the values of K_D , PIP_3^0 and Itk^0 we have used. However, only one root provides physically meaningful result, the other roots create an unphysical situation where $x_s > Itk^0$. We show the variation of x_s with two different values of K_D below (Fig. S11). Following similar analysis as in Fig. S10, we find that a large number of substrate is required to bring down the activation of PIP_3 bound Itk . A_{max} in this case was calculated by taking a limit $S^0 \rightarrow 0$, note, x_s has a discontinuity at $S^0=0$.

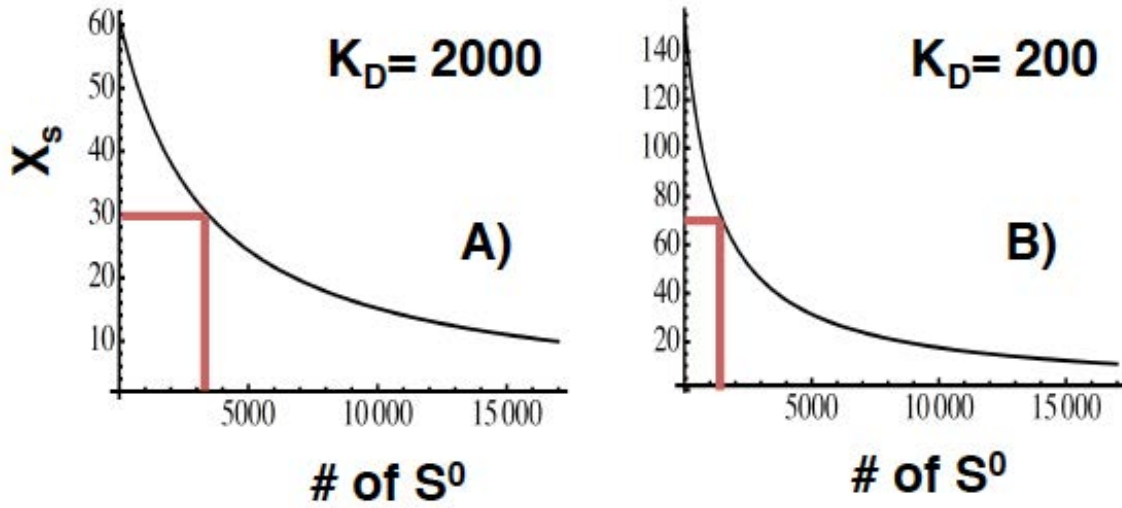


Fig. S11: A large concentration of IP_4 is required to replace PIP_3 in model M4. A) Variation of the steady state x_s (Itk- PIP_3) as a function of initial substrate (PIP_2) concentration S^0 when the $K_D = 2000$. B) Same as in A) for $K_D = 200$.

Variation of R with increasing initial concentrations of Itk and PIP_3 for models M1-M6

The asymmetry ratio, R , is calculated using, $R = \tau_w / \tau_p = [(\tau_p - t_1) + \tau_d] / \tau_p$, where, τ_w is the width of the temporal profile of the concentration of PIP_3 bound Itk. τ_w can be expressed in terms of the decay time, τ_d , t_1 (the time system takes to reach half of the peak concentration) and the peak time τ_p . We aimed to understand the variation of R with increasing Itk^0 and PIP_3^0 (Fig. 2) based on the results described in the last two sections.

Models M1 and M3

The asymmetry ratio, R , increases as Itk^0 and PIP_3^0 are increased. Our calculations show (Fig. S9) that τ_w does not vary appreciably as Itk^0 and PIP_3^0 are increased in the range of moderate to high values. This occurs because the decay time, τ_d , is primarily determined by the small unbinding rate of PIP_3 from the stable $IP_4 - Itk - Itk-PIP_3$ complex. Since τ_d is much larger than the peak time in this range, τ_w is mainly determined by τ_d in this range of concentrations. The increase in R , hence, arises from the decrease in τ_p as Itk^0 and PIP_3^0 are increased. The concentration dependence of this variation is determined by Eq. (5). At lower concentrations of Itk^0 and PIP_3^0 , both τ_w and τ_d decrease, as Itk^0 and PIP_3^0 are decreased, however, τ_p decreases at a faster rate compared to τ_d , resulting in increasing R values.

Model M2

In this model, in contrast to models M1 and M3, the asymmetry ratio, R , initially decreases with increasing Itk^0 and PIP_3^0 , and, then at larger values of Itk^0 and PIP_3^0 starts increasing with increasing Itk^0 and PIP_3^0 . At smaller values of Itk^0 and PIP_3^0 , τ_w , decreases (Fig. S9A) at a much faster rate as compared to τ_p , as Itk^0 and PIP_3^0 are increased. At higher values of Itk^0 and PIP_3^0 , τ_w does not change appreciably with increasing initial concentrations because of the same mechanisms as described for M1 and M3. However, in this range of concentrations τ_p decreases with increasing Itk^0 and PIP_3^0 resulting in increased R as the initial concentrations increase.

Models M5 and M6

For these models, τ_d is substantially larger than τ_p , therefore, τ_w is well approximated by τ_d . Since τ_p does not change appreciably, but τ_d decreases with increasing Itk^0 and PIP_3^0 we see a decrease in the ratio R as the initial concentrations are increased.

Model M4

τ_w behaves in a very similar manner to models M5 and M6. τ_p for M4 decreases with increasing Itk^0 and PIP_3^0 following Eqn (5), however, the rate of the decrease is still smaller than that of τ_w , which results in decrease in the values of R as the initial concentrations are increased.

Model 7 can be analyzed in a similar way.

Relative Entropy calculation

The continuous relative entropy is defined as

$$D_{\text{KL}} = \int_{x \in K} p(x) \log \frac{p(x)}{q(x)} dx \quad (17)$$

where, $p(x)$ is the distribution of the parameters denoted by $x \in K$, which is subject to constraints imposed by experiments, and, $q(x)$ is a uniform distribution, such that $q(x) = 1/|K|$ for all $x \in K$. Now we seek for $p(x)$ which maximizes Eqn (17) under the constraints:

$$\int_{x \in K} R(x) p(x) dx = R_{\text{avg}} = R_{\text{exp}}$$
$$\int_{x \in K} \tau(x) p(x) dx = \tau_{\text{avg}} = \tau_{\text{exp}}$$

$$\begin{aligned}
\int_{x \in K} A(x)p(x)dx &= A_{avg} = A_{exp} \\
\int_{x \in K} p(x)dx &= 1
\end{aligned}
\tag{18}$$

We use three Lagrange multipliers (λ , λ_1 , λ_2 and λ_3) to incorporate the constraints in Eq. (18) and maximize the following function:

$$\begin{aligned}
G(p, \lambda, \lambda_1, \lambda_2, \lambda_3) &= \int_{x \in K} p(x) \log \frac{p(x)}{q(x)} dx + \lambda \left(\int_{x \in K} p(x) - 1 \right) + \lambda_1 \left(\int_{x \in K} R(x)p(x) dx - R_{avg} \right) + \lambda_2 \left(\int_{x \in K} \tau(x)p(x) dx - \tau_{avg} \right) \\
&\quad + \lambda_3 \left(\int_{x \in K} A(x)p(x) dx - A_{avg} \right) \\
\frac{\partial G}{\partial p} = 0 &\Rightarrow \log \frac{p(x)}{q(x)} + 1 + \lambda + \lambda_1 R(x) + \lambda_2 \tau(x) + \lambda_3 A(x) = 0 \\
\frac{\partial G}{\partial \lambda} = 0 &\Rightarrow \int_{x \in K} p(x) dx = 1 \\
\frac{\partial G}{\partial \lambda_1} = 0 &\Rightarrow \int_{x \in K} R(x)p(x) dx = R_{avg} \\
\frac{\partial G}{\partial \lambda_2} = 0 &\Rightarrow \int_{x \in K} \tau(x)p(x) dx = \tau_{avg} \\
\frac{\partial G}{\partial \lambda_3} = 0 &\Rightarrow \int_{x \in K} A(x)p(x) dx = A_{avg}
\end{aligned}
\tag{19}$$

From Eqn (19) it is clear that

$$\begin{aligned}
p(x) &= \frac{q(x)e^{-\lambda_1 R(x) - \lambda_2 \tau(x) - \lambda_3 A(x)}}{\int_{x \in K} q(x)e^{-\lambda_1 R(x) - \lambda_2 \tau(x) - \lambda_3 A(x)}} \\
R_{avg} &= \frac{\int_{x \in K} R(x)q(x)e^{-\lambda_1 R(x) - \lambda_2 \tau(x) - \lambda_3 A(x)}}{\int_{x \in K} q(x)e^{-\lambda_1 R(x) - \lambda_2 \tau(x) - \lambda_3 A(x)}} \\
\tau_{avg} &= \frac{\int_{x \in K} \tau(x)q(x)e^{-\lambda_1 R(x) - \lambda_2 \tau(x) - \lambda_3 A(x)}}{\int_{x \in K} q(x)e^{-\lambda_1 R(x) - \lambda_2 \tau(x) - \lambda_3 A(x)}} \\
A_{avg} &= \frac{\int_{x \in K} A(x)q(x)e^{-\lambda_1 R(x) - \lambda_2 \tau(x) - \lambda_3 A(x)}}{\int_{x \in K} q(x)e^{-\lambda_1 R(x) - \lambda_2 \tau(x) - \lambda_3 A(x)}}
\end{aligned}$$

We substituted the $p(x)$ from Eq. (19) in the equations for R_{avg} , τ_{avg} and A_{avg} (Eq. 18), and solved for λ_1 , λ_2 and λ_3 when the values of R_{avg} and τ_{avg} were taken from the table II in the main text. Owing to the lack of knowledge about the absolute value of A_{avg} , we have used some A_{avg} , which all the models can yield. (We have also varied the A_{avg} , to study how the dependence of the robustness on the choice of A_{avg}). Then we calculate the Kullback-Leibler distance

$$D_{KL} = \int_{x \in K} p(x) \log \frac{p(x)}{q(x)} dx \quad (20)$$

for each model.

Range of parameter variation: For the results shown in Fig. S12, 13, 14, 15,16, 17, 19, 20, 21, 22 and 23, the rate constants were chosen from uniform distributions with lower and upper bounds equal to 1/10 and 10 times, respectively, the base values shown in tables S1-S7. We used 100,000 sample points, each point representing a set of rate constants and initial concentrations for all the models. For models M1-M3 the high affinity binding unbinding rates are drawn from a uniform distribution whilst the low affinity K_D is determined as $K_D^{low} = \alpha K_D^{high}$, where α is drawn from a uniform distribution with lower and upper bound of 1 and 4000 respectively. For M7, while high affinity binding and unbinding rates are drawn from a uniform distribution, α is chosen uniformly from 1 to 50. The initial concentrations of Itk and PIP₃ were varied within a 35% (11) range from uniform distributions centered at the base values shown in table S8.

Histograms of the asymmetry ratio (R) and the peak time τ_p for low, moderately high and high stimulation.

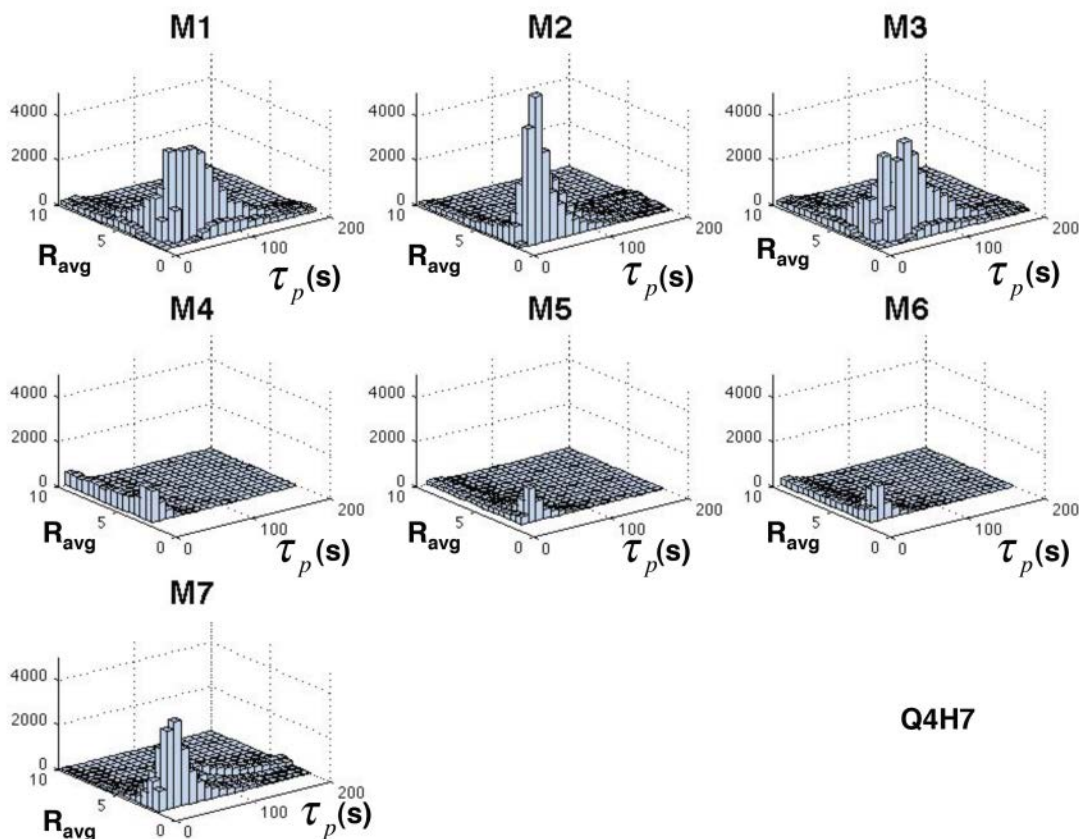
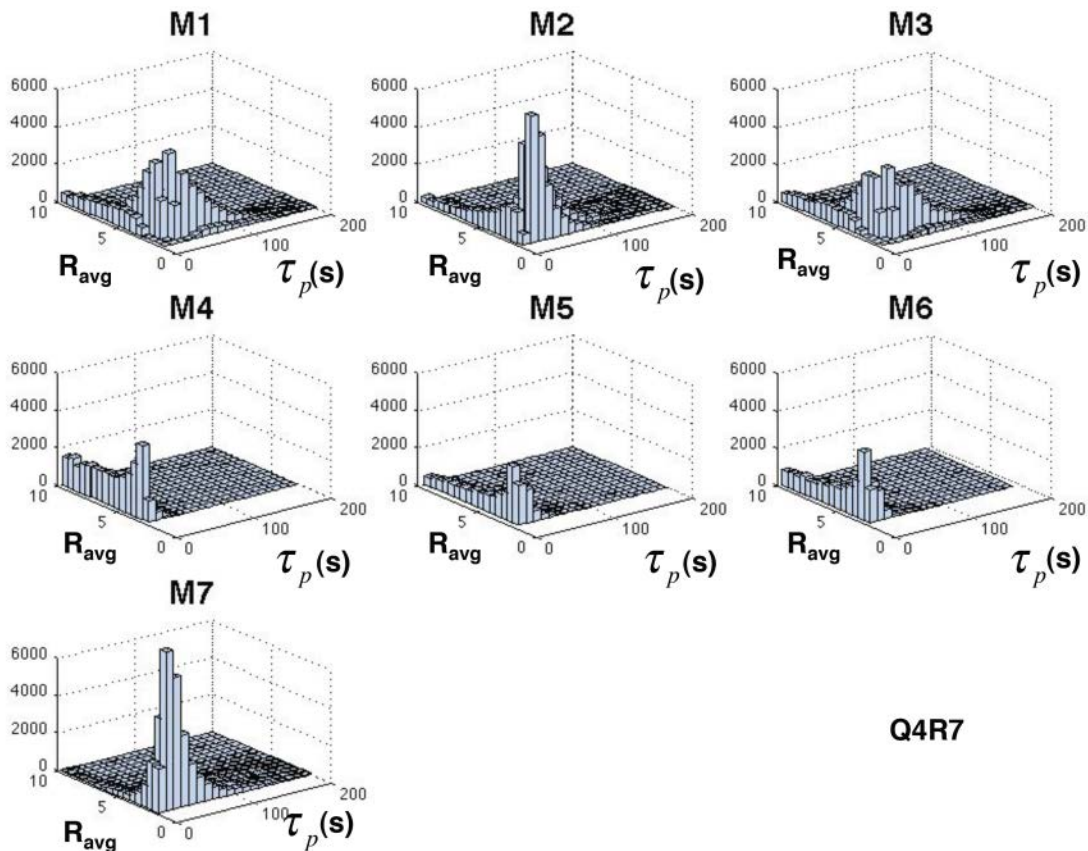
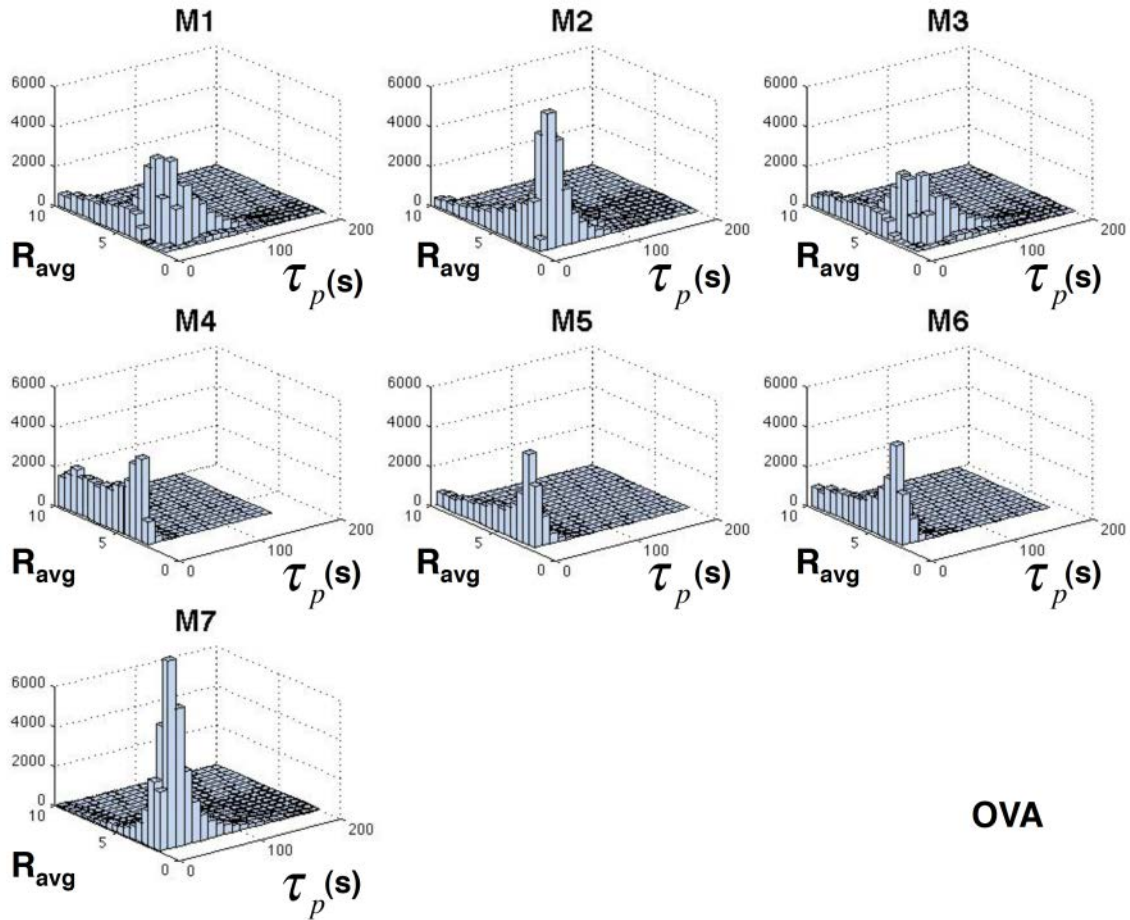


Fig. S12: The histograms for R and τ as the parameters are varied in all 7 models for moderately low initial concentrations of Itk^0 and PIP_3^0 . All the rate constants are varied by two orders of magnitude with the constraint $K_D^{\text{low}} = \alpha K_D^{\text{high}}$. For M1-M3, α is distributed uniformly over 1 to 4000 while for M7 it is distributed uniformly over 1 to 50. The initial concentrations of species involved are varied in a 35% window about the base value of $\text{Itk}^0 = 40$, $\text{PIP}_3^0 = 130$ and $\text{PIP}_2^0 = 17000$.



S13: The histograms for R and τ as the parameters are varied in all 7 models for moderately high initial concentrations of Itk^0 and PIP_3^0 . All the rate constants are varied by two orders of magnitude with the constraint $K_D^{\text{low}} = \alpha K_D^{\text{high}}$. For M1-M3, α is distributed uniformly over 1 to 4000 while for M7 it is distributed uniformly over 1 to 50. The initial concentrations of species involved are varied in a 35% window about the base value of $\text{Itk}^0 = 100$, $\text{PIP}_3^0 = 370$ and $\text{PIP}_2^0 = 17000$.



S14: The histograms for R and τ as the parameters are varied in all 7 models for high initial concentrations of Itk^0 and PIP_3^0 . All the rate constants are varied by two orders of magnitude with the constraint $K_D^{\text{low}} = \alpha K_D^{\text{high}}$. For M1-M3, α is distributed uniformly over 1 to 4000 while for M7 it is distributed uniformly over 1 to 50. The initial concentrations of species involved are varied in a 35% window about the base value of $\text{Itk}^0 = 140$, $\text{PIP}_3^0 = 530$ and $\text{PIP}_2^0 = 17000$.

The checkerboard plot of the most robust models for different peptide affinities as the R_{avg} and A_{avg} are varied.

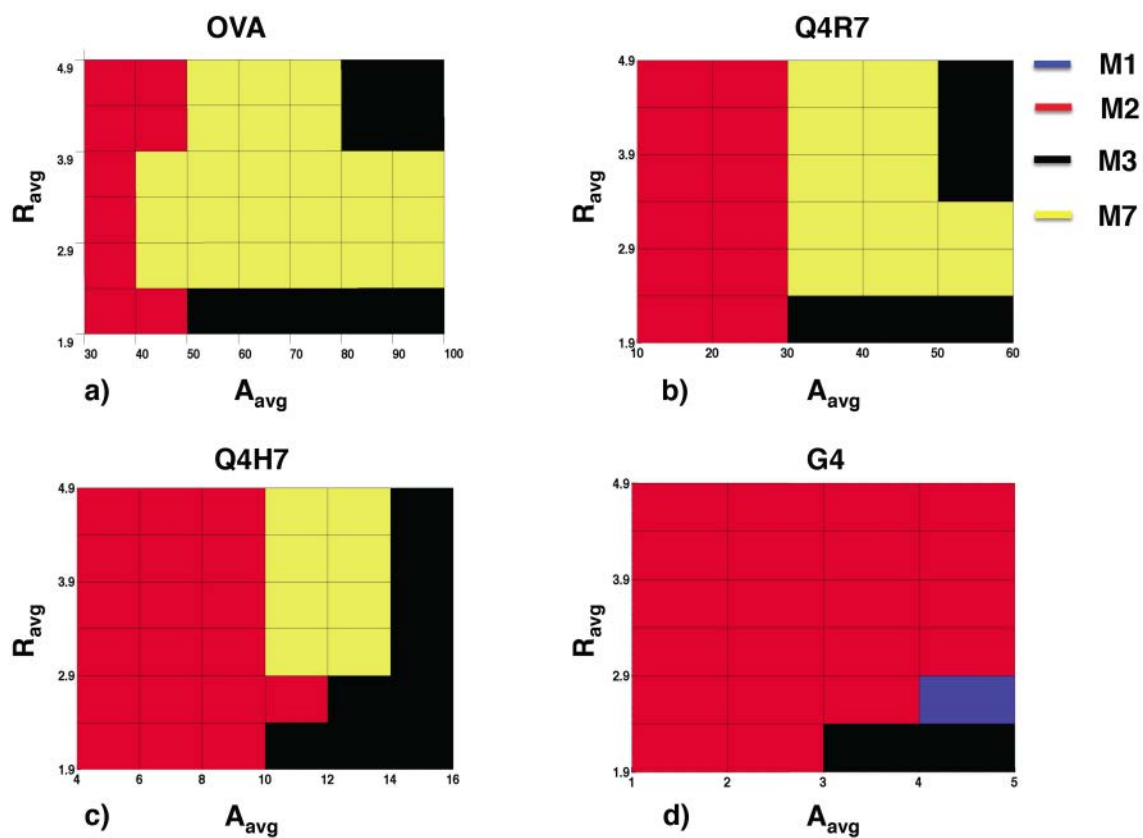


Fig. S15: Checkerboard plot of the most robust models for different ligand affinities as R_{avg} and A_{avg} are varied for a fixed $\tau_{avg} = 2\text{mins}$. a) Plot of the most robust models for $Itk^0 = 140$ and $PIP_3^0 = 530$ molecules. b) The same plot as a) for $Itk^0 = 100$ and $PIP_3^0 = 370$ molecules. c) Same plot as a) for $Itk^0 = 40$ and $PIP_3^0 = 130$ molecules. d) The same plot as a) for $Itk^0 = 20$ and $PIP_3^0 = 50$ molecules.

Relative robustness of the seven models for specific amplitude averages as the ligand affinities are varied.

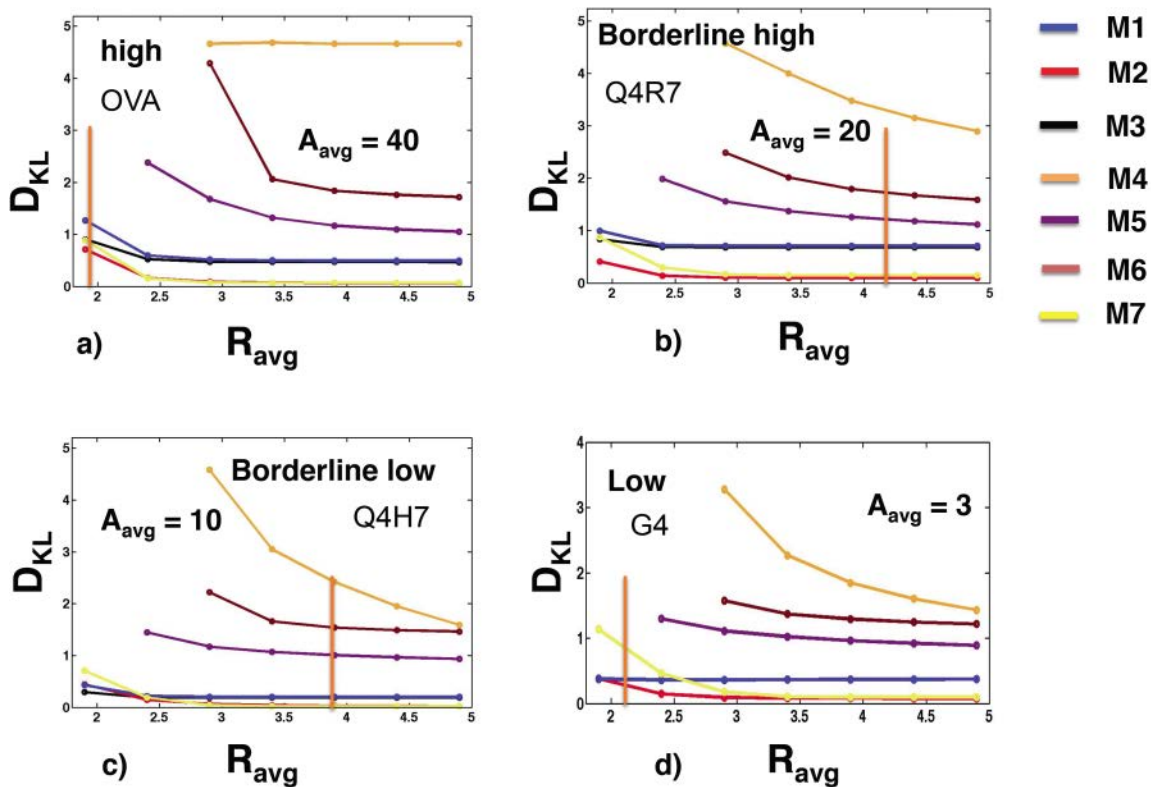


Fig. S16: Plots of the relative robustness of all the 7 models for a specific A_{avg} for different ligand affinities as R_{avg} is varies for a fixed $\tau_{avg} = 2\text{mins}$. **a)** For $Itk^0 = 140$ and $PIP_3^0 = 530$ molecules the D_{KL} is shown for an A_{avg} of 40 molecules. **b)** The same plot as **a)** for $Itk^0 = 100$ and $PIP_3^0 = 370$ molecules when the A_{avg} is held fixed at 20 molecules. **c)** Same plot as **a)** for $Itk^0 = 40$ and $PIP_3^0 = 130$ molecules when $A_{avg} = 10$ molecules. **d)** The same plot as **a)** for $Itk^0 = 20$ and $PIP_3^0 = 50$ molecules when $A_{avg} = 3$ molecules. The orange vertical bar in all the plots show the experimentally observed value of R_{avg} (table I main text).

The effect of Lck mediated phosphorylation of PIP_3 bound Itk complex.

We have studied the effect of Lck mediated phosphorylation of membrane bound Itk at its Y511 residue. Here the membrane bound Itk is phosphorylated by Lck (modeled as a first order reaction). Upon activation it becomes active (denoted by Itk^{act} except for M4 where it is denoted as Itk_{act}). Only an active form of Itk is capable of producing IP_4 from the hydrolysis of PIP_2 . The activation and de-activation rates of membrane bound Itk is chosen so that the kinetics of active Itk roughly agrees with the experimental data in the main text and (3). The reactions and the reaction rates are detailed in table S9-S15. We find that adding the Lck mediated phosphorylation of the membrane bound Itk does not alter the rank order of the models.

Table S9: Reactions and rate constants for model M1^{lck}.

Reactions	k_{on} ($\mu\text{M}^{-1}\text{s}^{-1}$)	k_{off} (s^{-1})	K_D (μM)	k_{cat} ($\mu\text{M}^{-1}\text{s}^{-1}$)	k_{ac} (s^{-1})	k_{deac} (s^{-1})
$Itk - Itk + PIP_3 \leftrightarrow Itk - Itk - PIP_3$	2.5×10^{-4}	0.1	400			
$PIP_3 - Itk - Itk + PIP_3 \leftrightarrow PIP_3 - Itk - Itk - PIP_3$	0.01	0.003	0.3			
$Itk - Itk + IP_4 \leftrightarrow Itk - Itk - IP_4$	2.5×10^{-3}	0.1	40			
$PIP_3 - Itk - Itk + IP_4 \leftrightarrow PIP_3 - Itk - Itk - IP_4$	0.1	0.003	0.03			
$IP_4 - Itk - Itk + PIP_3 \leftrightarrow IP_4 - Itk - Itk - PIP_3$	0.01	0.003	0.3			
$IP_4 - Itk - Itk + IP_4 \leftrightarrow IP_4 - Itk - Itk - IP_4$	0.1	0.003	0.03			
$IP_4 - Itk - Itk^{act} - PIP_3 + S \rightarrow IP_4 + IP_4 - Itk - Itk^{act} - PIP_3$				1.5×10^{-4}		
$Itk - Itk^{act} - PIP_3 + S \rightarrow IP_4 + Itk - Itk^{act} - PIP_3$				1.5×10^{-4}		
$PIP_3 - Itk - Itk^{act} - PIP_3 + S \rightarrow IP_4 + PIP_3 - Itk - Itk^{act} - PIP_3$				1.5×10^{-4}		
$Itk - Itk - PIP_3 \leftrightarrow Itk - Itk^{act} - PIP_3$					0.3	0.09
$IP_4 - Itk - Itk - PIP_3 \leftrightarrow IP_4 - Itk - Itk^{act} - PIP_3$					0.3	0.09
$PIP_3 - Itk - Itk - PIP_3 \leftrightarrow PIP_3 - Itk - Itk^{act} - PIP_3$					0.3	0.09
$Itk - Itk^{act} - PIP_3 \rightarrow Itk - Itk + PIP_3$		0.1				
$IP_4 - Itk - Itk^{act} - PIP_3 \leftrightarrow Itk - Itk^{act} - PIP_3 + IP_4$	0.1	0.003	0.03			
$IP_4 - Itk - Itk^{act} - PIP_3 \leftrightarrow Itk - Itk - IP_4 + PIP_3$	0.01	0.003	0.3			
$PIP_3 - Itk - Itk^{act} - PIP_3 \leftrightarrow Itk - Itk^{act} - PIP_3 + PIP_3$	0.01	0.003	0.3			

Table S10: Reactions and rate constants for model M2^{lck}.

Reactions	k_{on} ($\mu\text{M}^{-1}\text{s}^{-1}$)	k_{off} (s^{-1})	K_D (μM)	k_{cat} ($\mu\text{M}^{-1}\text{s}^{-1}$)	k_{ac} t (s^{-1})	k_{deac} t (s^{-1})
$I_{tk} - I_{tk} + PIP_3 \leftrightarrow I_{tk} - I_{tk} - PIP_3$	2.5 $\times 10^{-4}$	0.1	400			
$I_{tk} - I_{tk} + IP_4 \leftrightarrow I_{tk} - I_{tk} - IP_4$	2.5 $\times 10^{-3}$	0.1	40			
$PIP_3 - I_{tk} - I_{tk} + IP_4 \leftrightarrow PIP_3 - I_{tk} - I_{tk} - IP_4$	2.5 $\times 10^{-3}$	0.1	40			
$IP_4 - I_{tk} - I_{tk} + PIP_3 \leftrightarrow IP_4 - I_{tk} - I_{tk} - PIP_3$	0.01	0.003	0.3			
$IP_4 - I_{tk} - I_{tk} + IP_4 \leftrightarrow IP_4 - I_{tk} - I_{tk} - IP_4$	0.1	0.003	0.03			
$IP_4 - I_{tk} - I_{tk}^{act} - PIP_3 + S \rightarrow IP_4 + IP_4 - I_{tk} - I_{tk}^{act} - PIP_3$				1.5 $\times 10^{-4}$		
$I_{tk} - I_{tk}^{act} - PIP_3 + S \rightarrow IP_4 + I_{tk} - I_{tk}^{act} - PIP_3$				1.5 $\times 10^{-4}$		
$I_{tk} - I_{tk} - PIP_3 \leftrightarrow I_{tk} - I_{tk}^{act} - PIP_3$					0.3	0.09
$IP_4 - I_{tk} - I_{tk} - PIP_3 \leftrightarrow IP_4 - I_{tk} - I_{tk}^{act} - PIP_3$					0.3	0.09
$I_{tk} - I_{tk}^{act} - PIP_3 \rightarrow I_{tk} - I_{tk} + PIP_3$		0.1				
$IP_4 - I_{tk} - I_{tk}^{act} - PIP_3 \leftrightarrow I_{tk} - I_{tk}^{act} - PIP_3 + IP_4$	2.5 $\times 10^{-3}$	0.1	40			
$IP_4 - I_{tk} - I_{tk}^{act} - PIP_3 \leftrightarrow I_{tk} - I_{tk} - IP_4 + PIP_3$	0.01	0.003	0.3			

Table S11: Reactions and rate constants for model M3^{lck}.

Reactions	k_{on} ($\mu\text{M}^{-1}\text{s}^{-1}$)	k_{off} (s^{-1})	K_D (μM)	k_{cat} ($\mu\text{M}^{-1}\text{s}^{-1}$)	k_{act} t (s^{-1})	k_{deac} t (s^{-1})
$I_{tk} - I_{tk} + PIP_3 \leftrightarrow I_{tk} - I_{tk} - PIP_3$	2.5 $\times 10^{-4}$	0.1	400			
$I_{tk} - I_{tk} + IP_4 \leftrightarrow I_{tk} - I_{tk} - IP_4$	2.5 $\times 10^{-3}$	0.1	40			
$PIP_3 - I_{tk} - I_{tk} + IP_4 \leftrightarrow PIP_3 - I_{tk} - I_{tk} - IP_4$	0.1	0.003	0.03			

		3				
$IP_4 - Itk - Itk + PIP_3 \leftrightarrow IP_4 - Itk - Itk - PIP_3$	0.01	0.00 3	0.3			
$IP_4 - Itk - Itk + IP_4 \leftrightarrow IP_4 - Itk - Itk - IP_4$	0.1	0.00 3	0.03			
$IP_4 - Itk - Itk^{act} - PIP_3 + S \rightarrow IP_4 + IP_4 - Itk - Itk^{act} - PIP_3$				1.5 \times 10^{-4}		
$Itk - Itk^{act} - PIP_3 + S \rightarrow IP_4 + Itk - Itk^{act} - PIP_3$				1.5 \times 10^{-4}		
$Itk - Itk - PIP_3 \leftrightarrow Itk - Itk^{act} - PIP_3$					0.3	0.09
$IP_4 - Itk - Itk - PIP_3 \leftrightarrow IP_4 - Itk - Itk^{act} - PIP_3$					0.3	0.09
$Itk - Itk^{act} - PIP_3 \rightarrow Itk - Itk + PIP_3$		0.1				
$IP_4 - Itk - Itk^{act} - PIP_3 \leftrightarrow Itk - Itk^{act} - PIP_3 + IP_4$	0.1	0.00 3	0.03			
$IP_4 - Itk - Itk^{act} - PIP_3 \leftrightarrow Itk - Itk - IP_4 + PIP_3$	0.01	0.00 3	0.3			

Table S12: Reactions and rate constants for model M4^{lck}.

Reactions	k_{on} ($\mu M^{-1} s^{-1}$)	k_{off} (s^{-1})	K_D (μM)	k_{cat} ($\mu M^{-1} s^{-1}$)	k_{act} (s^{-1})	k_{deact} (s^{-1})
$Itk + PIP_3 \leftrightarrow Itk - PIP_3$	2.5×10^{-4}	0.1	400			
$Itk + IP_4 \leftrightarrow Itk^* - IP_4$	2.5×10^{-3}	0.1	40			
$Itk^* - IP_4 + PIP_3 \leftrightarrow Itk^* - PIP_3 + IP_4$	10					
$Itk_{act}^* - PIP_3 + S \rightarrow IP_4 + Itk_{act}^* - PIP_3$				1.5 \times 10^{-4}		
$Itk_{act} - PIP_3 + S \rightarrow IP_4 + Itk_{act} - PIP_3$				1.5 \times 10^{-4}		
$Itk - PIP_3 \leftrightarrow Itk_{act} - PIP_3$					0.3	0.09
$Itk^* - PIP_3 \leftrightarrow Itk_{act}^* - PIP_3$					0.3	0.09
$Itk_{act}^* - PIP_3 + IP_4 \rightarrow Itk^* - IP_4 + PIP_3$	10					

Table S13: Reactions and rate constants for model M5^{lck}.

Reactions	k_{on}	k_{off}	K_D	k_{cat}	k_{ac}	k_{deac}
-----------	----------	-----------	-------	-----------	----------	------------

	($\mu\text{M}^{-1}\text{s}^{-1}$)	(s^{-1})	(μM)	($\mu\text{M}^{-1}\text{s}^{-1}$)	t (s^{-1})	t (s^{-1})
$\text{Itk} - \text{Itk} + \text{PIP}_3 \leftrightarrow \text{Itk} - \text{Itk} - \text{PIP}_3$	1.25×10^{-4}	0.05	400			
$\text{PIP}_3 - \text{Itk} - \text{Itk} + \text{PIP}_3 \leftrightarrow \text{PIP}_3 - \text{Itk} - \text{Itk} - \text{PIP}_3$	1.25×10^{-4}	0.05	400			
$\text{Itk} - \text{Itk} + \text{IP}_4 \leftrightarrow \text{Itk} - \text{Itk} - \text{IP}_4$	1.25×10^{-3}	0.05	40			
$\text{PIP}_3 - \text{Itk} - \text{Itk} + \text{IP}_4 \leftrightarrow \text{PIP}_3 - \text{Itk} - \text{Itk} - \text{IP}_4$	1.25×10^{-3}	0.05	40			
$\text{IP}_4 - \text{Itk} - \text{Itk} + \text{PIP}_3 \leftrightarrow \text{IP}_4 - \text{Itk} - \text{Itk} - \text{PIP}_3$	1.25×10^{-4}	0.05	400			
$\text{IP}_4 - \text{Itk} - \text{Itk} + \text{IP}_4 \leftrightarrow \text{IP}_4 - \text{Itk} - \text{Itk} - \text{IP}_4$	1.25×10^{-3}	0.05	40			
$\text{IP}_4 - \text{Itk} - \text{Itk}^{\text{act}} - \text{PIP}_3 + \text{S} \rightarrow \text{IP}_4 + \text{IP}_4 - \text{Itk} - \text{Itk}^{\text{act}} - \text{PIP}_3$				1.5×10^{-4}		
$\text{Itk} - \text{Itk}^{\text{act}} - \text{PIP}_3 + \text{S} \rightarrow \text{IP}_4 + \text{Itk} - \text{Itk}^{\text{act}} - \text{PIP}_3$				1.5×10^{-4}		
$\text{PIP}_3 - \text{Itk} - \text{Itk}^{\text{act}} - \text{PIP}_3 + \text{S} \rightarrow \text{IP}_4 + \text{PIP}_3 - \text{Itk} - \text{Itk}^{\text{act}} - \text{PIP}_3$				1.5×10^{-4}		
$\text{Itk} - \text{Itk} - \text{PIP}_3 \leftrightarrow \text{Itk} - \text{Itk}^{\text{act}} - \text{PIP}_3$					0.3	0.09
$\text{IP}_4 - \text{Itk} - \text{Itk} - \text{PIP}_3 \leftrightarrow \text{IP}_4 - \text{Itk} - \text{Itk}^{\text{act}} - \text{PIP}_3$					0.3	0.09
$\text{PIP}_3 - \text{Itk} - \text{Itk} - \text{PIP}_3 \leftrightarrow \text{PIP}_3 - \text{Itk} - \text{Itk}^{\text{act}} - \text{PIP}_3$					0.3	0.09
$\text{Itk} - \text{Itk}^{\text{act}} - \text{PIP}_3 \rightarrow \text{Itk} - \text{Itk} + \text{PIP}_3$		0.05				
$\text{IP}_4 - \text{Itk} - \text{Itk}^{\text{act}} - \text{PIP}_3 \leftrightarrow \text{Itk} - \text{Itk}^{\text{act}} - \text{PIP}_3 + \text{IP}_4$	1.25×10^{-3}	0.05	40			
$\text{IP}_4 - \text{Itk} - \text{Itk}^{\text{act}} - \text{PIP}_3 \leftrightarrow \text{Itk} - \text{Itk} - \text{IP}_4 + \text{PIP}_3$	1.25×10^{-4}	0.05	400			
$\text{PIP}_3 - \text{Itk} - \text{Itk}^{\text{act}} - \text{PIP}_3 \leftrightarrow \text{Itk} - \text{Itk}^{\text{act}} - \text{PIP}_3 + \text{PIP}_3$	1.25×10^{-4}	0.05	400			

Table S14: Reactions and rate constants for model M6^{lck}.

Reactions	k_{on} ($\mu\text{M}^{-1}\text{s}^{-1}$)	k_{off} (s^{-1})	K_D (μM)	k_{cat} ($\mu\text{M}^{-1}\text{s}^{-1}$)	k_{act} (s^{-1})	k_{deact} (s^{-1})
$Itk + PIP_3 \leftrightarrow Itk - PIP_3$	1.25 $\times 10^{-4}$	0.05	400			
$Itk + IP_4 \longleftrightarrow Itk - IP_4$	1.25 $\times 10^{-3}$	0.05	40			
$Itk - PIP_3 \leftrightarrow Itk^{act} - PIP_3$					0.3	0.09
$Itk^{act} - PIP_3 \rightarrow Itk + PIP_3$		0.05				
$Itk^{act} - PIP_3 + S \rightarrow IP_4 + Itk^{act} - PIP_3$				1.5 $\times 10^{-4}$		

Table S15: Reactions and rate constants for model M7^{lck}.

Reactions	k_{on} ($\mu\text{M}^{-1}\text{s}^{-1}$)	k_{off} (s^{-1})	K_D (μM)	k_{cat} ($\mu\text{M}^{-1}\text{s}^{-1}$)	k_{ac} (s^{-1})	k_{deac} (s^{-1})
$Itk - Itk + PIP_3 \leftrightarrow Itk - Itk - PIP_3$	2.5 $\times 10^{-4}$	0.0 1	40			
$PIP_3 - Itk - Itk + PIP_3 \leftrightarrow PIP_3 - Itk - Itk - PIP_3$	0.01	0.1	10			
$Itk - Itk + IP_4 \leftrightarrow Itk - Itk - IP_4$	2.5 $\times 10^{-3}$	0.0 1	4			
$PIP_3 - Itk - Itk + IP_4 \leftrightarrow PIP_3 - Itk - Itk - IP_4$	2.5 $\times 10^{-3}$	0.0 1	4			
$IP_4 - Itk - Itk + PIP_3 \leftrightarrow IP_4 - Itk - Itk - PIP_3$	0.01	0.1	10			
$IP_4 - Itk - Itk + IP_4 \leftrightarrow IP_4 - Itk - Itk - IP_4$	0.1	0.1	1			
$IP_4 - Itk - Itk^{act} - PIP_3 + S \rightarrow IP_4 + IP_4 - Itk - Itk^{act} - PIP_3$				1.5 $\times 10^{-4}$		
$Itk - Itk^{act} - PIP_3 + S \rightarrow IP_4 + Itk - Itk^{act} - PIP_3$				1.5 $\times 10^{-4}$		
$PIP_3 - Itk - Itk^{act} - PIP_3 + S \rightarrow IP_4 + PIP_3 - Itk - Itk^{act} - PIP_3$				1.5 $\times 10^{-4}$		

$Itk - Itk - PIP_3 \leftrightarrow Itk - Itk^{act} - PIP_3$					0.3	0.09
$IP_4 - Itk - Itk - PIP_3 \leftrightarrow IP_4 - Itk - Itk^{act} - PIP_3$					0.3	0.09
$PIP_3 - Itk - Itk - PIP_3 \leftrightarrow PIP_3 - Itk - Itk^{act} - PIP_3$					0.3	0.09
$Itk - Itk^{act} - PIP_3 \rightarrow Itk - Itk + PIP_3$		0.1				
$IP_4 - Itk - Itk^{act} - PIP_3 \leftrightarrow Itk - Itk^{act} - PIP_3 + IP_4$	2.5×10^{-3}	0.01	4			
$IP_4 - Itk - Itk^{act} - PIP_3 \leftrightarrow Itk - Itk - IP_4 + PIP_3$	2.5×10^{-4}	0.01	40			
$PIP_3 - Itk - Itk^{act} - PIP_3 \leftrightarrow Itk - Itk^{act} - PIP_3 + PIP_3$	2.5×10^{-4}	0.01	40			

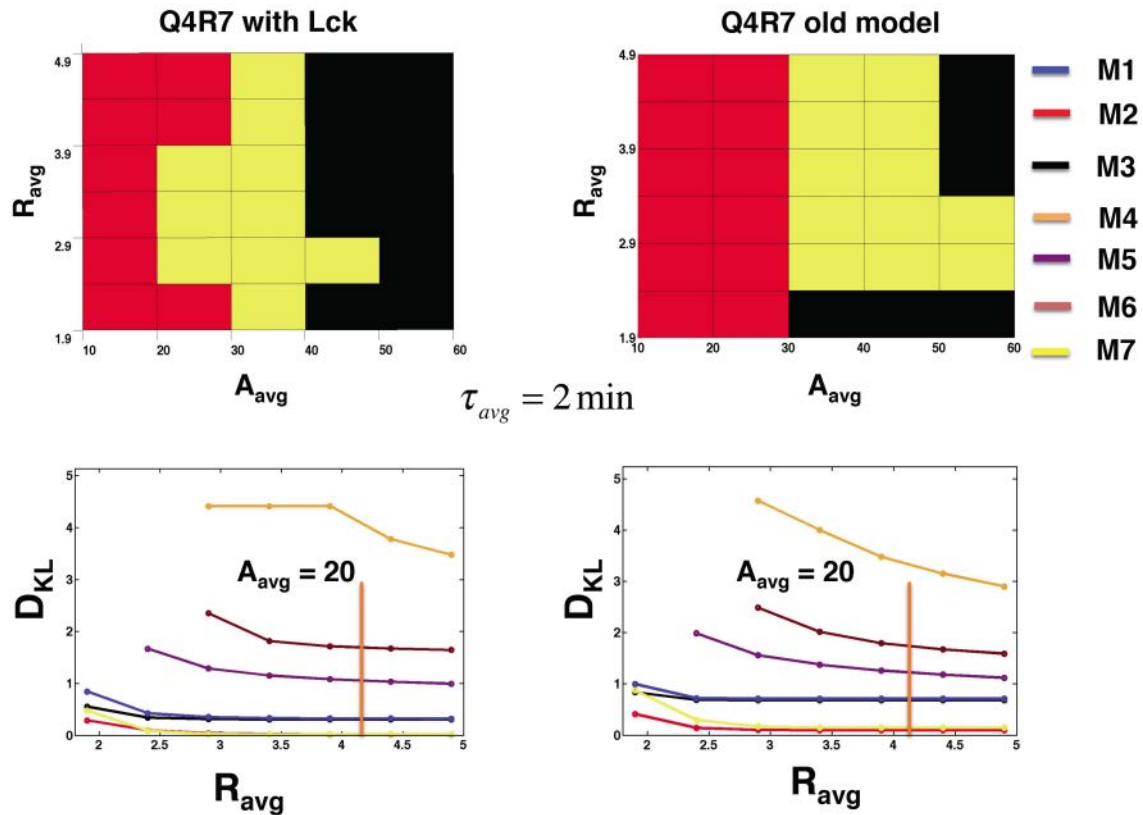


Fig. S17: The effect of Lck mediated phosphorylation of Itk-PIP₃ on the relative robustness of M1-M7. Upper panel (left most corner): For $Itk^0 = 100$ and $PIP_3^0 = 370$ the most robust models are shown as amplitude and the ratio of the Itk-PIP₃ kinetics are varied in presence of the Lck mediated phosphorylation of membrane recruited Itk at its Y511 residue. The average peak time is held at 2 mins. Upper panel (right most corner):

The same plot without any Lck mediated activation. Lower panel (left most corner): The relative robustness of the models M1-M7 for an amplitude average of 20 molecules in presence of Lck mediated activation of Itk. Lower panel (right most corner): Same plot without the explicit Lck mediated activation.

Anti-CD3 and anti-CD3/CD4 antibody stimulation of polyclonal *MHC-DKO* thymocytes.

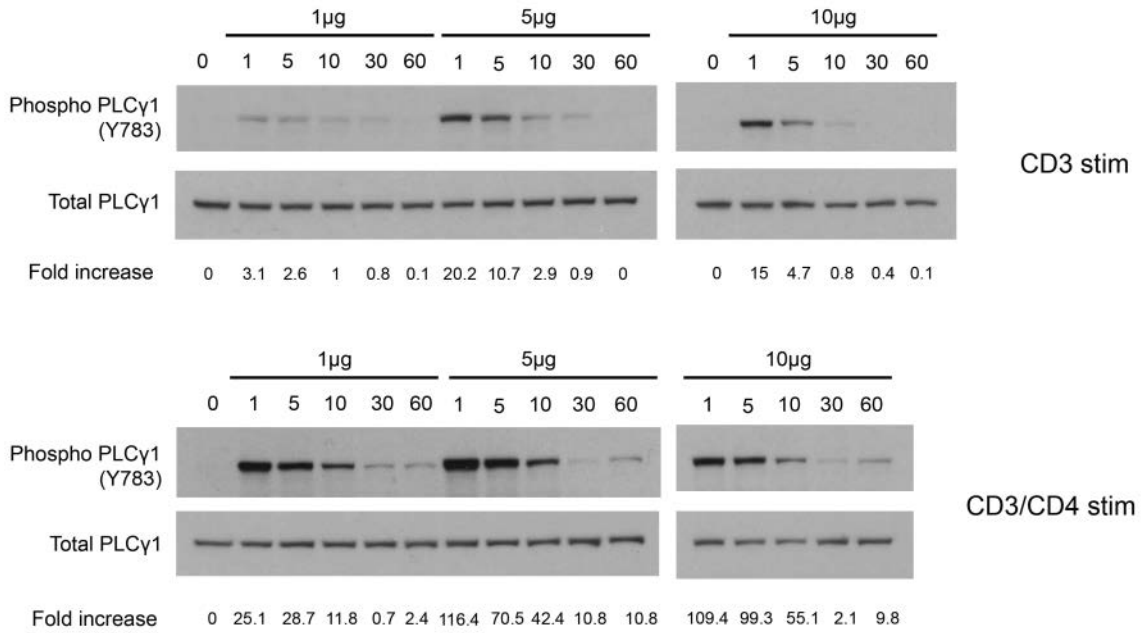


Fig. S18: Kinetics of induction of PLCγ1 phosphorylation represented as the fold increase over non stimulated cells using total PLCγ1 protein as a loading control.

Table S16: Values of peak time, peak width, and asymmetry ratio R calculated from the PLCγ1 activation kinetics in Fig. S18

CD3 μg / mL	peak time (τ_p) (mins.)	peak width (τ_w) (mins.)	R
1	1.0	8.0	8.0
5	1.0	5.5	5.5

CD3 & CD4 μg / mL	peak time (τ_p) (mins.)	peak width (τ_w) (mins.)	R
1	5.0	9.0	1.8
5	1.0	7.0	7.0

Checkerboard plot of the most robust models as R_{avg} and A_{avg} are varied for different doses of anti-CD3 and anti-CD3/CD4 antibodies.

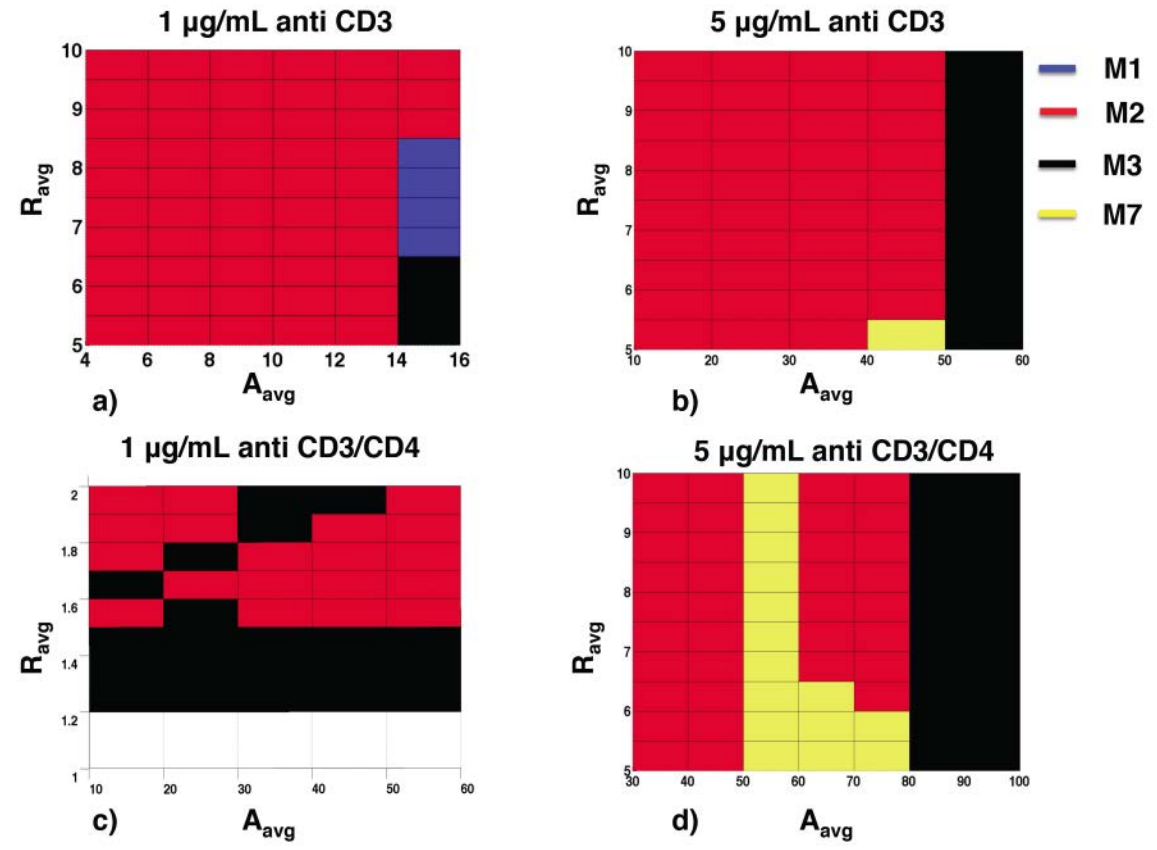


Fig. S19: **a)** $I_{tk}^0 = 40$ and $PIP_3^0 = 130$ molecules are used to emulate the 1 µg/ mL anti CD3 stimulation. The τ_{avg} is held at 1 mins. The checkerboard diagram of the most robust models is shown as R_{avg} and A_{avg} are varied. **b)** Same as plot **a)** but $I_{tk}^0 = 100$ and $PIP_3^0 = 370$ molecules are used as the initial concentrations. **c)** $I_{tk}^0 = 100$ and $PIP_3^0 = 370$ molecules are used to emulate the 1 µg/ mL anti CD3/CD4 stimulation. The τ_{avg} is held at 5 mins. The checkerboard diagram of the most robust models is shown as R_{avg} and A_{avg} are varied. **d)** $I_{tk}^0 = 140$ and $PIP_3^0 = 530$ molecules are used to emulate the 5 µg/ mL anti CD3/CD4 stimulation. The τ_{avg} is held at 1 mins. The checkerboard diagram of the most robust models is shown as R_{avg} and A_{avg} are varied.

The plot of D_{KL} for all the 7 models for a specific amplitude and different initial conditions for different doses of anti CD3 or anti CD3/CD4 antibodies.

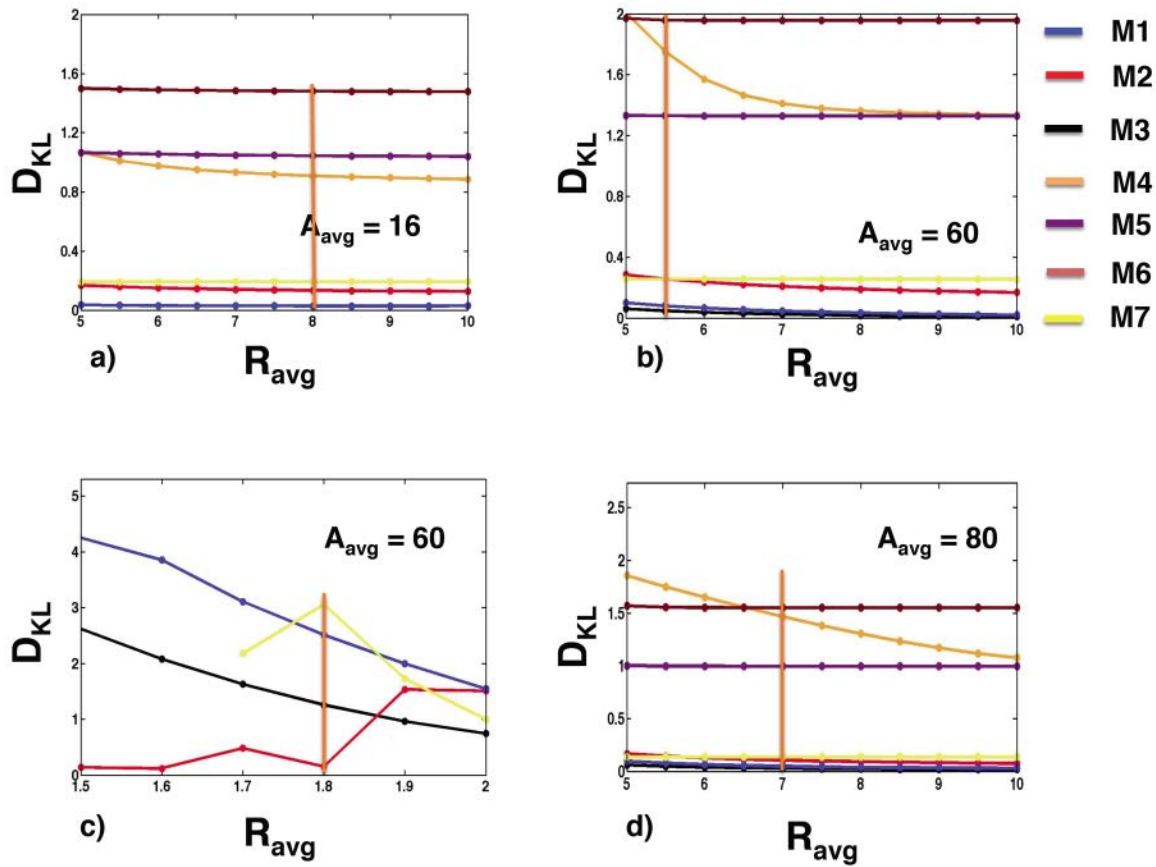


Fig S20: a) $I_{tk}^0 = 40$ and $PIP_3^0 = 130$ molecules are used to emulate the $1 \mu\text{g}/\text{mL}$ anti CD3 stimulation. The τ_{avg} is held at 1 mins. The D_{KL} is shown for an $A_{\text{avg}} = 16$ molecules. b) Same as plot a) but $I_{tk}^0 = 100$ and $PIP_3^0 = 370$ molecules are used as the initial concentrations and $A_{\text{avg}} = 60$ molecules. c) $I_{tk}^0 = 100$ and $PIP_3^0 = 370$ molecules are used to emulate the $1 \mu\text{g}/\text{mL}$ anti CD3/CD4 stimulation. The τ_{avg} is held at 5 mins. $A_{\text{avg}} = 60$ molecules. d) $I_{tk}^0 = 140$ and $PIP_3^0 = 530$ molecules are used to emulate the $5 \mu\text{g}/\text{mL}$ anti CD3/CD4 stimulation. The τ_{avg} is held at 1 mins and A_{avg} is set equal to 80 molecules. The vertical orange bar shows the observed experimental values (Table S16).

Dependence of D_{KL} on parameters those weakly influence the I_{tk} - PIP_3 kinetics.

Let us assume that the peak time τ_p , the amplitude A and the ratio R depend on n parameters. If we add m new parameters, which do not in any way influence the outcome of the I_{tk} - PIP_3 kinetics then the joint probability distribution that maximizes the entropy with the constraints becomes

$$p(k_1, \dots, k_{n+m}) = p(k_1, \dots, k_n) p(k_{n+1}, \dots, k_{n+m})$$

Now as k_{n+1}, \dots, k_{n+m} are drawn from a uniform distribution and they do not contribute anything to the observables, $p(k_{n+1}, \dots, k_{n+m}) = q(k_{n+1}, \dots, k_{n+m})$, where q is a uniform distribution. Therefore

$$D_{KL}^{new} = \int d^{n+m} k p(k_1, \dots, k_{n+m}) \ln \frac{p(k_1, \dots, k_{n+m})}{q(k_1, \dots, k_{n+m})} = \int d^n k p(k_1, \dots, k_n) \ln \frac{p(k_1, \dots, k_n)}{q(k_1, \dots, k_n)} \int d^m k p(k_{n+1}, \dots, k_{n+m})$$

$$= \int d^n k p(k_1, \dots, k_n) \ln \frac{p(k_1, \dots, k_n)}{q(k_1, \dots, k_n)} = D_{KL}^{old} \left(\because \int d^m k q(k_{n+1}, \dots, k_{n+m}) = 1 \right)$$

In order to probe the effect of parameters those weakly influence the kinetics of Itk-PIP₃ we have carried out a simulation for M3 with three added reactions. Instead of approximating the production of IP₄ from PIP₂ by a simple one step reaction, we have incorporated the fact that the membrane bound Itk phosphorylates PLCγ which in turn hydrolyses PIP₂ to form membrane bound DAG and soluble IP₃. IP₃ then gets converted into IP₄. In an effort to render the newly added parameters weak, we have chosen the rate constants in such a way that the PLCγ kinetics follow the Itk-PIP₃ kinetics and the turnover of IP₃ to IP₄ happens very quickly. The variations of these new parameters are confined within a two folds range. The details of the reactions are given in table S17. From Fig S21 we find that the D_{KL}^{new} and D_{KL}^{old} are very similar, differing only in the second place of decimal.

New reactions added to M3

Table S17

Reactions	$k_{forward}$	k_{back} (s ⁻¹)	k_{cat}
$Itk - PIP_3 + PLC\gamma \rightarrow Itk - PIP_3 + PLC\gamma^*$	5.0 μM ⁻¹ s ⁻¹		
$IP_4 - Itk - PIP_3 + PLC\gamma \rightarrow IP_4 - Itk - PIP_3 + PLC\gamma^*$	5.0 μM ⁻¹ s ⁻¹		
$PLC\gamma^* \rightarrow PLC\gamma$		8.0 s ⁻¹	
$PLC\gamma^* + S \rightarrow IP_3 + PLC\gamma^*$			1.5 × 10 ⁻⁴ μM ⁻¹ s ⁻¹
$IP_3 \rightarrow IP_4$			0.7 s ⁻¹

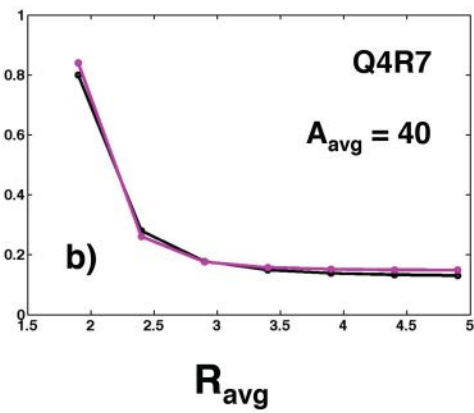
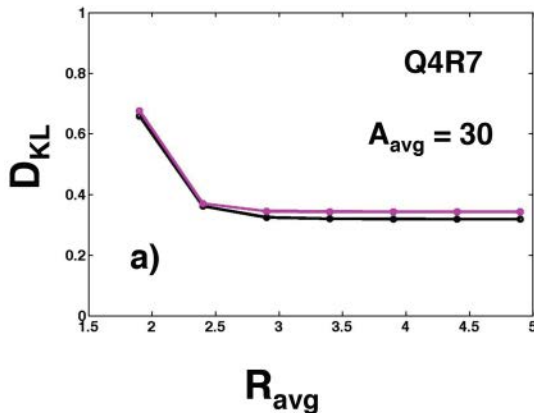


Fig. S21: Addition of parameters which weakly affect the Itk-PIP₃ kinetics, do not lead to any significant difference in the D_{KL} : For $Itk^0 = 100$ and $PIP_3^0 = 370$, **a)** we have looked at the relative difference in the D_{KL} of our old M3 (black) and M3 with the added reactions (magenta) for an amplitude average of 30 molecules and peak time average of 2 mins. **b)** We have looked at the relative difference in the D_{KL} of our old M3 (black) and M3 with the added reactions (magenta) for an amplitude average of 40 molecules and peak time average of 2 mins.

Convergence of the D_{KL} with the sample size

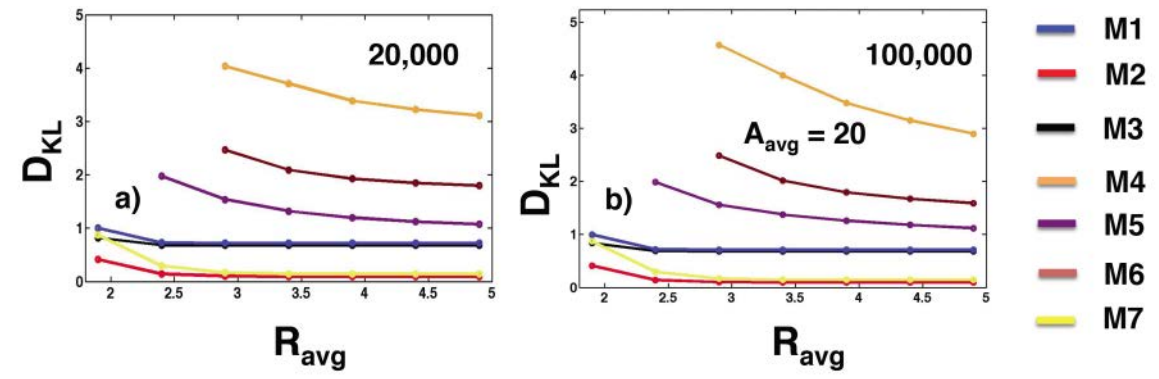


Fig S22: The sample set of 100,000 is a good sample size: We show the D_{KL} of M1-M7 for $Itk^0 = 100$ and $PIP_3^0 = 370$ for a) 20,000 realizations and b) 100,000 realizations when the amplitude average is 20 molecules and the peak time average is 2 mins. The KL distances are identical.

D_{KL} without the constraint on amplitude

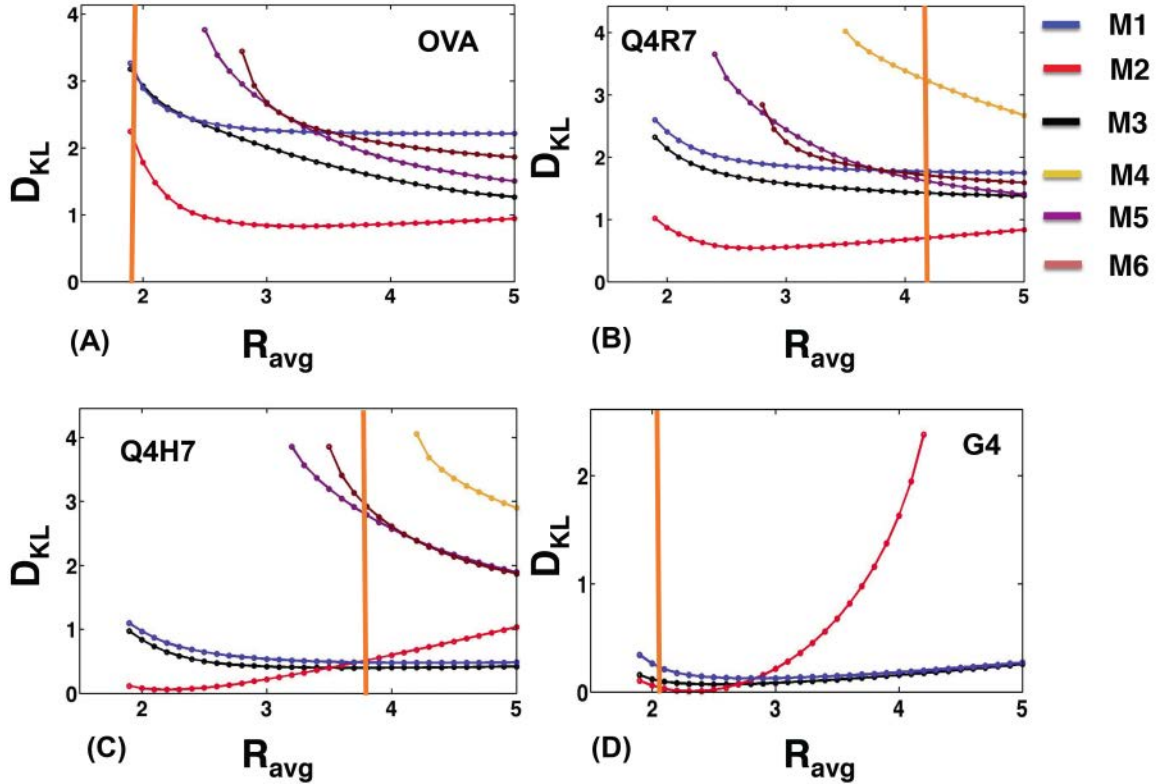


Fig S23: Model robustness, quantified by the Kullback-Leibler distance (D_{KL}) as a function of the average asymmetry ratio R_{avg} . Lower D_{KL} values (shown in \log_{10} scale) denote higher robustness for any given R_{avg} . Based on the data in Fig. 4, the average peak time was fixed at 2 mins in all cases. Experimentally measured R_{avg} values are indicated by vertical orange lines. (A) Robustness for models M1-M3 and M5-M6 at high initial I_{tk} ($I_{tk0}=140$ molecules) and PIP_3 concentrations ($PIP_{30}=530$ molecules), simulating high-affinity OVA stimulation. M2 appears most robust in the experimentally observed R_{ave} range. M4 fails produce any R value in the range investigated here. (B) M2 shows maximal robustness for moderate concentrations of initial I_{tk} ($=100$ molecules) and PIP_3 ($=370$ molecules), simulating Q4R7 stimulation. (C) For lower values of I_{tk0} ($=40$ molecules) and PIP_{30} ($=130$ molecules), simulating Q4H7 stimulation, M1-M3 are most robust with similar D_{KL} values in the experimentally observed R_{ave} range. (D) For low initial concentrations of I_{tk} ($I_{tk0}=20$ molecules) and PIP_3 ($PIP_{30}=50$ molecules), simulating stimulation by the low affinity peptide G4, M1-M3 are again most robust in the experimentally observed R_{avg} range. Models M4-M6 fail to produce any value of R in the range investigated here. Model M7 is not shown.

1. Altan-Bonnet G, Germain RN. 2005. Modeling T cell antigen discrimination based on feedback control of digital ERK responses. *PLoS biology* 3: e356
2. Kavran JM, Klein DE, Lee A, Falasca M, Isakoff SJ, Skolnik EY, Lemmon MA. 1998. Specificity and promiscuity in phosphoinositide binding by pleckstrin homology domains. *The Journal of biological chemistry* 273: 30497-508
3. Huang YH, Grasis JA, Miller AT, Xu R, Soonthornvacharin S, Andreotti AH, Tsoukas CD, Cooke MP, Sauer K. 2007. Positive regulation of Itk PH domain function by soluble IP4. *Science* 316: 886-9
4. Costello PS, Gallagher M, Cantrell DA. 2002. Sustained and dynamic inositol lipid metabolism inside and outside the immunological synapse. *Nature immunology* 3: 1082-9
5. Insall RH, Weiner OD. 2001. PIP3, PIP2, and cell movement--similar messages, different meanings? *Developmental cell* 1: 743-7
6. Stephens LR, Jackson TR, Hawkins PT. 1993. Agonist-stimulated synthesis of phosphatidylinositol(3,4,5)-trisphosphate: a new intracellular signalling system? *Biochimica et biophysica acta* 1179: 27-75
7. Guse AH, Emrich F. 1991. T-cell receptor-mediated metabolism of inositol polyphosphates in Jurkat T-lymphocytes. Identification of a D-myo-inositol 1,2,3,4,6-pentakisphosphate-2-phosphomonoesterase activity, a D-myo-inositol 1,3,4,5,6-pentakisphosphate-1/3-phosphatase activity and a D/L-myo-inositol 1,2,4,5,6-pentakisphosphate-1/3-kinase activity. *The Journal of biological chemistry* 266: 24498-502
8. Rebecchi MJ, Scarlata S. 1998. Pleckstrin homology domains: a common fold with diverse functions. *Annual review of biophysics and biomolecular structure* 27: 503-28
9. Ashok Prasad JZ, Jayajit Das, Jeroen P. Roose, Arthur Weiss and Arup Chakraborty. 2009. Origin of the sharp boundary that discriminates positive and negative selection of thymocytes. *PNAS* 106, no. 2: 528-33
10. Gillespie DT. 1977. Exact Stochastic Simulation of Coupled Chemical-Reactions. *Journal of Physical Chemistry* 81: 2340-61
11. Volfson D, Marciniak J, Blake WJ, Ostroff N, Tsimring LS, Hasty J. 2006. Origins of extrinsic variability in eukaryotic gene expression. *Nature* 439: 861-4